Self-assembly of anisotropic particles driven by ice growth : Mechanisms, applications and bioinspiration

Florian Bouville

N° D'ORDRE 2013ISAL0155
ANNÉE 2013

THÈSE

SELF-ASSEMBLY OF ANISOTROPIC PARTICLES DRIVEN BY ICE GROWTH: MECHANISMS, APPLICATIONS, AND BIOINSPIRATION

présentée devant

l'Institut National des Sciences Appliquées de Lyon

pour obtenir

Le grade de docteur

ECOLE DOCTORALE : Matériaux de Lyon
SPÉCIALITÉ : Science et Génie des Matériaux

par **Florian Bouville**

Ingénieurs de l'Institut National des Sciences Appliquées

Soutenue le 11 décembre 2013 devant la Commission d'examen

JURY MM :

D. R. CLARKE	Professeur, HARVARD, Cambridge (Etats-Unis)	(Président)
S. DEVILLE	Chargé de Recherche CNRS, LSFC, Cavaillon	(Co-Directeur)
J-M. DROUIN	Ingénieur Chercheur, Saint-Gobain CREE, Cavaillon	(Invité)
E. MAIRE	Directeur de Recherche CNRS, MATEIS, Villeurbanne	(Directeur)
C. MARTIN	Directeur de Recherche CNRS, SIMAP/GPM2, Grenoble	(Rapporteur)
W. C. K. POON	Professeur, Université d'Edinburgh (Royaume Unis)	(Invité)
F. ROSSIGNOL	Directeur de Recherche CNRS, SPCTS, Limoges	(Rapporteur)

Remerciements

A la fin de cette thèse, vient l'heure redoutée d'écrire les remerciements. Redoutée ? En effet, j'aimerais terminer cette section particulière en n'oubliant aucun des acteurs ayant participé de près ou de loin à ce périple. Il est temps de se lancer :

Premièrement, comme le veut la coutume, je tiens à exprimer ma gratitude à mes deux encadrants, Sylvain Deville et Eric Maire, pour m'avoir permis de travailler avec eux et du suivi, conseils et critiques dont j'ai pu bénéficier. Mais ma gratitude va bien au-delà de ces remerciements formels. Sylvain, tu m'as fait comprendre et apprendre ce qu'est le métier de chercheur, sous ces (très diverses) formes. Merci donc pour tes conseils, ton temps, tes talents en marketing et stratégie, tes corrections éclaires et bien sûr pour nos discussions sur des sujet tout autre que scientifiques. Eric, malgré la distance et nos contacts seulement ponctuels, tu as été disponible, ton aide et ton recul ont été précieux, tes corrections rapides, tes conseils avisés, bref, pour ton encadrement.

Je tiens à remercier Loïc Jourdaine, directeur de centre Saint-Gobain CREE, et Daniel Urffer, directeur scientifique du centre, de m'avoir accepté pour mener à bien ce projet. Je remercie aussi Caroline Tardivat, directrice de l'unité mixte de recherche, et Christian Guizard, directeur, de m'avoir accueilli au laboratoire et de m'avoir accordé leur confiance tout au long du déroulement de cette thèse. Enfin, je tiens à remercier spécialement Benoit Watremetz et Jean-Michel Drouin, pour m'avoir engagé en tant que stagiaire (il y a presque quatre ans !) dans l'équipe SIMPA et sans qui je n'aurais sûrement pas pu avoir cette offre. C'est pour moi un honneur de remercier les différents membres du jury, pour avoir accepté d'évaluer ce travail. Je remercie donc Christophe Martin et Fabrice Rossignol d'avoir accepté d'être rapporteur de cette thèse, en espérant qu'ils ont apprécié la lire autant que j'ai apprécié la faire. I would like to address a special thanks to the president of this jury, Professor David R. Clarke, who crossed an ocean to attend to my defense. My thanks also go to Professor Wilson C.K. Poon, who accepted the invitation to evaluate my work. Enfin, un second merci à Jean-Michel Drouin, pour avoir accepté de faire partie de ce jury.

J'ai été en contact avec de nombreuses personnes lors de la réalisation de cette thèse, pour garder cette section lisible je vais essayer de tout « ranger » par laboratoire et/ou site. Je démarre par remercier mes collègues (et amis) de l'unité mixte : Daniel (ou la surpuissance des statistiques dans les débats), Jordi (I'm still waiting for the croquetas. . .), Jérôme (Wolfy, le co-bureau idéal, entre autre), Emeline (malgré sa présence sporadique au cours de ces trois années), Daniel (le D.A .C. et ses conseils en géopolitique du CREE), Adam (« Voodoo and black magic » is now my definition of mechanics too, not so far from my definition of sintering though. . .), Helena (pour avoir essayé de m'initier à la chimie et à la course), Régine (sans qui le labo ne tournerais pas aussi bien), Stéphane, les « nouveaux » : Jérémy (pour ton sens de l'humour) et Juliette (tu m'as convaincu pour le confocal), les « anciens » : Gilles (Gilou), Idris (Hybride), Gisèle (« le petit chose », expression devenu célèbre), Audrey, Laure, Maira, les « intermittents de la science » (stagiaires) : Etienne (sans qui une partie de ce travail n'aurait pas été possible, calgon !), Emmanuelle, Giulia, Vanessa, Damien. . . Bien entendu, je tiens à remercier le personnel du centre, plus spécialement, Atanas, Guillaume (Guitz), Olivier, Yannick, Dorothée, Mathieu. . .

Du côté de l'INSA, parce que malgré le peu de temps que j'y ai passé, j'ai pu avancer, travailler et échanger, notamment avec Jérôme Adrien, Guillaume Bonnefont, Bertrand Van de Moortèle, Sylvain Meille, Sandrine (pour les 24h à l'ESRF !).

-famille et amis

Abstract

Self-assembly phenomena are of prime interest in materials science, because they fill the gap between assembly of macrostructure and processing of nanomaterials. Self-assembly is based on the spontaneous organization of individual small constituents into patterns and structures. Controlling the spatial arrangement can possibly improve materials properties by maximizing its response in a given direction. Furthermore, particular types of spatial arrangement, such as found in natural structures, can even induce new properties.

During the past three years, we have used ice templating process to trigger the assembly of platelet-shaped particles to replicate the hierarchical structure of nacre. Control over this technique allowed structural customization at different length-scales: local orientation of the platelets, ice crystal long range order, and the control if the interfaces between the platelets. This hierarchical process has set the ground for the creation of a new fully mineral nacre-like alumina.

The local platelet self-assembly triggered by ice growth was investigated by Discrete Element Modelling which provided new insight into the dynamic phenomenon responsible for the particles alignment. Synchrotron X-ray tomography was used to validated the model results. The different architecture observed in the final samples are not the result of a percolation threshold, as one could expect, but is instead a consequence of the delicate balance between pushing and engulfment at the solidification front.

The local alignment of platelets can be beneficial for the functional and structural characteristics of composites and relevant aspects for two potential applications were investigated: the thermal properties of the hexagonal boron nitride/silicon rubber composites and the mechanical properties of macroporous alumina.

Further adaptation of the process allowed for long range ordering of the ice crystals (up to the centimeter scale). Different tools have also been developed in order to characterize the response of composites as a function of the architecture at the level of the macropores and particle organisation.

Once those two levels of alignment were achieved, the addition of a glassy phase and nanoparticles to the grain boundaries of the platelets introduces, just like in nacre, interfaces capable of deflect and even stopping crack propagation. The final nacre-like alumina presents toughening mechanisms that raise the critical stress intensity factor (K_{IC}) from 6 MPa$\sqrt{m}$ to more than 20 MPa$\sqrt{m}$, while retaining stiffness, hardness, and strength values of a dense and fine grain alumina.

Résumé

Les phénomènes d'auto-assemblage sont au premier plan de la recherche en sciences des matériaux car ils comblent le vide laissé entre les procédés d'assemblage à l'échelle macroscopique et nanoscopique. L'auto-assemblage est basé sur l'organisation spontanée de composants individuels en motifs et structures. Contrôler l'agencement de la matière peut accroître les propriétés de matériaux en maximisant leurs réponses dans une direction préférentielle. Certaines architectures particulières, comme celles présentent dans les matériaux naturels, peuvent même faire émerger de nouvelles caractéristiques.

Au cours de ces trois années, nous avons utilisé l' « ice templating » (texturation par la glace) pour déclencher l'alignement de plaquettes de dimensions microniques afin de répliquer la microstructure de la nacre. Le contrôle de cette technique permet d'influencer l'architecture des materiaux à divers échelles : l'alignement local des plaquettes, l'alignement à longue distance des cristaux de glaces et enfin le contrôle de l'interface entre ces-mêmes plaquettes. Ce procédé a permis la création de matériaux inorganique avec une microstructure semblable à la nacre.

L'utilisation d'une modélisation par éléments discrets nous a permis d'étudier la dynamique de cet auto-assemblage. Parce qu'il tient compte de la dynamique du procédé, ce modèle nous a révélé comment l'organisation de ces particules se produit. La tomographie par rayon X a permis de visualiser les structures finales des échantillons et d'attester de la pertinence du modèle.

L'alignement local des plaquettes dans les parois générées par la congléation peuvent accroître les propriétés fonctionnelles et structurales de composite. Deux applications ont été étudiées : la conduction thermique dans des composites nitrure de bore hexagonal / silicone et la résistance mécanique d'alumines macroporeuses.

Une adaptation du procédé a permis d'obtenir l'alignement à longue distance (quelques centimètres) des cristaux de glaces. Différents outils ont été développés pour caractériser la réponse de ces composites en fonction de leurs architectures aux deux échelles considérées (celles des macropores et parois).

Après la mise en place de ces deux niveaux de contrôles sur la structure, l'addition d'une phase vitreuse et de nanoparticules aux joints de grains des plaquettes a introduit, de façon similaire à la nacre, des interfaces pouvant dévier et arrêter la propagation de fissures. L'alumine structurée présente des mécanismes de renforcements augmentant le facteur d'intensité de contrainte critique (K_{IC}) de 6 $MPa\sqrt{m}$ à plus de 20 $MPa\sqrt{m}$ tout en conservant la rigidité, la dureté et la résistance d'une alumine dense à grains fins.

Contents

Publications resulting from this work

Section 2.2 of the chapter 2 has been accepted as an article in the Journal of American Ceramic Society:

> Bouville Florian, Deville Sylvain, ”Dispersion of Boron Nitride Powders in Aqueous Suspensions with Cellulose", *Journal of the American Ceramic Society*, (2013)

Section 3.3 of the chapter 3 has been submitted as an article:

> Bouville Florian, Eric Maire, Deville Sylvain, ”Self-Assembly of Facetted Particles Driven by Ice Growth", (submitted 2013)

Section 4.3 of the chapter 4 has been submitted as an article:

> Bouville Florian,Maire Eric, Deville Sylvain, ”Lightweight and stiff cellular ceramic structures by ice templating", (submitted 2013)

Section 5.2 of the chapter 5 has been submitted as an article:

> Bouville Florian, Portuguez Etienne, Chang Yunfei, Messing Gary L., Stevenson Adam J., Maire Eric, Deville Sylvain, ”Templated grain growth in macroporous materials", (submitted 2013)

Section 6.2 of the chapter 6 has been submitted as an article:

> Bouville Florian, Maire Eric, Van de Moortele Bertrand, Stevenson Adam J., Deville Sylvain, ”Strong and tough bioinspired ceramics from brittle constituents", (submitted 2013)

Three patents have been filed on this study.

Introduction

The terms self-assembly and bioinspiration are extensively used in materials research. The first represents a promising category of processes and the second, through natural materials, is among the most successful example of composites so far. Bulk processing of materials presents limitations, because the materials are used in their bulk form and thus limited to their intrinsic properties. The example of ceramics is striking: they are the stiffest, strongest and most thermally stable materials, but also the most brittle ones. This limits their uses to a safe zone where they present the lowest chance of failure. For safety-critical applications, only low-strength high-toughness materials are chosen, which limits upon the development of new technologies that are more demanding. Similar examples can be found in other fields than structural materials, where materials face completely antagonist requirements, such as high ionic conduction combined with a high thermal stability. Only so much can be achieved by changing the composition or microstructure, and most of the recent engineering materials are composites. Indeed, to fulfill antagonist requirements, the logical choice is to mix materials, each one providing a functional or structural property. Beyond materials intrinsic properties, their spatial arrangement and interfaces are also critical. The spatial arrangement can be controlled at the macroscale (like fiber composites or cermets) or at the nanoscale (in microelectronics) but achieving control in the range of a few to a tens of microns is still difficult. Moreover, organizing materials at different scales (by introducing hierarchy) can also induce remarkable improvements.

This gap in length scale is filled by the self-assembly processes, where small building blocks (from the micrometer to the nanometer scale) are organized by different processes to palliate the incapacity of producing them piece-by-piece. Many processes are available, depending on the dimensional requirement and can be combined to obtain more complex (or achitectured, hybrids etc...) materials. As more and more appraoches are available to produce such materials, the question of how to organize them in the most efficient way is quickly becoming critical. Inspiration can be draw from the structure of natural materials because there are composite

materials whose architecture is defined at multiple scales. The raw materials are limited and thus the structure has to be as efficient as possible to obtain viable materials for the living organisms (like the well-known examples of nacre, wood or bone). Natural materials are also made by self-assembly, they provide thus an additional source of inspiration for the processes. Self-assembly and natural materials are thus intimately linked.

The two main topics mentioned above represent the global context of this study. This work is in the direct continuity of the research initiated by Sylvain Deville on ice templating, bioinspired materials and processes [1]. Ice templating is a way to create porous materials that uses the growth of ice crystals in suspension to template the final porosity. It now constitutes a well-established, versatile technique for which any kind material can be used. Because the growth of the crystals is usually directional, materials with a structural anisotropy are obtained. The porosity templated by the ice crystals with ice is lamellar and the resulting organization of walls are similar to the brick and mortar structure of nacre. So far, the building blocks used to mimic nacre are formed by the ice segregation, their size is thus limited to a few microns (compared to a few hundreds of nanometers for the platelets in nacre). The size of the buildings blocks matters because it defines the number of interfaces in the composites, which plays a particularly important role in the final properties. The original idea of this research is to reduce the size of the building blocks to one comparable to nacre's platelets. The solution chosen here is the use of platelet shaped particles and their alignment triggered by the growth of ice crystals. Ice-templating can thus be used as a self-assembly process.

The structure of nacre has long been an appealing model for materials scientist because it can generate fracture toughness (resistance to crack propagation) mostly by extrinsic mechanisms that shield any crack from the applied loads. Because this toughening mechanisms are developed over many length scales (nano to macro), they are extremely difficult to replicate in synthetic structures. The final goal (also known as the "Holy-Grail" for me) of this study was to develop a material that replicates most of the structural features of nacre. In other words, a dense material constituted of a brick and mortar structure at the 500 nm scale with carefully controled interfaces. In addition we have to try to palliate some drawbacks of the natural structures and most of the synthetic composites by removing any organic component. This was no easy endeavor, because several processing steps had to be studied, invented or improved to obtain such a material.

This manuscript is organized by increasing complexity towards the final architecture.

The first chapter has the (tedious) task to present the concepts of self-assembly at different length scales, the processing strategies developed so far, but also the relationships between natural materials and self-assembly. The research that combine ice templating, bio inspiration and self-assembly are also presented in this part.

The chapters two to six have been published in different journals (cf. publications list page viii); the experimental methods are detailed within each parts. The second chapter describes the specific suspensions that were developed in order to produce the materials reported in the next chapters.

The third chapter tries to answer the question of how ice templating can align anisotropic particles. Because it is based upon dynamical aspects (an increasing particles concentration in the confined space of growing crystals), a discrete element model was built to visualize what happens during the solidification of this peculiar system.

The fourth and fifth chapters report the successive steps that were necessary to obtain the final nacre-like material. The fourth chapter is the use of the platelets alignment in porous or composite materials, where the benefits of ice templating to control particle orientation are illustrated with two properties, thermal and mechanical. With the arrival at the laboratory of Adam J. Stevenson and a partnership with the Pennsylvania State University, this work have earned a piezoelectric component, which conduces to the fifth chapter of the manuscript. It pushes further the complexity by trying to control the orientation of the ice crystals over long distance. This chapter introduces also a more complex set of initial particles, comprising platelets and spheres.

Finally, the sixth chapter is the accomplishment of the study, where all the previous steps are combined and the control of the interface is added, to obtain a material composed entirely of ceramic but, because it replicates many of the structural features of nacre, is characterized by a unique combination of high strength and high toughness.

Chapter 1

Self-assembly... Self-assembly everywhere

1.1 Introduction

The vocation of this first chapter is to describe the background of the studies reported after. Different fields, materials and objectives are involved, and a specific and relevant bibliographic part is made for each. But they also all collapse within the same category, the design of materials by self-assembly, or the relative control of the organization of materials at different length scales. Self-assembly processes are of prime interest in materials science, because of their ability to organize constituents at a scale that cannot be achieved otherwise. The interest goes well beyond materials science, from the chemistry, where the first examples where found, to the behavior of atmospheric clouds.

A preliminary definition is required, in particular regarding the term 'self-assembly'. There is apparently no consensus on a definition and this expression is used in an increasing number of publications in various fields (see figure 1.1a and b). This definition seems so broad that everything (or nothing) could be considered as a self-assembly process [2].

One possible definition is a process that involves elementary constituents (distinctive parts of a disordered structure) and conduces to a reversible disorder-to-order transition (which does not involve permanent bonds). This definition can be related to the field of chemistry, where this self-assembly term seems to originate. But even in this definition, several types of self-assembly processes can be distinguished.

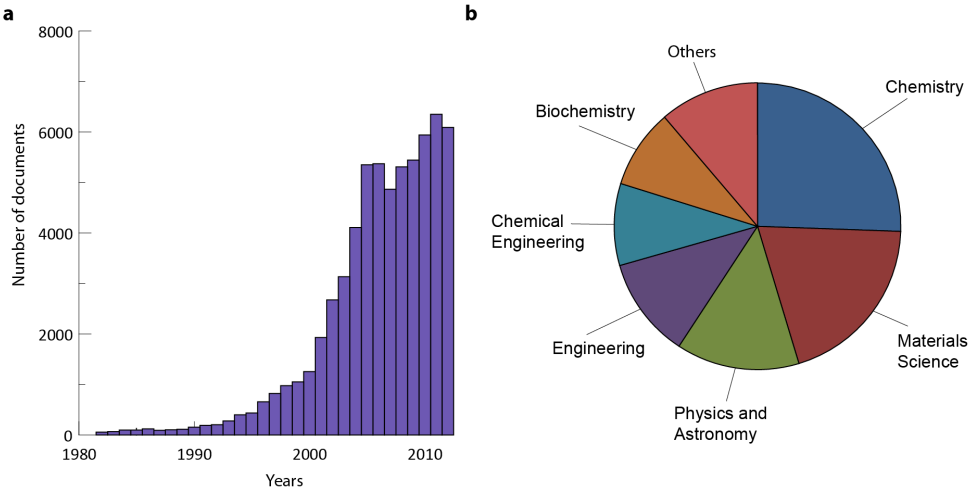

Figure 1.1: **Some statistics about the use of "self-assembly" in scientific literature.** a) Number of publications using "self-assembly" in the title or the abstract each year. b) Repartition per scientific fields of the publications mentioning "self-assembly". Source Scopus.

The first type is static, when systems are at a local or global energy minimum and do not dissipate energy, even if some energy can be required (such as stirring) to promote the arrangement. For instance, molecular crystal are formed by static self-assembly [3]. This is the most extensively studied type. The second one is dynamic where the system organization involves energy dissipation, the most well-known example being the reaction diffusion process [4]. Because of its extreme complexity, the dynamical self-assembly is less understood but is the object of increasing research efforts [5]. In static self-assembly, two variants are present, one called *templated self-assembly* where interactions between the components and features from the environment define the final structures, another called biological self-assembly characterized by the complexity and variety of the resulting structures. The main idea is that the intrinsic properties of the building blocks (shape, charges, surface properties, magnetic dipole, etc ...) act like a code and define the final structures. The fine control over this properties is required to obtain well-defined final structures. Because no type of interaction or dimension is specified, this concept can be applied for molecules as well as weather systems [6], and thus explain the variety of fields where those words appear (cf. figure 1.1b).

Now that the term has been defined, the rest of this chapter is organized as follows. The first part details the different types of self-assembly that are (relatively) close to ice templating in terms of dimensions of the building blocks. The different sections are organized by growing size, from molecules to particles. The driving force or the main factors that defines the assembly are described through examples along with their advantages and limitations. A short detour is taken after this part to look at self-assembly in natural systems. The interest here is twofold: they are the most complex self-assembly processes known so far and the architectures that result from these mechanisms are an extensive source of inspiration to design more efficient materials and processes. Finally, a review of what has been done so far in self-assembly and bioinspiration by ice templating is presented.

1.2 Self-assembly of molecules

This section contains a brief description of the self-assembly that occurs when short molecules are used, with the well-known example of micelles but also the more complex and controlled block copolymer assembly. Comprehensive reviews are available [7, 8] and can be used in this section as references. As for nearly all the other topics, the entire manuscript would not be sufficient to accurately describe this field. The objectives here is only to introduce the main concepts and requirements of this technique through simple examples.

1.2.1 Micellar organization and block copolymers

The principle of molecular self-assembly is relatively simple and the first classical example is the assembly of surfactants in a solvent. This is the process by which soap molecules clean. A surfactant presents two components, a solvophile head and a solvophobe tail (longer chains than the head, see figure 1.2a). When those molecules are put in a solvent, they homogeneously mix with it until a limit concentration is reached, the critical micellar concentration (CMC). Above this concentration, it is energetically more favorable for the molecule to separate from the solvent. They form spherical assembly with all the tails at the center in contact with each other and the solvophile heads facing the solvent [9]. The most common system is soap in water, such as sodium stearate, where the head is polar and thus hydrophile and the tail is apolar chain, thus hydrophobe. This phenomenon belongs to the static self-assembly category. Different chemistries can be used and adapted to the solvent. Different morphologies can be obtained as the concentration increases [9].

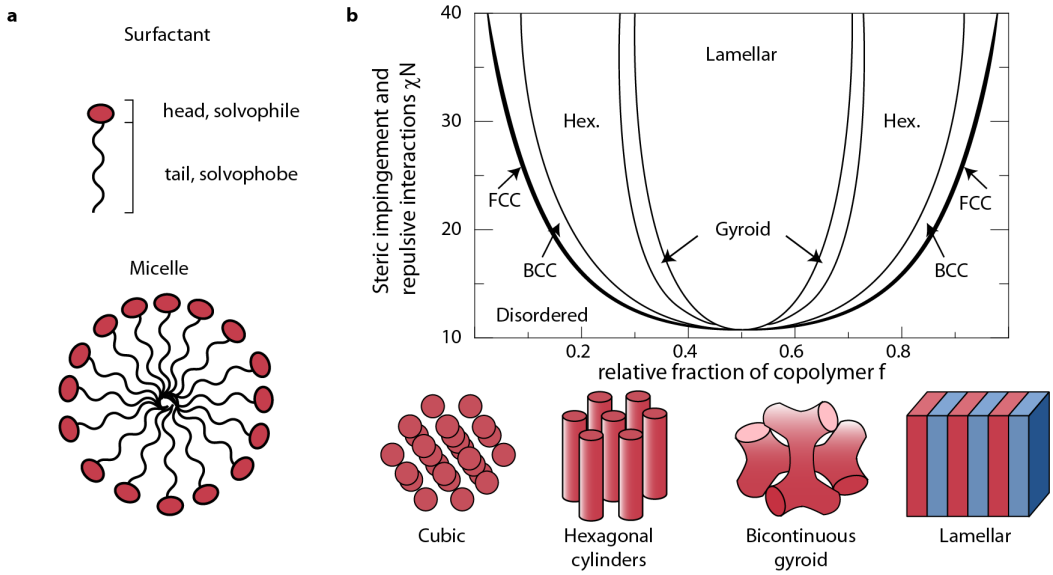

Figure 1.2: **Self-assembly of molecules and macromolecules.** a) Anatomy of a surfactant and schematic representation of the micelle that forms in the dedicated solvent. b) Phase diagram and schemes of the different phases that can be obtained with block copolymers. The x axis is the relative fraction of copolymer component and the y axis represents the affinity and steric parameters. χ is the relative affinity of the components (Flory interaction parameter) and N the number of repetitive units.

The block copolymers are an extension of this concept: macromolecules are constituted of blocks (two or more) with a different chemistry. The nature, the length and the number of blocks can be changed, which in turn affects the arrangement of those polymers in solution. In figure 1.2b a phase diagram of typical block copolymer is depicted[8], like in the system poly(isoprene-b-styrene) or poly(ethylene oxide-propylene oxide) (PPO-PEO-PPO, commercially sold under the trademark Pluronic). The main parameters that guide the structure are a combination of steric impingement (the degree of polymerization of the blocks) and interaction parameters (χ, related to the Flory-Huggins interaction parameters) versus the relative size of the blocks. Different architectures can be obtained, from a cubic arrangement at low fraction of one block to lamellae at equal fractions of blocks. It is worth mentioning that the Flory-Huggins χ parameter is inversely proportional to the temperature so that this phase diagram is also temperature dependent [10]. But like all the phase diagrams, the phase behavior is given but not the resulting microstructure, which depends also of the technique used to shape such polymers and is briefly described in the next section.

Finally, recent developments are based on different types of molecules, and the resulting materials are referred to as supramolecular. The basic principles are the same but instead of using covalently bond chains, small molecules assemble under the action of weaker forces (hydrogen or electrostatic bonding). Those materials present characteristics similar to the macromolecules but because of the bonds involved, they can assemble and disassemble dynamically, which gives rise to peculiar and interesting properties such as self-healing. More details can be found elsewhere [11, 12, 13].

1.2.2 Overview of preparation methods

The different phases that can be obtained by molecular self-assembly are dictated by their interactions and constitutions. But the resulting architecture also depends on the shaping processes. The assembly of those molecules occurs when the concentration is increased (as in micellar systems) and the domain of organization follows a nucleation and growth mechanism. The concentration is usually increased by the evaporation of a solvent (for instance by evaporation on a substrate, by spin-coating or by Langmuir-Blodgett process) and a thin film is obtained. Because of the nucleation and growth process, different organized domains are formed with a typical dimension of 0.5 μm^2. The substrate and the external conditions play a critical role on the formation of the domains. So the application of stresses or the use of a patterned surface [14] (see figure 1.3) can increase the size of the domains to the mil-

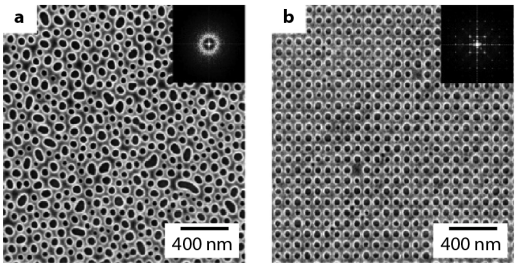

Figure 1.3: Vertically oriented cylinders of PS-b-PMMA diblock copolymer on a) a neutral surface and b) on a surface that contains an array of dots in a square pattern. Reproduced from [14].

limeter scale (or even form a centimeter-size single crystals [8]). Some techniques can be used to obtained real three dimensional systems, such as colloidal crystal templating (discussed in the next section 1.3.3) or foam replication.

1.2.3 Applications

Unsurprisingly, the largest use of micelles is in the detergent market [7]. But the main use of block copopolymers is to serve as a template in hybrid materials [7, 15]. Because of their ability to self-organize in various mesostructures, they can be infiltrated afterwards by inorganic precursors (which can alternatively be incorporated before self assembly) and degraded upon thermal treatment to leave only their skeleton. An ordered (or not) mesoporous material can be obtained (with pore sizes from 1 nm to 10 nm). The main application is thus for templating monolith for catalytic applications [15], because the presence of pores allows to increase dramatically the specific surface of the material while having a larger pore size than in zeolithes based materials. Those materials can be useful wherever diffusion of species is needed, and for instance have been successfully used in lithium batteries as an anode material [16]. However, in every application and because it is inherently a two dimensional process, another step is required to obtain fully functional materials. Colloidal crystals templating, described in the next section, can be one of this additional process.

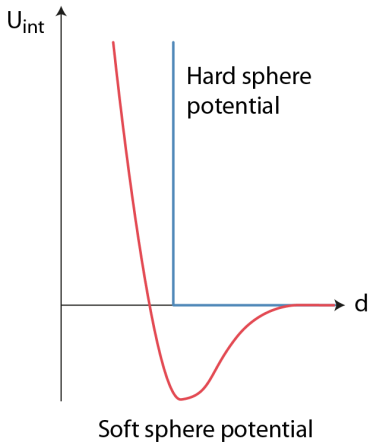

Figure 1.4: Interaction potentials that exist between two colloidal particles separated by a distance d.

1.3 Self-assembly of particles

The colloids self-assembly has been a growing field of research over the past decades, because of the parallel that can be drawn between colloidal particles and atoms. This similarity was first studied by Albert Einstein himself when he discovered that colloidal particles in liquid present the same density distribution as a gas (the barometric distribution). Even if particles are relatively large (although typical sizes are below 1 μm), their behavior is dictated by solvent interactions and diffusion, thus not (exclusively) by the gravity. This similarity makes them an intriguing model system to study phenomena that are nearly impossible to monitor at the atomic scale so far, such as gas-liquid interfaces, the glassy states and what is of particular interest for us here, crystallization [17]. Indeed, such particles may undergo disorder-to-order transition under certain circumstances to a particle assembly that present long range order, called colloidal crystals. The main mechanisms of colloidal crystal formation is described along with their processing route and the practical and fundamental applications.

1.3.1 Colloidal crystals

The first rule to know about colloids is that they can interact through two main different kinds of potential. The first one, which is also the simplest is the hard

sphere potential (see figure 1.4), where there is just an excluded volume representing the impossibility for particles to interpenetrate. This case represents the ideal case, because no attraction occurs between two particles and thus they can move independently from each other without sticking (flocculating) when they get closer. Experimentally this type of potential is extremely difficult to obtain [18] because the refractive index of a non-polar medium is different from the particle. Attractive Van-Der-Walls forces (here London dispersion forces) appear [19]. The index of the medium can be matched to a certain extent (for organic particles especially) but not for all the materials.

The usual pair potential between two particles is thus closer to the model of soft spheres (see figure 1.4) where the potential is the sum of attractive and repulsive terms. Again, in order to obtain colloidal crystal, particles must be free to move with respect to each other. If the dwell created by the attractive part is too deep (so that too much energy is gained when two particles stay close with respect to their thermal energy), the particles flocculate easily and no long range order can be obtained. This energy minimum needs to be avoided, or at least minimized, in order to get closer to the ideal hard sphere situation. This is usually achieved by the adsorption of polymer onto the surface that creates a supplementary steric repulsive force [20, 19]. The other condition to create colloidal crystals is a carefull control of particle polydispersity. Particles must present the same size to avoid stacking faults in the structures. An increasing number of techniques are available (such as emulsion polymerization, sol-gel etc ...) to create organic (mostly PMMA and PS spheres) or inorganic (mostly silica) particles of different sizes (0.02 μm to several μm) with a very narrow diameter distribution [21].

As long as these requirements are met, colloidal crystals can form in solution. Growth methods detailed in the next section (1.3.2) are built upon the same principles: the controlled increase in particles concentration (usually by settling). Because the density of the particles is different than that of the medium, particles eventually settle. The concentration at the bottom of the recipient increases over time (from hours to months depending on the system) and the particles, because they can move freely, undergo a disorder-to-order transition. This transition involves no change in heat or energy (a Kirkwood-Alden transition) and is driven only by entropic effect [21]. The general packing structure obtained is a face-centered-cubic lattice (or opal structure) with a compacity around 74% (see figure 1.5a and b). Because the two conditions can be obtained not only for spheres, but also for regularly shaped particles, different structures can be formed. Example of assembly of faceted particles are presented in figure 1.5c, 1.5d, 1.5e.

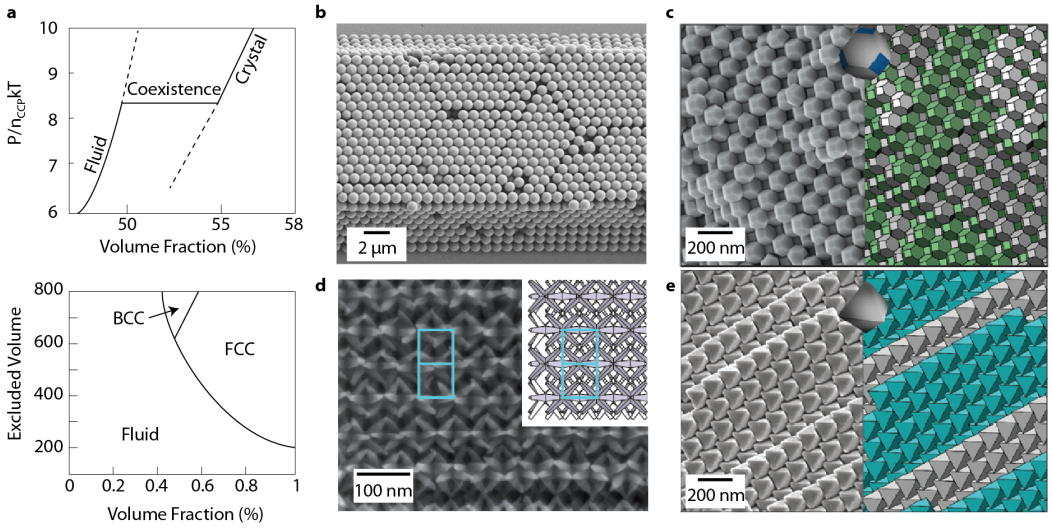

Figure 1.5: **Phase diagrams and different colloidal crystals.** a) Phase diagram of colloidal crystals as a function of the volume fraction of particles for hard (top) and charged (bottom) spheres. After [21]. b) Colloidal crystal obtained with PMMA sphere of 1 µm. c) and e) colloidal crystals with truncated cube and poylyhedral particles. From [22]. d) Colloidal crystal made from octapod particles. From [23].

When the assumption of hard sphere potential is not relevant, as with a polar solvent and/or other particles types are used [a], colloidal crystals can also be formed. However, long range interactions, such as coulombic interaction, must be present. The system is now governed by the screening length (the Debye-Huckel length). When this length is shorter than sphere radius, colloids behave like hard spheres, and when it is larger, colloids act as soft spheres with an additional excluded volume coming from the electrostatic surface charges [24, 25]. Those systems can crystallize into either FCC or BCC lattice (see figure 1.5a) [26]. Those colloids produce large 3D crystals (centimeters sizes) but have strict requirements in terms of polydispersity, surface charge density, and operative conditions. The accessible crystals lattice are also broader (FCC, BCC, and random hexagonal packing rhcp), and the use of oppositely charged particles can even form structures similar to that of ionic crystals [27]. Recent developments even demonstrated the possibility of using directional bonding over DNA patching of the surface [28], providing colloids with a directional bonding, similar (to some extent) to that of atoms. By doing so, more complex crystal structures could be achieved, such as diamond-like structures.

1.3.2 Growth methods

The formation of colloidal crystals can be achieved by numerous methods, partly similar to the ones used for molecular self-assembly (1.2.2), such as evaporation or Langmuir-Blodgett techniques. The most common, however, is the settling method that produces crystal size of around 1 μm^2. The settling rate is a critical parameter [25] and if it is too fast, particles cannot rearrange and a glassy phase is formed. On the other hand this rate also conditions the time scale over which crystals are formed. The process can be extremely slow, some systems can take up to several weeks to grow. Because settling velocity is conditioned by particles mass, relatively large particles (around 0.5 μm) are preferred. Physical confinement and hydrodynamic flow have been successfully used to obtain large scale crystals [21, 29]. Another way to obtain colloidal crystals is to use templated substrates, either with microchannels [30, 22], or array of nucleation sites [31, 14, 29, 32, 33]. These last techniques can be seen as the mesoscopic equivalent of the epitaxial growth of crystals on surface.

[a] Most of ceramic suspensions are constituted by highly charged particles.

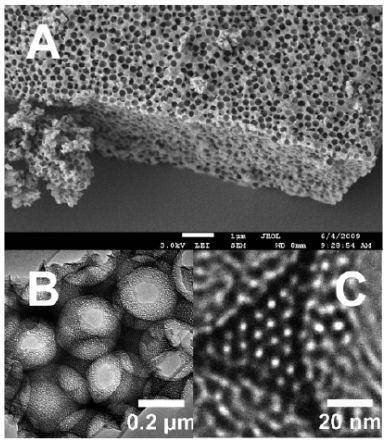

Figure 1.6: Example of a pellet presenting ordered hierarchical porosity. a) SEM images of the pellets showing the organize macroporosity from the colloidal crystal template. b) TEM image of the material showing porosity of the material between the macropores. c) TEM images of the organized mesoporosity. From [36].

1.3.3 Technical and fundamental applications

There are two main applications of colloidal crystals: photonic crystals and porosity templation. Colloidal particle sizes are in the range of visible light wavelength and thus can interact with light. A natural example is the opal structure, where silica nanoparticles are closely stacked together and thus give rise to the macroscopic iridescent aspect [2]. Because large scale 3D colloidal crystals can be obtained with finely defined lattices and particles sizes, they produce Bragg diffractions and the stop positions in the spectral band depend on the size of the particles and interparticles spaces (for more information see [21] and references therein and [34, 29, 35]). The other application is their use has sacrificial template to make hierarchical porosity [7]. As seen in a previous section (1.2.3), the main use of molecular templates resides in catalytic applications. But in order to make efficient support, those mesoporous materials have to be shaped in volume, but then only the pores on the surface are accessible. Large pores (from nanometer to several micrometers scale) are needed to help the bulk molecules (such as hydrocarbons) diffuse to the active sites in the mesopores, leading to a hierarchical porosity (see figure 1.6). Extensive studies of the improvements related to the hierarchical porosity in catalytic application have been reported [15].

On the fundamental aspect ("colloid as big atoms" [17]), because colloids share some similarities with atoms, they have been used to study numerous phenomena ([17] and references therein). The first one was gas-like diffusion initiated by Albert Einstein. The dislocation movement in colloidal crystals has also proven to be similar as in atomic crystals [33]. The presence of tunable particle's attraction make them also useful to study liquid/solid phase transition [27] and grain boundaries phases [37].

1.4 Self-assembly by an external field

The two most studied fields of self-assembly have been presented, but others processes, that rely on different properties of the building blocks, can be used. One of them is the assembly with the help of external fields (magnetic, electric or both). Examples and results about the use of electric fields are presented in section 4.2.3, here is only presented the self-assembly driven by a magnetic field. Every material is influenced to a certain extent by a magnetic field, but only paramagnetic (and superparamagnetic) materials can be easily controlled by a relatively low intensity field. Diamagnetic materials need a magnetic field of high intensity (several Tesla) to be moved and thus only small sample sizes can be obtained (for more information, refer to section 4.2.3 and references [38, 39]). If only paramagnetic or superparamagnetic materials can be used, two different strategies are available, either when the material itself is superparamagnetic (which greatly limits the range of possible materials), or when superparamagnetic particles are employed to aligned a different material. The two processes are presented below through specifics examples. Similar studies are available [40, 41] for magnetic particles self-assembly, [42] magnetic self-assembly using nanoparticles, and [43, 44, 45] for electrically driven self-assembly).

1.4.1 Direct self-assembly of magnetic particles

The facile alignment with magnetic fields of nanoparticles is based on their superparamagnetic properties. If the particles present only regular paramagnetic susceptibility, their orientation and movement are mainly dictated by the random thermal motion in solution and only magnetic fields of high magnitude could influence their movements. The superparamagnetic property of nanoparticles is a direct consequence of their small size. When small enough (between 5 and 50 nm), nanoparticles are composed of only a single domain with nearly all the atom magnetic moments aligned [48]. This peculiar property gives rise to the domain of ferrofluidic,

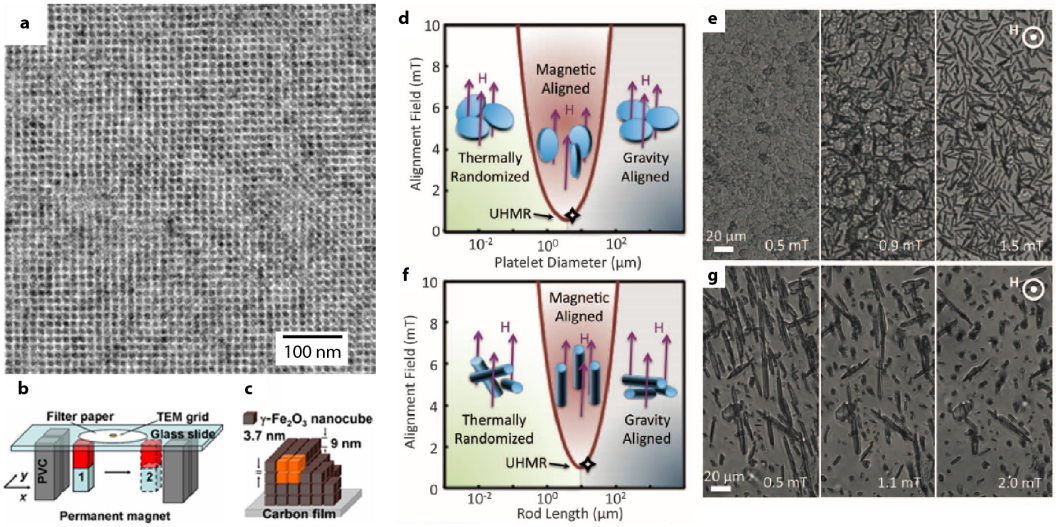

Figure 1.7: **Self-assembly of particles in a magnetic field.** a) Superparamagnetic nanocubes (maghemite $\gamma - Fe_2O_3$, 9 nm size) self-assembled into an oriented superlattice. b) Schematic representation of the magnetic-field-induced self-assembly procedure. The magnet used here creates a field of maximum 0.4 T. c) Representation of the superlattice created. Reproduced after [46]. d) and f) plots representing the behavior of surface-magnetized platelets (α-alumina) and rods (gypsum) respectively as a function of the their dimensions and the magnetic field applied. The stars denote the position of the used material on the curve. e) and g) visualization of the gradual alignment introduced by a magnet in the two systems. Reproduced after [47].

where the properties of dispersed suspensions of such particles can be controlled by the presence of a magnetic field. In the study of Ahniyaz et al. [46], well-defined nanocubes of superparamagnetic iron oxide (mainly maghemite $\gamma - Fe_2O_3$) have been synthesized and organized simply by the application of a permanent magnet upon drying. The resulting superlattices are presented in figure 1.7 along with the setup used in 1.7b. Because of their magnetic anisotropy, the alignment improvement and the particles concentration increase occurs at the same time. This process is therefore a way to create a cubic superlattice with a high degree of crystallographic orientation order with a low magnitude magnetic field. This process is nevertheless limited to superparamagnetic particles and thus cannot be used to control the orientation of other types of materials.

1.4.2 Self-assembly guided by magnetic nanoparticles

Another process based on the use of magnetic nanoparticles but with a broader range of applications has been developed by Erb et al. [47]. The approach is based on the adsorption by heterocoagulation of superparamagnetic nanoparticles onto the oxide surface. The magnitude of the magnetic field necessary to align the particles is minimal when the size of the particles is sufficient to avoid being randomly oriented by the thermal motion and at the same time small enough to avoid being aligned by the gravitational field. The intensity of the required field can be as low as 0.8 mT (see figure 1.7d and f). The main asset of this process is that any material regardless of its magnetic properties can be oriented as long as its dimensions and aspect ratio are suitable. In this study [47] the platelets have been used to reinforce a polyurethane matrix in different ways (see figure 1.8), so that the stiffness and the maximum strain of the material can be modulated by controlling the platelets orientation.

The use of a polymeric matrix allows the authors to create multi-layered composites and thus combine the in-plane and out-of-plane reinforcements. Even though those composites are interesting and easy to process, the volume fraction of platelets is limited by the sterical hindrance they generate. This packing fraction is limited to 20 vol.% in the case of static field and can go up to 50 vol.% when a rotating field (to align particles in two directions) is applied.

The use of external fields to assemble particles is a powerful tool because of the degree of control of the orientation that is reached, even with magnetic field of low intensity. Yet, restriction in terms of materials can be a major drawback, as well as limitations of reinforcement content.

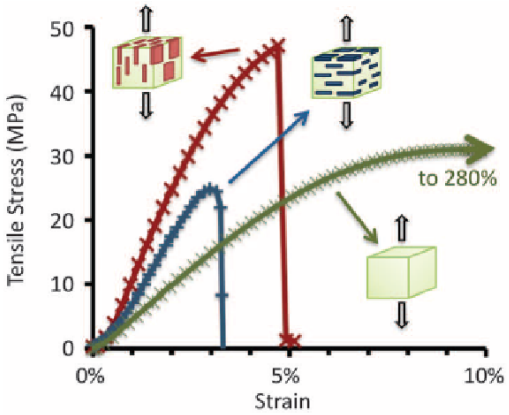

Figure 1.8: Stress-strain curves in tension of composites with and without platelets reinforcement. Reproduced from [47].

1.5 Self-assembly by layer by layer deposition

Layer by layer deposition can be used to form composite materials, where inorganic particles are aligned in a polymer matrix. Particles are first aligned on a substrate by diverse mechanisms and form an organized layer where a polymer is deposited (by spin or dip coating). Those steps are repeated several times to form a thin film (see figure 1.9d). The first study was made by Tang et al. [50], where anionic montmorillonite clay were aligned on a substrate by dip-coating in a dilute solution (0.5 vol.%) followed by a similar step in solution of dilute polymer (PDDA). The resulting film has a thickness around 1 µm depending on the number of successive depositions (see figure 1.9c). The mechanical properties in tension are presented in 1.9f. Increasing the number of layers improves both the strength and elongation of those composites, as well as the presence of cations Ca^{2+}due to a stronger interactions between the clays and the polymer. More recent researches [51, 52] on this system reported even better results with a single step process and higher mechanical properties (stiffness of 25 GPa and strength of 320 MPa), but at the expense of the material toughness.

In the second and more recent research made by Bonderer et al. [49], modified alumina platelets were incorporated in a chitosan matrix. The particles surface were made more hydrophobic by grafting (see figure 1.9a) so that when put in water they form a Langmuir-Blodgett film at the air/water interface. The aligned platelets were simply transfered by dipping on a substrate and a layer of chitosan was spin coated

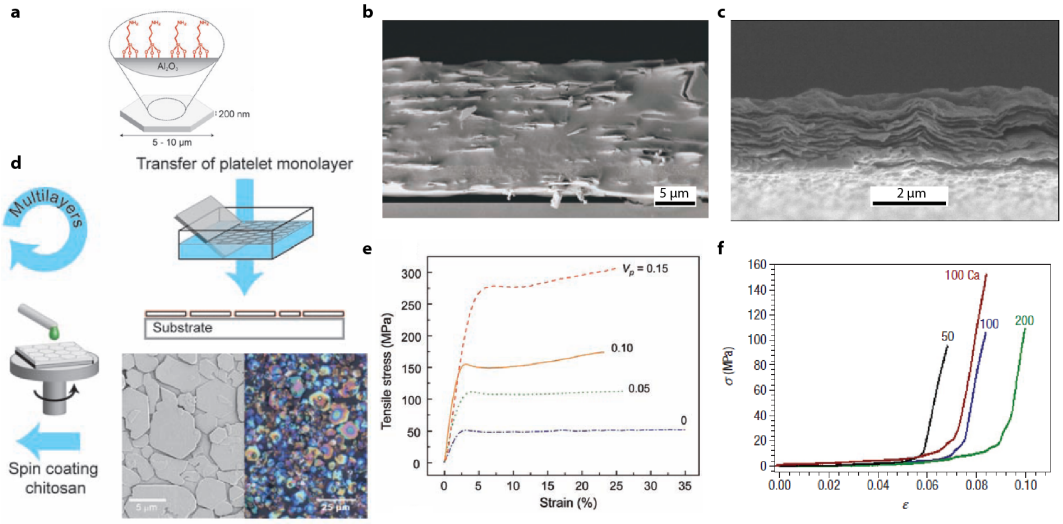

Figure 1.9: **Composite microstructure and properties obtained by layer by layer deposition.** a) Surface modified alumina platelets [49]. b) SEM image of the microstructure of the thin film composite [49]. c) SEM image of the microstructure composite clay/PDDA [50]. d) Schematic representation of the layer by layer deposition used in reference [49]. e) and f): mechanical properties of the thin films, from [49, 50] respectively.

after drying (see figure 1.9d). The addition of these reinforcement increases the yield stress with an increasing platelets content (300 MPa for 15 vol.% compared to 50 MPa with a pure matrix), without too much deterioration of the maximum strain (17 % against 35 %).

Because of the tuned interface and orientation of those reinforcements, the resulting composites present an improved strength without noticeably impinging on the deformation capability, and by doing so, they are getting closer to the characteristics of some natural materials (see 1.7.1). But as for the magnetic field assisted self-assembly, the layer by layer process is limited in terms of mineral content, which prevented them to build high strength and high toughness materials. The thickness of the final materials is also limited because of the time necessary to obtain a single layer.

1.6 Self-assembly by mechanical stresses

The previous section marked the departure from the typical self-assembly systems presented above to evolve toward less ideal systems (and thus less demanding) where irregularly shaped and sized particles are aligned. Even if the term self-assembly is less used with those systems, preferring assembly or orientation control, they still fall in the definition of the introduction (see 1.1). No intrinsic properties of the composition are used directly to trigger the alignment, only their anisotropic shapes. This simple characteristic broaden the range of eligible raw materials, because many of them can be synthesized in the form of anisotropic particles. Polydispersity is also less of a problem, and the volume fraction is higher, at the expense of a less accurate control of the orientation. The processes rely on the application of mechanical stresses. Tape casting and uniaxial pressing are good examples of this approach.

1.6.1 Tape casting

Tape casting, where a suspension is uniformly spread on a support by the action of a doctor blade, is a conventional industrial ceramic process. It is inexpensive, scalable and able to produce uniform material with an interesting throughput. Most of the capacitors are made by tape casting, as well as layered ceramics such as solid oxide fuel cells. The control of particles orientation is possible due to the shear stress that exists when the doctor blade slides across on the surface. This alignment process has been studied in various articles ([54, 55] and references therein). One of the main factor responsible for the phenomenon is the particles volume fraction. The

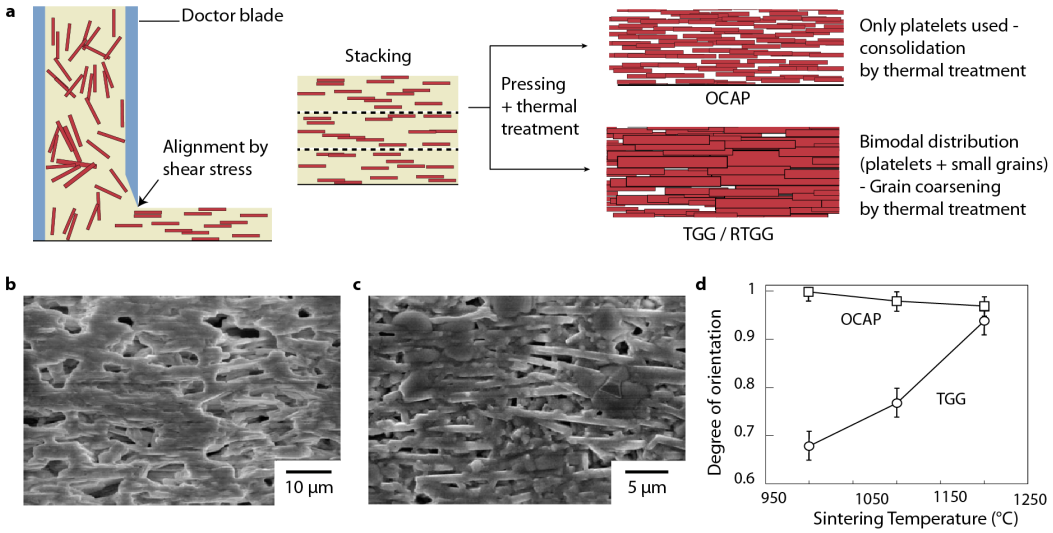

Figure 1.10: **Schematic representation of tape casting and the two main strategies to obtain dense and textured ceramic.** b) and c) SEM pictures of tape casted $SrBi_4Ti_4O_{15}$ by the OCAP and TGG methods respectively, both sintered at 1200 °C during 2 hours. After [53]. d) Degree of orientation (represented by the Lotgering factor) of tape casted ceramics at different sintering temperatures.

alignment is due to the collective rotation of particles created within the top sheared surface that propagates from particles to particles. Platelet shaped particles are preferred because the alignment is obtained in a plane [b]. Their sizes have to be large enough to avoid the randomization by thermal agitation. As long as enough particles are present in the medium (determined as 30 vol.% by [54]), their rotation in the top layer is sufficient to align the rest (with a loss throughout the thickness). This setup can efficiently produce ceramic parts where all the grains are aligned along the crystallographic axis of the platelet basal plane but not oriented in the plane.

However, because the aim here is to create dense and textured ceramic parts, the densification must also be controlled. Up until now, two main strategies have been developed, usually referred to as the Oriented Consolidation of Aligned Platelets (OCAP) method and the (Reactive) Templated Grain Growth (TGG/RTGG) method [53] (see figure 1.10a). OCAP consists in the use of platelets only, aligned by tape casting and stacked, and finally sintered. This method is the simplest, at the expense of a generally lower final density. Large particles have to be used, their mass prevents much of the particles rearrangement during thermal treatment and consequently less porosity is removed, unless pressure assisted techniques are used. To avoid this issue, the TGG method has been developed [56, 57]. A bimodal distribution is necessary, large and aligned platelets act as seeds for the orientation, and small isotropic particles help the densification (see 5 for more details). The study made by Kimura et al. [53] illustrated the difference between the two techniques. The degree of orientation obtained by the two methods is different (see figure 1.10d). With the OCAP method platelets are already well-aligned without any thermal treatment. For TGG, the alignment is improved by the sintering step, because the templates grow at the expense of the non-oriented small particles.

This method is probably the most promising technique to obtain textured and dense ceramics at the industrial scale, which is a real challenge for piezoceramics.

1.6.2 Uniaxial pressing

Uniaxial pressing can also be used to align anisotropic particles. Pressure applied on randomly oriented platelets tends to align them simply because their basal plane is not perpendicular to the force direction, and hence is translated into a torque. This rotation is usually prevented in a large sets of particles because of the friction force that exists at their contact points. In order to alleviate those frictions, a lubricant can be added. The study of Nam et al. [58] used a thermoplastic polymer above

[b] Contrary to rod, where the in-plane orientation obtained is random.

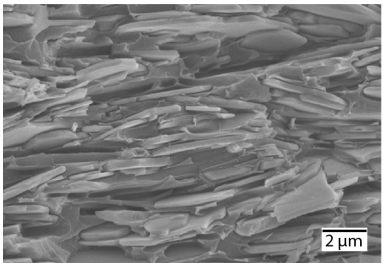

Figure 1.11: SEM picture of the microstructure of a warm pressed alumina platelets/PMMA composite. Reproduced from [58].

its glass transition as a lubricant to prepare an alumina platelets/PMMA composite by warm pressing (see figure 1.11). The difficulty to align alumina particles as well as the non-uniformity in pressure distribution during uniaxial pressing prevents a high platelet's content, thus limiting the improvement obtained by this method so far.

1.7 Natural materials as a source of inspiration

In the previous sections were described the different ways engineers have at their disposal to obtain architectured materials by self-assembly. Those techniques can control the architecture of materials at different length scales, from the molecular to the macroscopic level. Their combination, when possible, provides hierarchically organized materials. For instance, the presence of hierarchical porosity in catalytic support [15] can increase the catalytic activity, or the hierarchical stiffness that protect stretchable electronics circuits from damage [59]. An increasing number of concepts in materials and chemistry sciences are found by mixing different materials at different levels. This trend came along with the better understanding of natural materials organization. They provide design guidance and puzzle, their properties being sometime astonishing, but their formation and architecture being indubitably complex to understand and challenging to reproduce. In this section some characteristics of natural materials and why they are interesting examples are detailed, (see chapter 6 and section 4.3). Biomineralization, because it is one of the most complex and effective self-assembly process known to date, is briefly discussed.

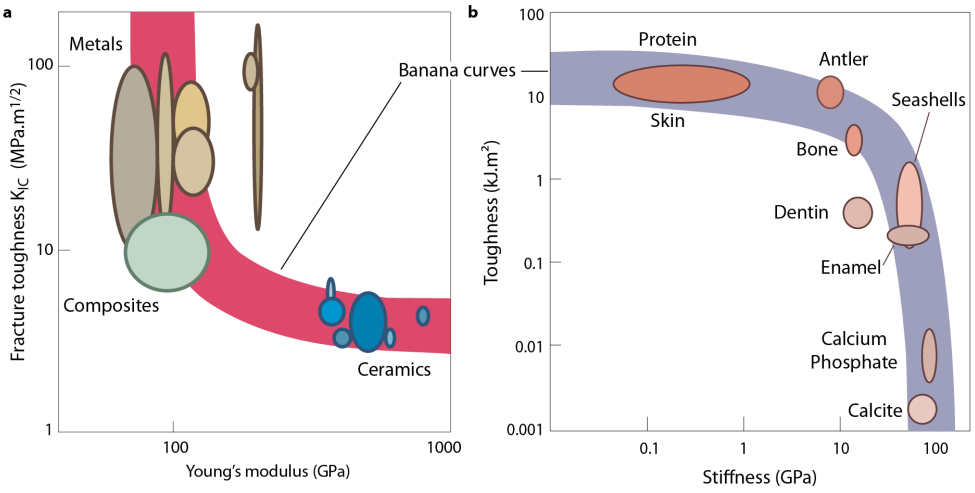

Figure 1.12: **Ashby maps (stiffness versus toughness) of two different systems with their respective "banana curves".** a) Map of man-made materials, showing that rigidity (but also strength) and toughness are mutually exclusive. b) Map of materials present in biological systems. Even if weaker components are used, they combine the toughness and stiffness of their individual parts. Reproduced from [60].

1.7.1 Bioinspiration: why and how?

When talking about bioinspiration, the scientific community is divided by fields of interests. Research in chemistry for instance is more interested in the small and organized porosity found in silica diatom [61] whereas material researchers are gazing at the mechanical properties [62]. These boundaries are however more and more blurred, because the formation of the structurally interesting natural materials is based on chemical processes and present multiple functions [c]. Bioinspiration is thus by definition a multidisciplinary research field. This section will be treated from the mechanical point of view, mainly because the bio-inspired structures shown in the next chapters fall into this field.

The stiffness and toughness of man-made materials and natural materials are plotted in 1.12. The synthetic materials follow a curve (sometimes called "banana curve") that represents their mutual exclusiveness, a gain in one property come at the expense of another. Engineering materials are most of the time used as bulk materials so their properties are intrinsic. For instance, the toughness (or ductility in this case) is higher in metals because of the metallic bond between the constitutive atoms. This bond is unidirectional and sufficiently weak to permit dislocation movements. At the same time, because of this lower energy bonding, the Young's modulus is lower (as well as the thermal stability). Most of technical ceramics [d] present iono-covalent bonding, which is stronger and directional, preventing any dislocation movement. Subsequently those materials are stiffer but also more brittle.

Natural materials combine mineral and organic components. Because they use quasi exclusively materials readily soluble in water, their organic parts are usually constituted of proteins (like chitin and collagen) and the mineral parts are ionic species present in water (mainly calcium, phosphate, silicium and carbon). They are represented in figure 1.12 at the extremities of another banana curve. The behavior of the composites is radically shifted (thus fall on a reverse banana curve). Because of the way these composites are organized, the presence of the mineral phase increases the stiffness without impinging on the toughness. The concept of bioinspiration, at least for mechanical properties, is thus to build upon the architecture of natural materials but with higher performance constituents. Various fields are in need of such composites.

How we can mimic the architecture of natural materials? The first step is to understand where their intriguing properties come from. The bone and the nacreous

[c] A structural natural material carries also a biological functions, such as bone that provides a resistant scaffolds for biological flux [63, 34].

[d] Here, ceramics that are not use for construction.

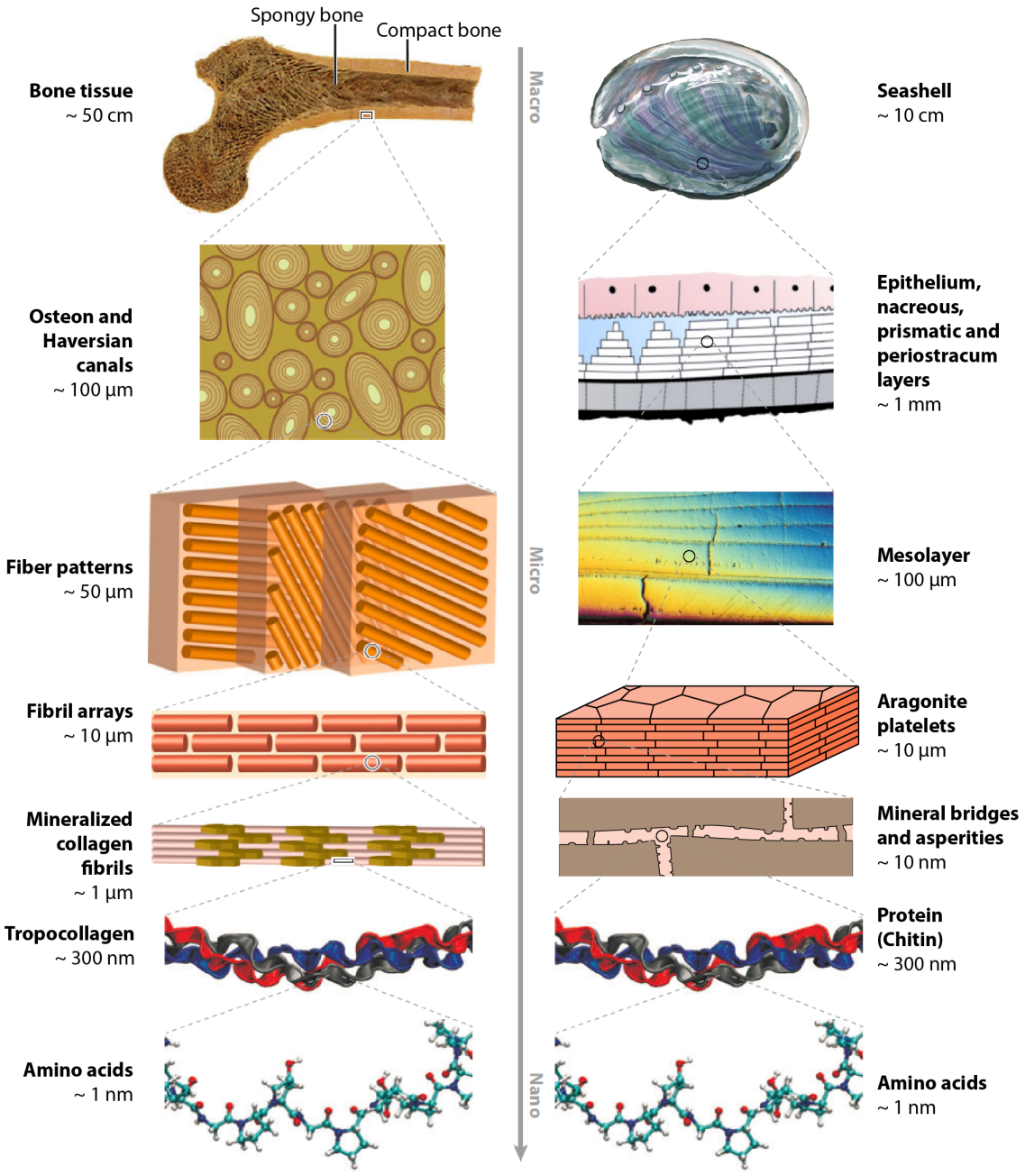

Figure 1.13: Multiscale structure of bone (left side, adapted from [64]) and nacre (right side).

layer of seashells are probably the two most studied natural materials. They both present a hierarchical structure with many different levels, from the macroscopic scale to the nanoscopic one (see figure 1.13). The two elementary components are similar, the organic phase consists in proteins (different collagen for bone and chitin for the nacre) and the calcium phosphate and calcium carbonate for bone and nacre respectively. Those two parts are combined at the nano scales with different ratio, from to 60 % to 90 % mineral content for bone and a higher content (95 %) for nacre. The building blocks are composite materials, with troppocollagen fibril intertwined with calcium phosphate nanoplatelets (2 nm to 5 nm thick to 15 nm to 25 nm large) in bone and aragonite (metastable phase of calcium carbonate) tablets (500 nm, 7 µm wide) embedded in a thin layer (20 nm) of chitin.

The most striking feature that most of the natural structures share is their anisotropy. The tablets in nacre are oriented perpendicular to the surface (see figure 1.13) so that a crack coming from the outside of the shell will have more difficulty to propagate to the inner side, ensuring the protection of the mollusk [60, 65, 66]. The structure of bone is even more anisotropic. The mineralized fibrils are aligned in arrays, that are themselves stacked together. The orientation in those layers evolves depending on the main solicitation the bone undergoes (parallel to the stress to provide strength or tilted for bending resistance), similar to laminate composites but at the micrometer scale [64, 67, 68].

The stiffness in those materials is thus obtained by orienting the building blocks in the direction of solicitation. In addition they are dynamically remodeled in response to the applied stress field [69]. Their other distinctive feature is their remarkable resistance to crack propagation. Indeed, even if they are mainly constituted of brittle materials, their toughness is orders of magnitude above that of either individual constituents [70]. The reason of this increase resides in numerous mechanisms that dissipate the energy ahead of the crack tip and by doing so prevent any catastrophic failure. Bone present many intrinsic (like collagen unfolding, tablets sliding) and extrinsic toughening phenomena (crack deflection at layer interface, crack bridging) responsible for this exceptional improvement in toughness [64]. The main toughening mechanisms in nacre are extrinsic, such as crack deflection at interfaces, tablet sliding and interlocking [71], mineral bridges breaking [72, 73]... Interestingly, each level of hierarchy plays a role during a crack propagation, in addition to their biological properties. Another well-known example of hierarchical architecture that induces toughness is that of a sea sponge [74], the *Euplectella sp*. This sponge is nearly entirely constituted by consolidated silica spheres (see figure 1.14i), and yet is damaged tolerant and highly flexible, because of the way those fibrils are arranged and the thin concentric ring of organic phase (see

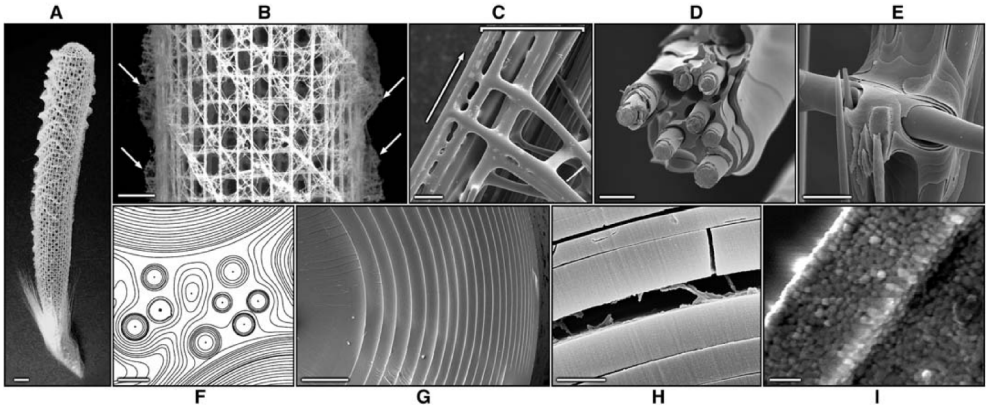

Figure 1.14: Hierarchical structure of *Euplectella sp*. Scale bars: a) 1 cm, b) 5 mm, c) 100 μm, d) 20 μm, e) 25 μm, f) 10 μm, g) 5 μm, h) 1 μm, and i) 500 nm. Reproduce from [74].

figure 1.14g and h) separating silica layer.

1.7.2 Biomineralization

Through the few examples shown above, we saw that the delicate interplay between the organic and mineral phases at all scales represent one of the most critical factors leading to the improved properties of natural materials [75]. This aspect, along with the anisotropy of the structure arises directly from the way these materials are formed. If we go back to the definition 1.1, biomineralization, because it is a phenomenon that involves different biological agents and chemical reactions, is a dynamical self-assembly process. This part, as mentioned previously, is extremely complex and not all the processes involved are unraveled yet. This section describes, through the same examples as previously (bone and nacre), what is known about this natural self-assembly so far. The growth mechanism of nacre has been extensively studied [76, 77, 66]. Images of growing nacre (see figure 1.15) reveal that the organic layer is built first, before the aragonite crystals. The organic part is constituted of polysaccharides and proteins fibers laid down orthogonally to each other and aligned with the aragonite crystal axes. Holes in this layer ensure a continuity of the mineral phase because they allow the formation of mineral bridges between tablets. Those bridges play a key role in crack resistance [72, 73] but at the same time probably act as nuclei for the layer above, preventing another crystals departure in an undesirable location.

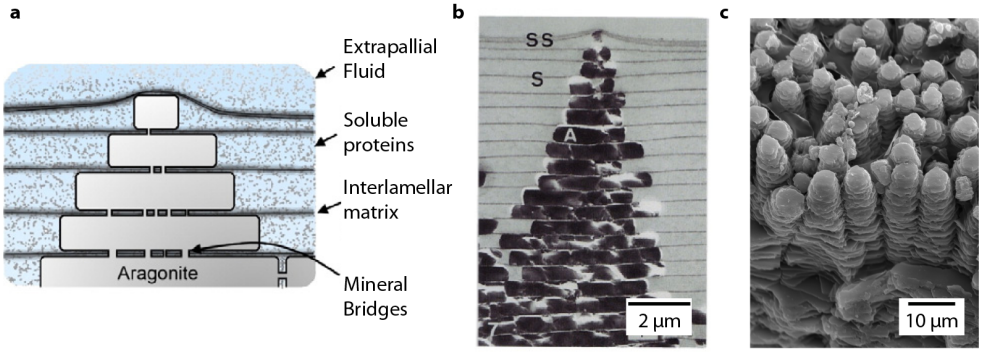

Figure 1.15: a) Schematic representation and b) TEM images of growing nacre. Reproduced from [66]. c) SEM pictures of the inner side of seashell.

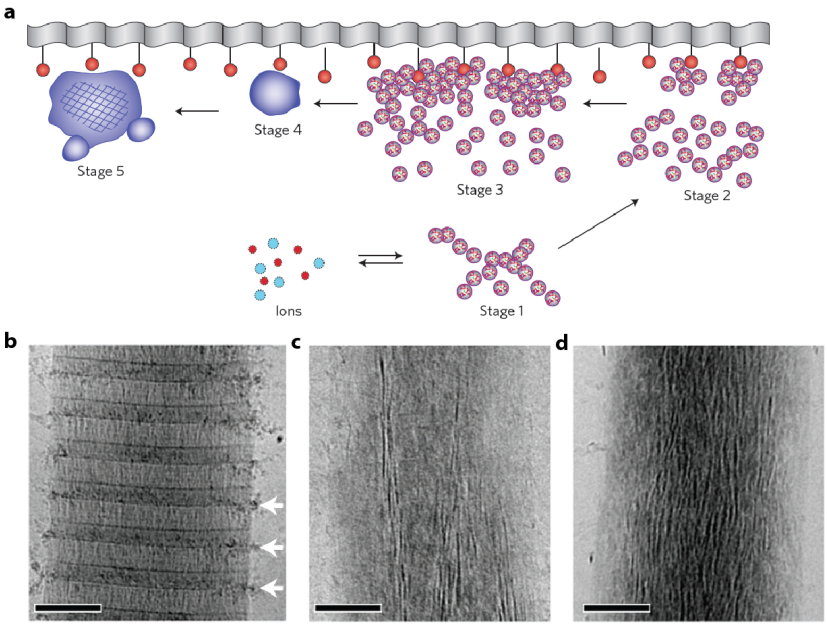

Figure 1.16: **Surface-directed mineralization of calcium phosphate.** a) The five different stages of bone mineralization. CryoTEM images of collagen at different stages of mineralization. b, 24h. c, 48h. d,72 h. Scale bars: 100 nm. Reproduced from [78, 79, 80].

A recent study [78, 79, 80] reported the result of mineralization of collagen fibrils in simulated body conditions. The figure 1.16a summarizes what researchers have figured out about the mineralization mechanisms so far. The main idea is that concentration of ions has to be far from the point where they can spontaneously precipitate. Ion clusters are however present in solution and when they get in contact with the protein at the surface of the collagen, they stay because of chemical affinity (and functionality) (stage 1, 2, and 3 1.16a). Finally nucleation and crystallization occurs (stage 4 and 5). In bone's collagen, surface proteins are organized in bands (visible in 1.16b) with alternate surface charge that guides the ionic clusters into the fibrils. Crystal nucleation occurs only in selected areas and where those crystals meet, they finally merge to form nanoplatelets [79] (see figure 1.16b, c and d).

All these individual stages have been more or less reproduced synthetically using molecules self-organization on surfaces. It has been shown that chemical functionality and molecule spacing on the surface can influence the crystal formation, by changing its orientation and lattice [81, 82]. All these aspects tend to confirm the mineralization scheme proposed for bones, but also explain why platelets in nacre are made of nearly perfectly oriented nanoparticles of aragonite (and not calcite) [60].

The hierarchical architecture of natural materials is finally a reflection of the hierarchical phenomena that occurs during their formation. The organic part is self-assembled into organic layers or fibrils with patterned molecular surface with changing chemistry and charges. Then this mineral grows in patterns defined by the self-assembled organic part, leading to an intricate microstructure responsible for their impressive properties. From the materials engineer's point of view, the growth rate (several weeks to form nacre layer [83] for instance) and materials combination represent great limitations, no matter how astonishing and complex those structures are. Processing shortcuts needs to be found to obtain similar structures but with stronger raw materials. The aim of bioinspiration is therefore to combine the best of both worlds. At least until we find a way to control the bottom-up formation of different materials similarly to natural species.

1.8 Ice-templating as a tool to create architectured materials

Ice-templating (*aka* freeze casting) is a process that takes advantage of the growth of ice in suspensions to template the pore structure in materials. Because of the scale where this process takes place, it can be one of the shortcuts needed to obtain

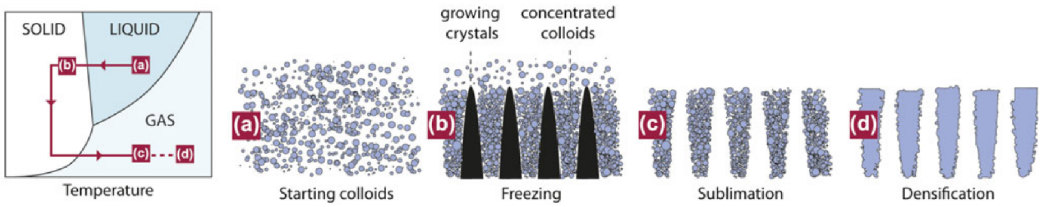

Figure 1.17: Schematic diagram of the ice templating process.

bioinspired materials. This section aims at briefly describing the process and its characteristics (complete reviews are available [84, 85, 86]) along with its contribution to the bioinspiration field. Ice templating has been used in this work as a tool to form various materials by self-assembly (bioinspired or not). The final section will thus describe the state of the art in terms of self-assembled materials obtained by ice templating.

1.8.1 The principle

The principle of ice templating is simple; it consists in a directional solidification of suspensions, which creates crystals that grow along the thermal gradient direction. This solidified solvent is then removed by sublimation, leaving a porous structure that is the negative of the crystals (see figure 1.17). The material in suspension can be practically of any nature, from polymer, metal, ceramic or precursors, as long as it is small enough (under tens of microns), dispersed or soluble. The solvent rejects what is in the suspension independently of its nature and thus the final material is constituted by every element present in the starting suspension or solution. This gives a great opportunity to mix and aggregate all the different constituents of a material (or a composite) in a single step. This process is mainly considered as a phase separation, where the ice is thermodynamically more stable when pure and so rejects all the others species up to the point (usually at a fraction near the random close package for particles [87]) where it becomes favorable to create numerous interfaces and engulf the segregated part.

1.8.2 ...and its characteristics

The first use of ice templating was to obtain porous samples with a unique and highly anisotropic structure [88]. Because the crystals grow from one side to the

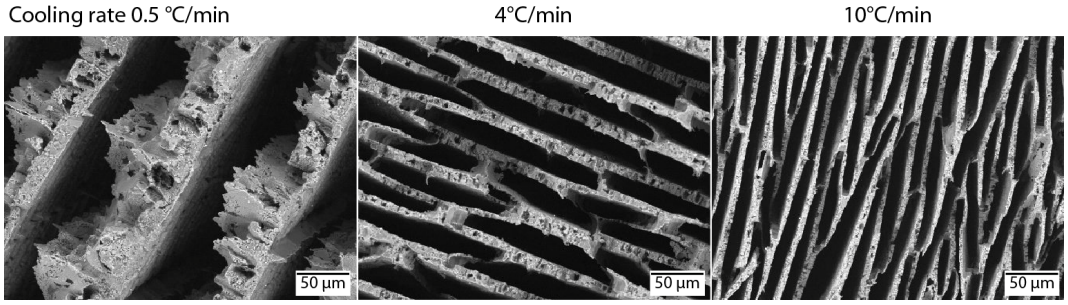

Figure 1.18: Cross section of ice templated samples at different cooling rate, made of 17 vol% suspension of zirconia in water.

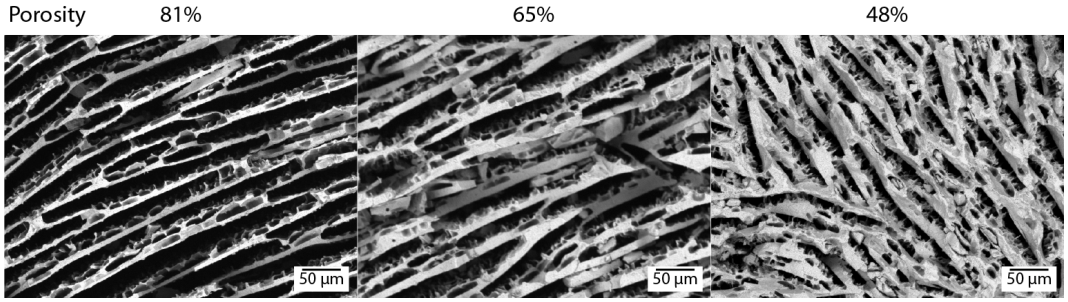

Figure 1.19: Cross section of ice templated zirconia samples at different volume fractions, obtained with a 2°C/min cooling rate.

other, the porous structure is constituted of low tortuosity channels[e]. The main parameters that influence the pore size and quantity are the cooling rate and the solid loading of the suspension.

The ice front velocity dictates the size of the crystals by changing the undercooling degree of the suspension and the interface stability. The velocity is controlled by changing the thermal gradient (experimentally the cooling rate) of the setup. Examples of such variations are shown in figure 1.18. The size of the wall can be varied over nearly an order of magnitude (from around 60 µm to 6 µm [89, 90]), but process limitations occurs when the velocity is either too fast (usually superior to 80 µm/s) or too slow (below 5 µm/s).

[e]As opposed to the ones obtained by conventional methods such as pore formers or foam replication.

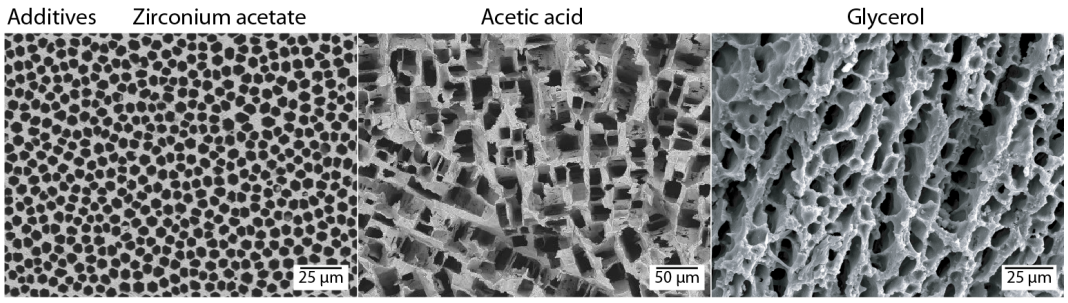

Figure 1.20: Cross section of ice templated ceramic samples comprising different additives.

The solidification front velocity modifies the periodicity of the structure (the length of a pore and a wall) but the size of the pore (respectively the wall thickness) can be tuned by changing the amount of solid in suspension. In figure 1.19 are shown different microstructures with different amounts of powder in the initial solution. The porosity content obtained can typically vary from 90 % to 40% [f] to obtain samples that can be easily manipulated.

The pore morphology is dependent on the solvent and because the growth rates of the different crystalline planes of ice are different, a lamellar pore morphology is usually obtained. Camphene-based suspensions lead to a dendritic pore morphology [84] while ter-butyl alcohol leads to hexagonal pores [91, 92]. With the same solvent, pore morphology can be changed by the addition of additives, modification to the support [90] (see figure 1.20) or the presence of an electric field [93]. In a more complex way, the pore morphology of water based suspensions can be dramatically changed by the addition of a metallic salt, the zirconium acetate [94] (see figure 1.20). The way additives interact with the process is not yet fully understood. They can both act on the solidification front and particles interaction or even on the viscosity of the medium. We nevertheless have enough knowledge now to adapt the structures as required thanks to those different additives, even if we do not know exactly how they influence the process.

[f] Those values are valid for ceramic slurries and to obtain mechanically stable samples (fibers can be obtain with a few percent solid loading). The use of polymer can lead to a higher porosity. When higher solid loading is used, the technique can be used to cast dense samples (hence the name *freeze-casting*).

1.8.3 Freezing and bioinspiration ("Bio-Ice-Piration"?)

As mentioned previously, the first and main use of ice templating is to produce samples with a controlled and anisotropic porous structure. Because of this anisotropy, it can be related to natural porous structures, like bone or wood (see section 4.3). The main application is consequently related to bone substitutes [95] or improve the support for gas separation [97] (because of the low final tortuosity).

The pore architecture being lamellar (when water is used), the resulting structure can also be compared to the nacre brick and mortar organization when the pore are aligned over large distances. The control of lamellae orientation can be achieved by modifying the freezing setup. Different methods have been proposed so far in the literature [90] but unfortunately have proven hard to replicate. The first step toward nacre-like materials by ice templating was made by filling the pores with a ductile phase (polymeric or metallic) (see figure 1.21a and [1, 98]). The role of interfaces appeared critical for the final properties (see figure 1.21b), but the low fraction of ceramic severely limits the strength of those materials. One further step was done when the mineral content was improved [96] by adding several processing steps, comprising several pressing and thermal treatment sequences. The resulting composite presented a higher mineral content (close to 80 %) but also an improved adhesion of the polymeric phase (by surface grafting). In addition, it shared several features with its natural model (see figure 1.21c). The crack propagation resistance of the composite is dramatically increased compared to both constituents (see figure 1.21d) and is even better than in nacre.

Those two examples paved the way for several more studies and materials and are still considered as reference of bioinspiration in the literature [62, 99]. On the other hand, the elementary building blocks of those materials rely on the lamellae created by ice templating. This structural element size directly depends on the ice front velocity and its thickness is therefore limited to a few microns. We saw that natural materials possess several hierarchy levels to multiply interfaces hence improving their toughness (see section 1.7.1). One way to overcome this intrinsic limitation is to stop using lamellae as building blocks and use instead the growth of ice to organized smaller building blocks.

1.8.4 Self-assembly driven by the growth of ice

If we look from the point of view of self-assembly, this process directly falls into the dynamical category (1.1): the spatial arrangement of all the species occurs here with an energy dissipation (the latent heat of solidification for instance). Those systems (see 1.1) are extremely complex but are getting more and more attention. The ice

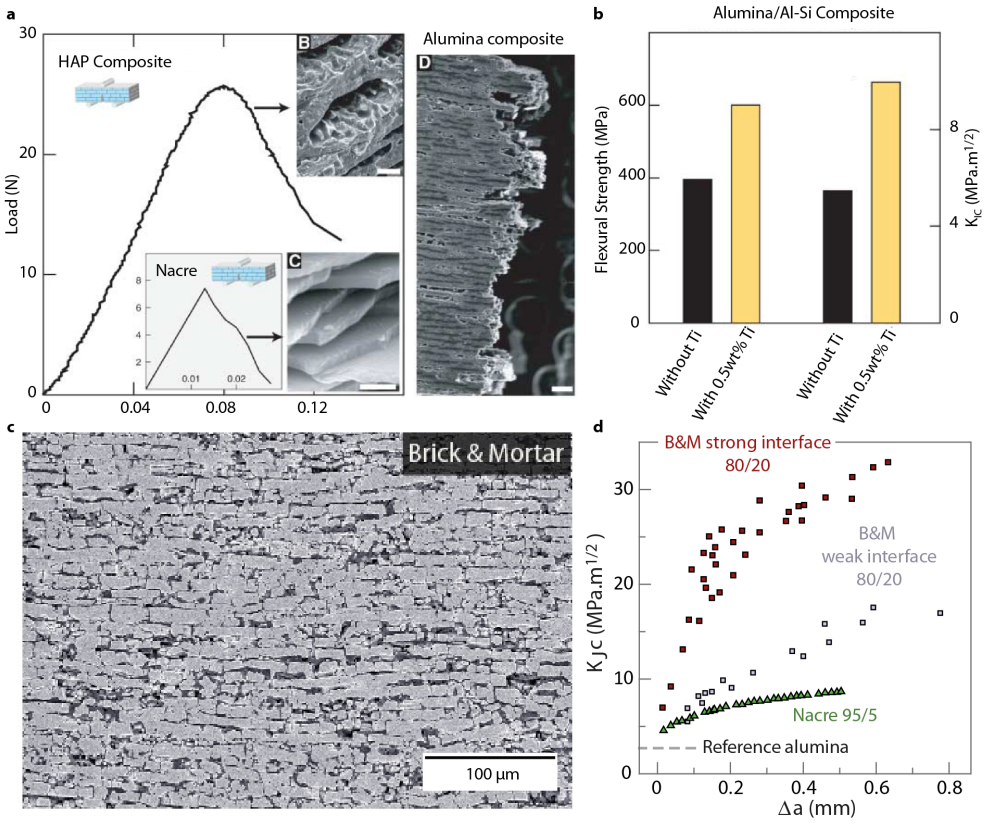

Figure 1.21: **The two main examples of bioinspired materials by ice-templating.** a) Load-displacement curve of ice templated composites and their microstructure b) Mechanical properties of ceramic-metal composite with different interfaces c) Brick and mortar composite of alumina and PMMA d) R-Curve behavior of the brick and mortar composite. The number represents the fraction of mineral and organic part in the composite. a and b are reproduced and adapted from [95]. c and d are reproduced and adapted from [96].

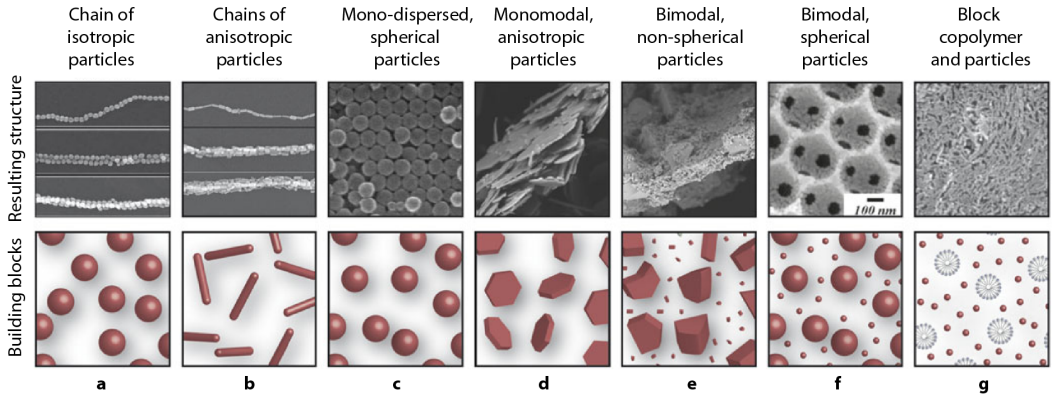

Figure 1.22: Self-assembly of different building blocks induced by the growth of the surrounding ice crystals. Reproduced from [100].

crystals that grow in the medium concentrate the different components before eventually engulfing them. This concentration occurs at a length scale where it can be used as a driving force to organize the constituents, depending on their intrinsic properties and characteristics. It constitutes though a case of static self-assembly (1.1), similar to the others techniques detailed in this chapter. This process is a (hierarchical) combination of static and dynamic self-assembly.

Probably one of the first case of self-assembly by ice templating is the alignment of clay particles in the study by Hwang et al. [101], even if it is neither measured or nor mentioned. Several other studies point toward the evidence: ice templating is a robust way to organize particles [100] (see figure 1.22). The use of monomodal spherical particles lead to walls constituted of colloidal crystals (figure 1.22c). Exactly like the evaporation method, the concentration rate (and therefore the cooling rate) must be carefully controlled to obtain particles ordering. By lowering the solid content, monofilaments of particles can be obtained (see figure 1.22b and c). Faceted particles, such as platelets, are also aligned by the freezing front (see figure 1.22d), independently of the material (for instance graphene layers [102] and alumina platelets [103]). Block copolymer self-assembly is also possible (see figure 1.22g), leading to hierarchical porous structures. Self-assembly at different length scales can be combined, as shown by Kim et al. [104], where small silica particles are ordered in between colloidal crystals of large (400 nm) particles (see figure 1.22f).

All the materials obtained by this method present roughly the same microstructure of straight pores and walls. Those walls can present an organization of smaller building blocks. Because the two intricate self-assembly processes can be modu-

lated separately (under certain conditions), this technique is a powerful and versatile tool to obtain sophisticated structures defined at several length scales. Because the static self-assembly seems guided by the same global principles than for the other processes detailed previously, freezing can benefit from the experience already accumulated. The next step could be the better understanding of the dynamical aspects to further tailor material constitution.

1.9 Conclusions

Self-assembly, as a research field, is ubiquitous and complex. Only a small part have been described in this first chapter, but by doing so we have spanned several length scales (from molecular level to macroscopic level), build hierarchical materials to finally found that evolution have lead to some outstanding examples of architectured materials. The use of self-assembly indeed provides leverages to create complex and intricate structures and the study of natural materials can provide the necessary guidelines to optimize our processes and materials.

Interesting microstructure are provided by natural materials and the resulting properties are the witnesses of the progress made. In this jigsaw, the missing piece is the process. Self-assembly have been developed to palliate the lack of control upon materials organization at the micron scale. However, the materials obtained are most of the time of small dimensions, and rather two dimensional because it remains hard to carefully control larger systems [g]. Ice-templating can fill the gap between the local self-assembly phenomena and large three-dimensional pieces (centimeter sized), at the expense of the creation of porosity. The concentration that occurs between two adjacent ice crystals is on the order of a microns, but samples of several centimeters are easily processed. In this manuscript we demonstrate the use of this technique on a particular type of self-assembly, the alignment of large (above a few microns) platelet particles. But the principle are similar for other systems, and the ice growth can trigger other types of self-assembly, such as colloidal crystals or molecular templates [100].

Ice-templating process has been linked to bioinspiration for a while, because of the similarity that exists between the architectured sample and some well know natural materials. Because the final materials present a directional porosity, it seems like a good start to produce bone substitutes. The similarity with nacre have also conduced to two studies, still considered as a reference of bioinspiration years after

[g] In most case films are obtained, as with molecular assembly, tape casting or layer by layer deposition.

their publication [1, 96]. Those materials paved the way to develop more resilient ceramic/polymer composites at a scale unachievable before and represent a proof of concept of the use of ice templating as a process to make composites materials.

Several issues have limited further developments, such as a multiple steps processes hard to replicate or intrinsic limitations of walls thickness (cf. section 1.8.3). Still, plenty of room exists to simplify the creation of those materials and further improve their properties. The limitation in wall thickness can be overcome by trading the building blocks for smaller ones. The presence of a polymer, used as interfacial material, severely limits the operative conditions (usually the asset of ceramics) of such composites. The creation of fully ceramic composites inspired by the microstructure of nacre can be highly beneficial, for two main reasons: they could be used in extreme operative conditions and at the same time be obtain through a much simpler process. The development of such materials constitutes the final goal of this study and can lead to composites presenting both high strength and high toughness.

Chapter 2

Suspension's optimization

2.1 Introduction

In this chapter the two main types of suspensions developed to be used in the rest of the manuscript are described. Those slurries are specifically designed to be shaped by ice templating, which implies several considerations, such as being fully dispersed and stable versus sedimentation during the time where the freezing takes place (up to one hour). The first part concerns the aqueous dispersion of boron nitride with a new dispersant, a cellulose ester. This part has been published as an article in the *Journal of the American Ceramic Society* (cf. publications list page viii). The second part explores the co-dispersion of alumina platelets and additives later necessary for the synthesis of the material in the chapter 4 and 6 and their stabilization versus sedimentation.

2.2 Dispersion of boron nitride with cellulose

Hexagonal boron nitride (BN) exhibits a unique combination of high thermal conductivity, high resistance to thermal shock, high thermal/chemical stability, and low surface energy. These properties arise from its crystalline structure [105]: covalently bonded boron and nitrogen that forms layers that are weakly bonded by Van der Walls forces. The structure is similar to graphite but electrically insulating [106]. Because of its low surface energy, BN is particularly useful in applications involving liquid metals handling where it acts as a barrier to prevent corrosion and contamination. Such benefits are also particularly useful for high temperature crucibles [107]. These two main applications usually rely on aqueous powder processing

Powder	BN-16			BN-8			BN-1		
$D_{10}/D_{50}/D_{90}$ (μm)	7	16	31	4	8	18	0.2	1	3
Thickness (μm)	1			0.54			0.06		
Surface Area m^2/g	2			4			20		
B_2O_3 content $wt.\%$	$< 0.1\%$			$< 0.1\%$			$< 0.1\%$		

Table 2.1: Characteristics of the boron nitride powders

routes, to cast a preform or deposit a coating. The low sinterability of BN requires the use of densification techniques such as hot isostatic pressing (HIP) in presence of sintering additives [108, 109].

Unfortunately, the low surface energy of BN is a major drawback for its use in aqueous media [110], because it is not easily dispersed. This dispersion issue often results in heterogeneities in the green body, both in terms of particles packing density and sintering additives. An effective dispersant could allow the use of highly loaded suspensions with a homogenous mix of BN particles and sintering additives. The final ceramic parts could therefore present more homogenous microstructures and thus improved mechanical properties. Cellulose derivatives are usually added in suspension as thickening agent, to prevent the settling of large particles. We demonstrate through zeta potential, viscosity, and adsorption measurements that cellulose are also efficient dispersants of BN particles in aqueous suspensions.

2.2.1 Experimental procedure

BN powders were provided by Saint-Gobain BN products (Tres BN series). Those powders are mainly used in cosmetics products and thus present a relatively high purity and crystallinity, but also low boric acid content. The main characteristics of the different powders are given in the table 2.1.

The granulometric distributions have been obtained by laser granulometry, which assumes a relative sphericity of the particles. The equivalent diameters measured are the diameter of the platelets, values confirmed by SEM observations. The thicknesses of the platelet have also been evaluated by the same method.

Two types of cellulose were tested: a hydroxyethyl cellulose HEC (Tylose H 4000 P2 from ShinEtsu, Mv = 720 000) and methyl cellulose MC (Methocel A4M from Dow Chemicals, Mw = 88 000). The celluloses present the same viscosity of 4 $Pa \cdot s$ at 2 wt.% in water but their structures are different, the MC is more hydrophile than the HEC. The suspensions were prepared by mixing the powder, the cellulose,

and distilled water with a magnetic stirrer or a propeller mixer depending on their viscosity. Suspensions with hydroxyethyl cellulose were mixed for at least 4 hours to ensure total hydration before being used. Ultrasonic mixing was applied with a sonotrode (Digital Sonifier 250) with an applied energy around 150 $W \cdot h/kg$.

Adsorption isotherm measurements were conducted using a total organic carbon (TOC) analyzer (TOC VCSN, Shimadzu), which provides a quantitative measure of the non-adsorbed fraction of cellulose in solution. BN/Cellulose suspensions from 0 to 1 wt.% of HEC were prepared. After complete hydration and mixing, the suspensions were centrifuged at 7200 rpm for 1h and supernatant aliquots were taken to be analyzed.

Zeta potentials were measured with a ZetaProbe after dispersion of the particles in distilled water by sonication. The pH was adjusted with 1 mol/L hydrochloric acid and sodium hydroxide. To calculate the zeta potential with this technique, the relative sphericity of the particles is assumed. This assumption is not valid with the anisotropic particles used here, so the measured values offer only a qualitative comparison of the zeta potential values between samples. Rheological measurements were performed in a concentric cylinder viscosimeter (Bohlin, Malvern, UK). The suspension was pre-sheared at $100\,s^{-1}$during 30 s followed by 30 s at rest. Two procedures were followed: a shear rate ramp was applied from $0.05\,s^{-1}$ to $600\,s^{-1}$ or a constant shear rate for 1 min. A shear rate of $150\,s^{-1}$was chosen to compare the viscosity of the different suspensions. Most of the suspensions have reached a quasi-Newtonian behavior before this value. This ensures the stability of the measurement.

2.2.2 Results and discussion

Effect of ageing time

A 19$vol.\%$ of BN-16 suspension, with HEC at a powder ratio of 0.019, was mixed by a magnetic stirrer at 800 rpm and a part of the suspensions was taken at different ageing times to perform rheological measurements. The evolution of viscosity versus ageing time is plotted in figure 2.1. The viscosity decreased by a factor of six just by maintaining the stirring for fifteen days. The final viscosity was even slightly below the viscosity of the solvent with the same amount of HEC (0.11 Pa.s for the slurry and 0.15 Pa.s for 1 wt.% HEC solution). The evolution could be explained by the adsorption of the cellulose on the particle surfaces. This phenomenon could help the breakage of agglomerate, and thus could reduce the suspension viscosity.

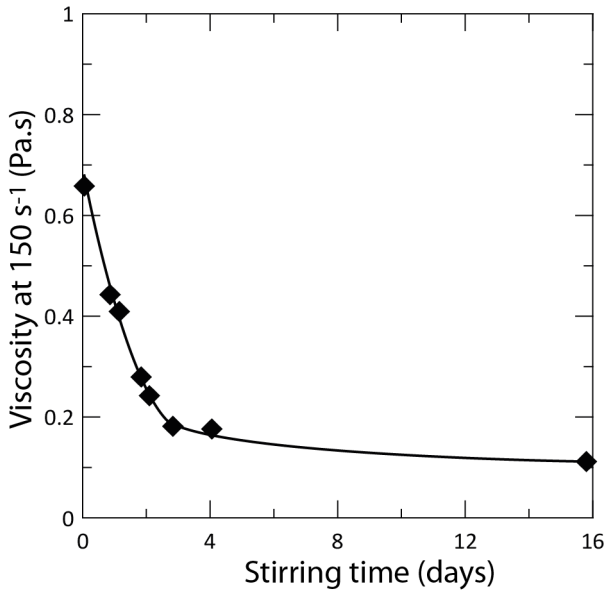

Figure 2.1: Viscosity *vs* the ageing time of 19 vol.% BN-16 suspension.

Effect of the amount of cellulose

Rheological characterization (figure 2.2) has been conducted on 19 vol.% BN-8 and BN-1 suspensions with HEC to powder weight ratio ranging from 0 to 0.03. Concerning the BN-1 suspensions, only the HEC/BN weight ratios of 0.01, 0.02, and 0.03 were tested because the suspensions corresponding to the other ratios presented a viscosity too high to be assessed by the concentric cylinder rheological setup.

Repeated HEC additions minimized the viscosity of the suspensions for both particle sizes. After this minimum, the viscosity increases at different rates for the various particle sizes. The optimum weight ratio of HEC/BN is 0.0025 for 8 μm powder and 0.02 for 1 μm powder. The presence of a viscosity minimum is generally associated with a ratio where the dispersant molecules cover the maximum of particle surface without any excess in the suspension [111]. If we assume that HEC acts as a dispersant for BN, this particular ratio must be constant with the evolution of surface area. Suspension viscosity evolution versus HEC/powder ratio divided by powder surface area is shown in figure 2.2b. The minimum viscosity is reached at almost the same ratio for both powders, which is consistent with an optimum repartition of a dispersant on particle surface, independent of its size.

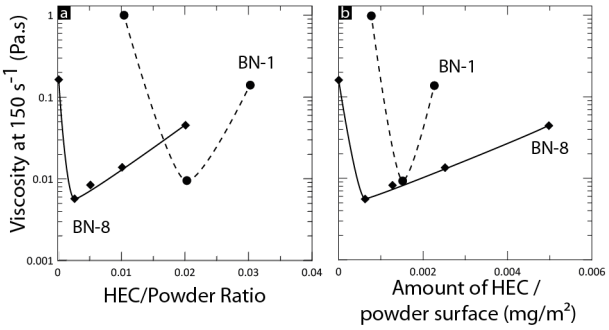

Figure 2.2: a) Effect of HEC/Powder weight ratio on different sizes of boron nitride particles. b) Effect on viscosity of HEC/powder ratio divided by powder specific area.

Isotherm adsorption of cellulose

The adsorption isotherm for HEC on BN-8 is plotted in the figure 2.3. A nearly total adsorption on the surface (>90% for 10 mg/m^2) is observed for a relatively low amount of cellulose added (1g/L corresponding to a HEC/powder ratio of 0.0025). Then the adsorbed amount reaches a plateau at 15 mg/m^2 when more cellulose is added. Those value are relatively high, compared to the typical value of well-known systems such as poly(acrylic acid) (PAA) on oxides, that are around 1 mg/m^2 [112, 113]. This quantity is usually related to the polymer conformation on particle surface, the more the polymer is stretched, the lower the concentration needed to entirely cover the surface. However, the cellulose used here presents chains nearly an order of magnitude longer (the molecular mass is MV = 720 000) than the usual dispersant used (MW around 10 000 for most of the commercially available PAA). This amount could come from the larger number of cellulose chains needed to cover the surface. The large molecular weight could also explain why a full coverage is not achieved. The cellulose derivatives are effectively adsorbed on boron nitride platelet and thus play the role of a steric dispersant.

Effect of of cellulose on zeta potential

Due to the low boric acid content (<0.1 wt.%), zeta potential of these BN particles is low, between -8 mv to -20 mV. Only the boric acid present on particle surface exhibit hydroxyl groups and thus can induce surface charge changes with the pH [114]. This behavior has also been reported by Crimp et al. [110] with two different powders of different boric acid content in aqueous suspension. The higher the surface charge,

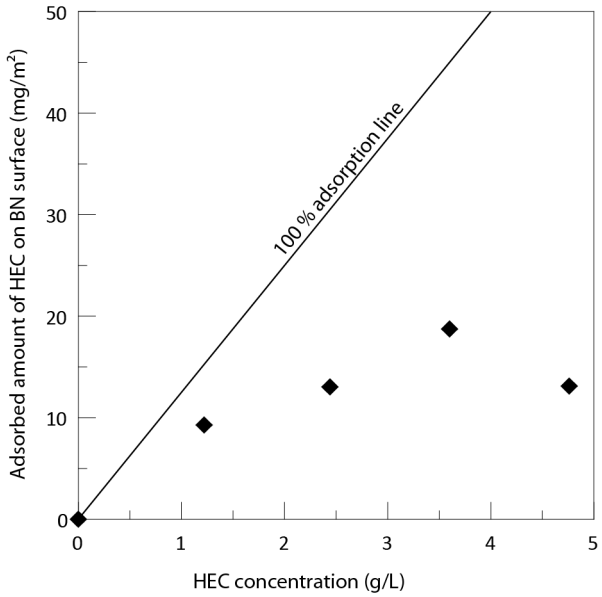

Figure 2.3: Adsorption isotherm of HEC on BN-8 surface.

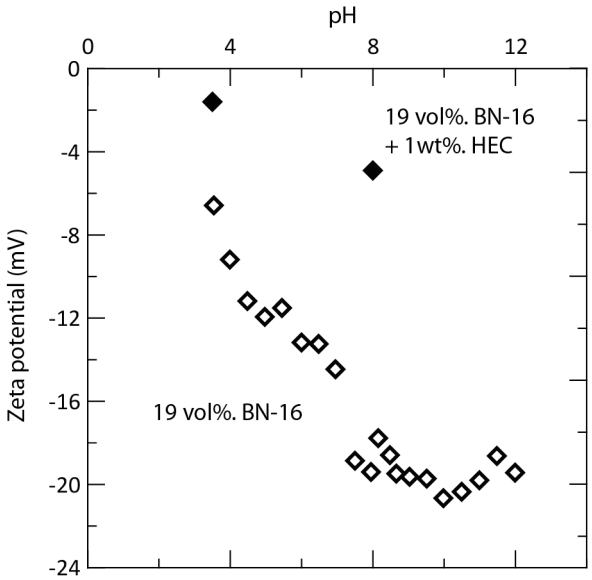

Figure 2.4: Effect of HEC on Zeta potential BN particles.

the higher the oxygen content. However, the addition of the HEC decreased the zeta potential from -20 mV to -4 mV at the solution pH and at pH 4. The decrease in zeta potential is usually associated with a more agglomerated state of particles, which induces higher suspension viscosity, but HEC addition lowered the viscosity (figure 2.4). The addition of this type of cellulose possibly masks the surface charge, thus lowering the zeta potential, and acts as a steric barrier to prevent agglomeration.

This behavior of polysaccharides has been observed previously by Wang and al. [115] with clay and ethyl (hydroxylethyl) cellulose. Clay particles have a flake morphology (a few microns in diameter and a hundred of nanometer in thickness) with a flat surface usually presenting a low negative surface charge (with a small numbers of hydroxyls groups), while the edges are positively charged (with hydroxyl group). Even if the interactions between cellulose and minerals are not well established yet, the frequently accepted explanation consists in adsorption due to a mix of hydrophobic forces on faces and hydrogen bonding on edges. Wang et al. [115] conclude that hydrogen bonding -thus interactions with edges- is predominant. With BN, edges should not play a key role in interaction due to a different particle size and aspect ratio. A similarity between clay faces and BN can be noticed because none of them present hydroxyl group, and thus, supposedly, the main mechanism of cellulose adsorption on surface is hydrophobic forces. The zeta potential is lowered in neutral to acidic pH range, a range where cellulose is considered stable; a proper dispersion can theoretically be obtained within this range.

Effect of cellulose type on dispersion

Another type of cellulose, methyl cellulose (MC), has been mixed with BN and the viscosity measured under the same conditions. MC was chosen to assess if the hydrophilicity influences the dispersion behavior. The resulting viscosity at different ratio and the data obtained with HEC are represented in figure 2.5.

An optimum viscosity is found for both MC and HEC at different cellulose/powder ratio (0.0025 and 0.005 for HEC and MC respectively). This suggests that the nature and/or amount of cellulose functional groups do not change its capacity to disperse the BN particles. Indeed, if the main mechanism of adsorption is hydrophobic bonding, the nature of cellulose does not have a great impact as long as they have the same type of interaction with the solvent and particle, e.g. the same type of hydrophobic and hydrophilic functional groups. The amount of HEC required is slightly lower, possibly because of a larger molecular mass (Mw = 80 000 for MC and MV = 720 000 for HEC) that leaded to a maximum coverage of the surface with less

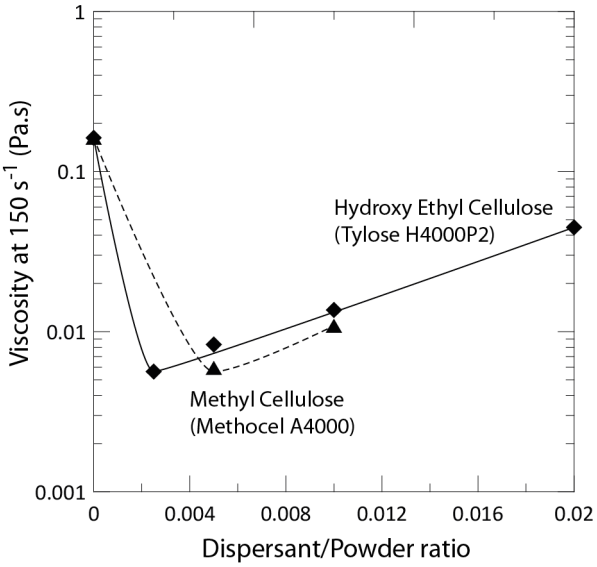

Figure 2.5: Effect of cellulose type on suspension viscosity.

molecules.

Effect of solid loading

The effect of solid loading on the behavior of a suspension is a critical parameter in order to use the slurry in typical ceramic processing, like slip or tape casting. A high aspect ratio of particles is a drawback to obtain loaded suspension because of low packing ability due to a greater steric hindrance. This can be partially tackled if the particle-particle interactions are limited due to an optimum amount of dispersant. In order to determine maximum solid loading of cellulose-dispersed BN, the rheological behavior at different solid loading have been investigated (figure 2.6), using the dispersant / BN ratio obtained previously (figure 2.2). A typical shear thinning behavior is obtained for the three different slurries, due to the breaking of particles aggregates and their alignment along the flow direction as the shear gradient increases [116].

Experimental data are plotted in figure 2.6 for the BN suspensions. For comparison a suspension of BN-8 without HEC at 17 vol.% was also investigated. The suspension without HEC presents a high shear-thinning behavior, its viscosity decreases by two orders of magnitude. The viscosity at low shear rate of the suspension

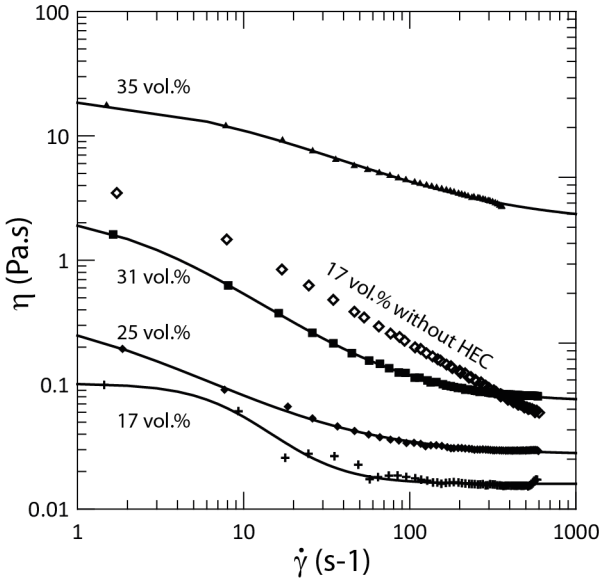

Figure 2.6: Rheological behavior of BN-8 with and without HEC suspension at different solid loadings.

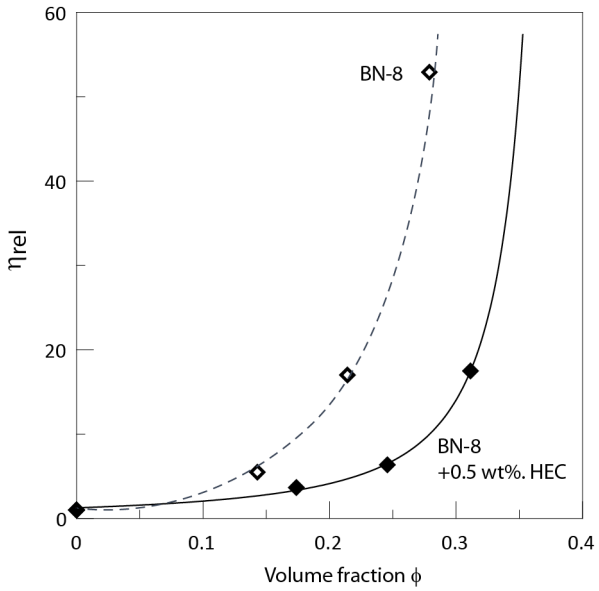

Figure 2.7: Minimum viscosity versus particle volume fraction with and without HEC. The solid line is the Krieger-Dougherty model fits with Φ_m = 0.36 and $[\eta]$ = 3.1 parameters value.

with HEC is more than an order of magnitude lower than the viscosity of the suspension without HEC. The viscosities values of both suspensions get closer as a higher shear rate is applied, probably because the agglomerates are broken by the applied stress. The high viscosity at low shear rate makes it hard to cast the suspension in any mold. The dependencies of the relative viscosity (viscosity of suspension at high shear rates on viscosity of the medium [113]) values with the solid volume fraction Φ are plotted in figure 2.7 with and without HEC. The relative viscosities without dispersant are higher at lower volume fractions (three times higher for a volume fraction of 0.3). The data with dispersant were fitted by a Krieger-Dougherty model [113, 114] (2.1). The high shear-thinning behavior of the suspensions without cellulose additives makes it hard to precisely determine the minimum viscosity and thus to apply the same model on it.

$$\eta_{rel} = (1 - \frac{\phi}{\Phi_m})^{-\Phi_m[\eta]} \tag{2.1}$$

Equation (2.1) allows calculating Φ_m, the volume fraction of particle where the viscosity tends to the infinity. In this equation, $[\eta]$ is the intrinsic viscosity. The intrisic viscosity and the maximum volume fraction are fonction of particle shape. The value of $[\eta] = 2.5$ and $\Phi_m = 0.64$ are obtained with perfectly spherical and monodispersed particles, but $[\eta]$ increases and Φ_m decreases as the particle aspect ratio increases. The value obtained with BN, $[\eta] = 3.1$ and $\Phi_m = 0.36$, are consistent with these evolutions and the values found in litterature with various materials [117, 118]. Barnes et al. [116] found an empirical formula for the intrinsic viscosity evolution with the aspect ratio of disks $[\eta] = 3$ (axial ratio) /10 and leads, in this case, to an aspect ratio of approximately 10, which is consistent with the aspect ratio of 16 for BN particles, considering the high polydispersity of these powders (cf. table 2.1). As described previously, the plate-like shape of these particles prevents a high solid loading suspension.

2.2.3 Conclusions

Hexagonal boron nitride (BN) aqueous slurries can be dispersed using cellulose derivatives. The mechanism of the adsorption on particles surface is not explained in this study although experimental evidences point toward hydrophobic forces. Because cellulose is relatively stable versus pH, the dispersion can be achieved within a relatively large pH range. Obtaining a higher volume fraction could be achieved by adjusting more precisely the molecular weight. A stable dispersion with a high solid loading offers interesting possibilities to obtain homogeneous green bodies with fewer defects, especially when associated with electrostatic dispersion of sintering additives. An alternative to make BN ceramic can now be considered: the use of thermal gel casting. Indeed cellulose ethers form a gel when heated above a certain temperature and thus could directly be used for ceramic shaping.

2.3 Co-dispersion in alumina suspensions

The development of stable and dispersed suspensions of alumina platelets and additives has been necessary to achieve a good control over the microstructure of materials detailed in the following chapters (4 and 6). The use of complex suspensions can lead to materials with interesting properties. However, none of these results would have been possible without a homogeneous repartition of the different components (alumina nanoparticles and liquid phase precursors, silica and calcium carbonate nanoparticles) in between the platelets. Even at a larger scale, the quantity of powder must remain as constant as possible in all sample's height, which implies a

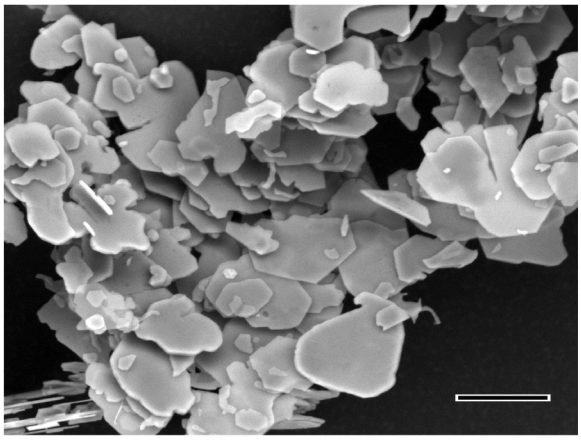

Figure 2.8: Morphology of alumina platelets used in this study. Scale bar: 10 µm.

moderate or no settling of the particles during the whole process time. The settling of particles occurs when the gravitational forces are larger or of the same order of magnitude as the forces induced by thermal motion. A simple energy balance calculation can be made to confirm this assumption.

The gravitational energy U_g needed to lift our alumina platelets (8 μm diameter and 500 nm thick, (see figure 2.8)) of its own size is:

$$U_g = m \cdot g \cdot \Delta h = \pi R^2 e(\rho_p - \rho_w) \cdot g \cdot 2R = 5.9 \times 10^{-18} J \tag{2.2}$$

Where m is the mass of the particle, g the gravitational constant, Δh the distance over which the particles is lifted, R the particles radius, e its thickness and ρ_p and ρ_w the particles and water density respectively. The thermal energy $k_B T$ at room temperature (298K) is $4.1 \times 10^{-21} J$ and thus is clearly lower than the gravitational energy that acts upon the particles. This simple calculus proves that the diffusion of the particles is counteracted by the gravity, which places this type of suspension out of the colloidal suspensions domain. Those platelets settle in water at a rate that depends on the balance between drag forces and buoyancy. This settling rate can be estimated with the Stokes law:

$$w = \frac{2}{9} \frac{(\rho_p - \rho_w)}{\eta} g R_{eq}^2 \tag{2.3}$$

Where η is the viscosity of the medium. The equivalent radius R_{eq} is a combination of the effective diameter, a correction factor that takes into account the particles

shape and the aspect ratio $E = d_{||}/d_{\perp}$ [119]:

$$R_{eq} = f_e d_{eff} = \frac{E^{-1/3}\sqrt{1-E^2}}{2\cos^{-1}E} d_{\perp} E^{1/3} = 3.98 \times 10^{-6} m \tag{2.4}$$

The settling velocity for alumina platelets is thus $w = 5.7 \times 10^{-5}$ m/s. The solidification front velocity during ice-templating is around a few tens of microns per second, so this means that the platelets fall faster than the ice front moves. Plus, the time in which a typical two centimeters size sample is frozen is around 45 minutes at slow cooling rate (-1°C/min or -2°C/min). By comparison, the time for which particles at the top of the mold reach the bottom is slightly more than six minutes (350 seconds exactly).

The settling speed of such micron size particles could be a severe hit to the final sample homogeneity, whatever the processing method. The dispersion of platelets has been extensively studied in clay suspensions, which is a highly specific system, with different charge signs between the face and the edges, and so forms the well-known "house of cards" structures.

The alumina platelets used here are different, because of the crystalline structure, size, and aspect ratio and thus simpler in many ways. Some examples of dispersion studied can be found in literature, either alone [120] or as part of a mixture [121]. In particular, Khoo et al. [120] studied the dispersion of the same alumina platelets with nitric and phosphoric acid [122, 123], two molecules that are known to give rise to strong steric interaction between oxide particles. All those studies lead to homogeneous dispersions but do not address the issues of particles settling.

In this part we developed the study made in order to obtain first dispersed slurry of alumina and additives needed and then how the settling issue was solved.

2.3.1 Study of the platelets and additives surface charge

The zeta potential of alumina platelets was measured by an electroacoustical method (with a Colloidal Dynamic's Zetaprobe, see 2.2.1 for further details). By comparison, and because final suspensions will use it, the surface charge of α-alumina nanoparticles was also measured. The results obtained are plotted in figure 2.9a. The zeta potential of the platelets similar to that of pure α-alumina [114], with an IsoElectric Point (IEP), point where the negative and positive charge compensate each other on the surface) is close to pH 8. The particles present a small surface charge between 10 mV and -20 mV, which is not sufficient to efficiently disperse them. The nanoparticles presents nearly the same IEP but their surface charge is much higher,

around ± 80 mV. The liquid phase precursors that will be needed are silica and calcium carbonate nanoparticles (for more detailed about material choice, please refer to chapter 6). The zeta potential of the nanoparticles of silica (20 nm diameter, provided by Nyacol) is −40 mV around pH 8. The surface charge of calcium carbonate is also negative over nearly the entire range of pH [124], but the value depends on several external parameters and have not been measured here.

In order to homogeneously disperse the platelets and the nanoparticles, a dispersant must be added, and preferably a dispersant that induces negative charges to be compatible with the others additives. The Darvan 7NS (referred afterward as $D[Na^+]$), an sodium polymethacrylate with relatively long chains (molecular weight of 10 000), was chosen because of its ability to disperse α-alumina particles [112] and its large size that can prevent large particles flocculation. The zeta potential values measured after the addition of the dispersant are presented in figure 2.9b. The surface charges are shifted to negative values around neutral to basic pH thanks to the addition of the $D[Na^+]$. This time the surface charge carried by the platelets is around -60 mV, which is usually considered as sufficient to have a stable dispersion. Nanoparticles present the same behavior, with a negative potential in the targeted pH range.

Finally, all powders present in the suspension are negatively charged, which ensures their mutual repulsion and thus the homogeneity in composition of the final material.

2.3.2 Determination of the optimal amount of dispersant

The addition of $D[Na^+]$ induces the desired surface charges on the alumina particles, but the amount has to be tuned to avoid any excess of the dispersant in the solution during the process. The presence of dispersant or binder can influence the stability of the particles during the freezing, and can even lead to the formation of defects [125]. A methodology has been previously developed and consists in optimizing the amount of dispersant so there is no large excess of it in solution and then add a binder [125]. The binder prevents the flocculation or the particles during the concentration between ice crystals. The optimum amount of dispersant has been determined by rheological measurements at constant shear rate of suspension containing a varying amount of $D[Na^+]$. The resulting deflocculation curve are shown in figure 2.10. For both suspensions the optimum weight ratio of $D[Na^+]$ to powder at those volume fraction is 0.5 %.

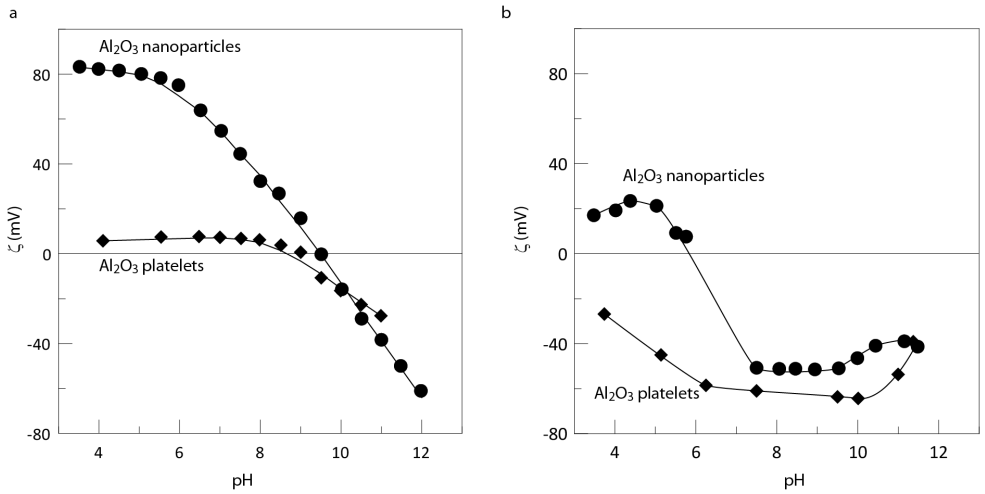

Figure 2.9: Zeta potential of 10 wt.% alumina platelets and nanoparticles as a function of the pH with a) no dispersant b) 1% powder ratio of $D[Na^+]$.

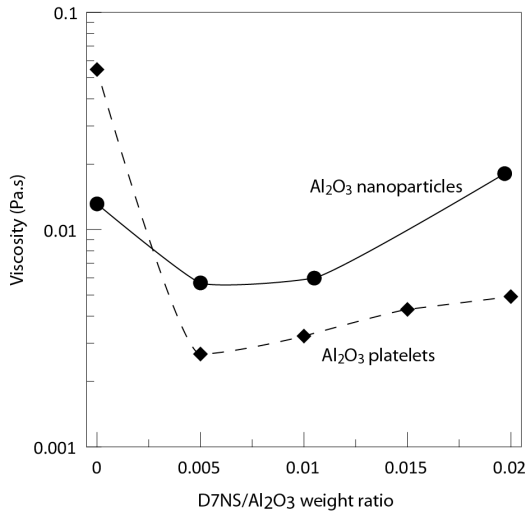

Figure 2.10: Viscosity at $150\,s^{-1}$ with different amount of $D[Na^+]$ of alumina platelets and nanoparticles suspensions (14 vol.% and 20 vol.% respectively)

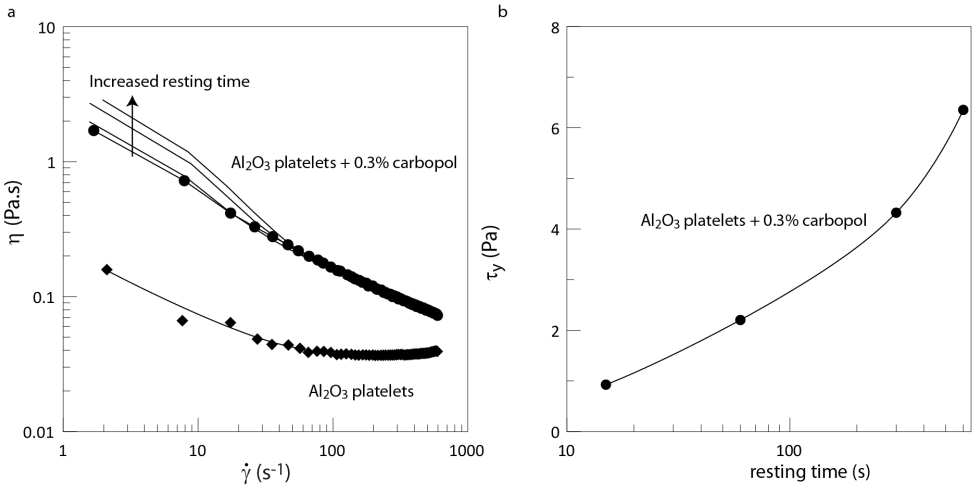

Figure 2.11: a) Effect of the addition of PAA on the suspension viscosity versus the shear rate at different resting time. b) Evolution of the yield stress versus the resting time.

2.3.3 Formation of a soft gel

Different strategies can be used to tackle, or at least minimize, the deleterious effect of the settling of the particle in those suspensions. The easiest one could be to increase the viscosity of the medium, by adding an excess of binder for instance. If the viscosity is increased, the settling velocity (2.3) is reduced but also the platelets' mobility, which can dramatically limit their ability to align. The ideal solution is to introduce a yield stress in the medium, where below a certain stress the suspension behaves like a gel and above it, like a liquid. Highly cross-linked polyacrylic acid (PAA) dissolved in water introduces precisely this type of behavior. This polymer forms soft aggregates in water [126, 127] that interact with each other and quickly (seconds to minutes) form a gel without external solicitation. This flocculation is reversed when a small stress is applied and the suspension viscosity is not affected too much by the presence of those polymers. The effect of the addition of PAA on the rheology of the alumina platelets suspension was measured and the results are plotted in figure 2.11. Before the measurement, a pre-shear was applied (at $100\,s^{-1}$ during 30 s) to remove all the possible aggregates and then the suspensions were left for rest during a varying amount of time. The initial viscosity of the suspension with PAA was at least an order of magnitude above the one without, and then rapidly decreased to finally be only twice as high. The addition of PAA increases the viscosity

and all the suspensions present a shear thinning behavior. The shear stress (τ) as a function of the shear rate ($\dot{\gamma}$) can be modeled by a Bingham expression:

$$\tau = \tau_y + K\dot{\gamma}^n \tag{2.5}$$

where τ_y is the yield stress, K the consistency and n an exponent that is < 1 in case of shear thinning and > 1 in case of shear thickening. As seen in figure 2.11a, when the suspension is allowed to rest for an increasing amount of time, the initial viscosity seems to increase while the viscosity remains the same over the rest of the applied shear rate. The evolution of the yield stress τ_y versus the resting time is plotted in figure 2.11b. The yield stress is multiplied by 6 over a resting time of 10 minutes, which reveals an evolution of the suspension.

The PAA seems to form a microgel quickly because the initial viscosity is relatively high but this gel is reinforced over time. This effect may influence the particles behavior in those suspensions. The presence of a yield stress is normally considered as sufficient to block the settling and as long as the particles do not induce a sufficient stress, the suspension is stable.

For comparison purpose, another settling velocity can be calculated with (2.3) with the viscosity of solution of PAA in water at the same concentration (given as 7 Pa.s for a 0.3 wt. % PAA solution) instead of the water viscosity (1,8 mPa.s at 298K). The resulting settling velocity is 1.4×10^{-8} m/s and leads to a settling time of approximately two days in the same conditions as above.

2.3.4 Conclusions

The use of a conventional dispersant for alumina allows to tweak the surface charge sign and value of both alumina platelets and nanoparticles. At natural pH (between 8 and 8.5), both the alumina and liquid phase precursors (silica and calcium carbonate) present a negative surface charge, which is a necessary condition to obtain repulsion between all the different materials and thus stable and homogeneous suspensions. The amount of dispersant was also optimized by rheological measurements. Finally, thanks to the addition of a rheology-modifier polymer, the dispersed suspensions present a yield stress sufficient to avoid the settling of the particles during the entire duration of the process.

Chapter 3

How platelets get aligned

3.1 Introduction

Before putting the alignment of platelets to good use, this chapter tries to explain how platelets can get aligned by the growth of ice crystals. The first thing to investigate was whether platelets could be aligned by ice templating or not? If anisotropic particles get aligned, is the lateral growth of ice crystal responsible (see figure 3.1) or it is something else? Preliminary experiments were done to understand how the initial conditions can influence this organization. A discrete element model was then built, improved, and fed with the experiments carried out in parallel. Only this back-and-forth movement could have created at the same time this complete model and (more importantly) all the materials described in the rest of this manuscript. Even if, in a clarity purpose, this chapter is dissociated from the others, it is intimately linked with them because no other technique could have given us this direct insight into this self-assembly phenomenon. The section 3.3 of this chapter have been submitted as an article.

3.2 Preliminary results

These experiments were carried out to determine first, if platelets can be aligned by ice templating- and then- (since the preliminary results were successful) what degree of control can be achieved upon this alignment. The first samples were made with a suspension of 16 µm diameter boron nitride platelets, frozen at a low cooling rate (-1°C/min). To align the particles, our first hypothesis was that they have to be small enough to be pushed by the crystal, but large enough to interact with

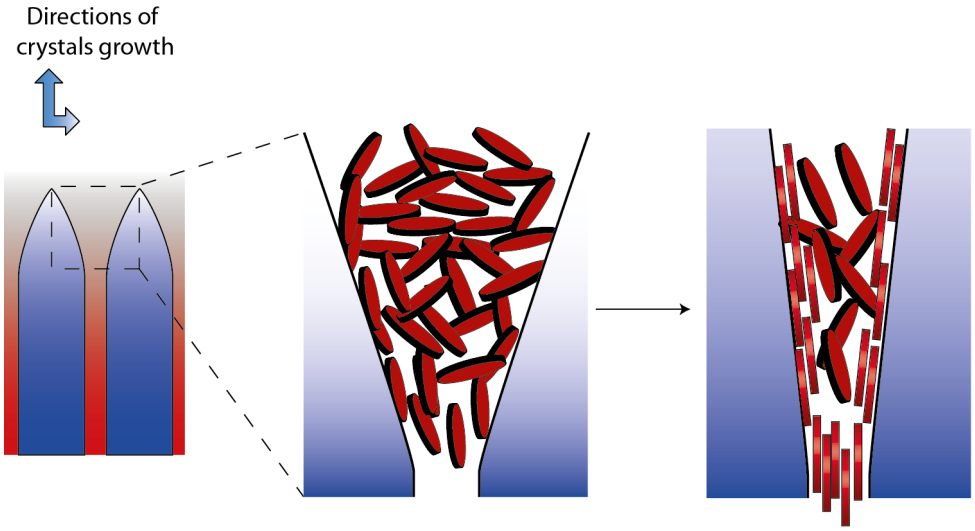

Figure 3.1: Schematic representation of the expected platelet alignment mechanism.

the solidification front. Consequently the particle size was chosen to be on the order of magnitude of the inter-crystalline space at this low cooling rate (around ten micrometers). The platelets were correctly aligned (see figure 3.2) and apparently so throughout the sample. When a higher cooling rate was used (-10°C/min), the platelets were randomly oriented and distributed, a sign that the critical velocity has been reached.

Two different powder granulometries, with average particle size of 8 µm and 1 µm, were processed in the exact same conditions as previously. The resulting cross sections are represented in figure 3.3. The platelets organization differs from the large one, they tend to be more aligned and closely packed in the outer part of the lamellae than in the core. This effect is even more visible with the 1 µm particles (see figure 3.3). Those preliminary results provide a first assumption, there is a finite number of particles that can be aligned in the wall, i.e. there is a particle-to-lamellae size ratio to obtain the best alignment. Based on this assumption, we have started to explore, both experimentally and *in silico*, the domain of the number of particles aligned with respect to the freezing conditions, as well as to quantify this stacking. The results obtained are presented in the next section.

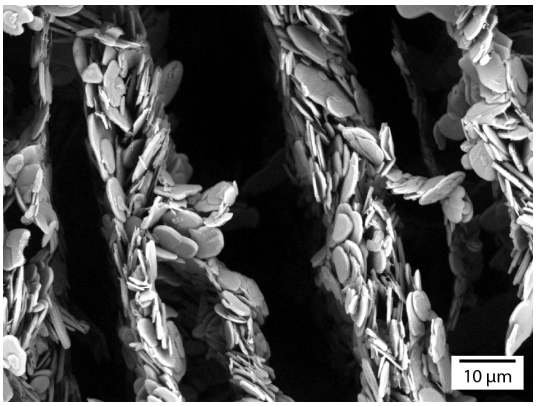

Figure 3.2: Cross section of ice templated samples comprising 19 vol.% of 16 µm boron nitride platelets frozen at -1°C/min.

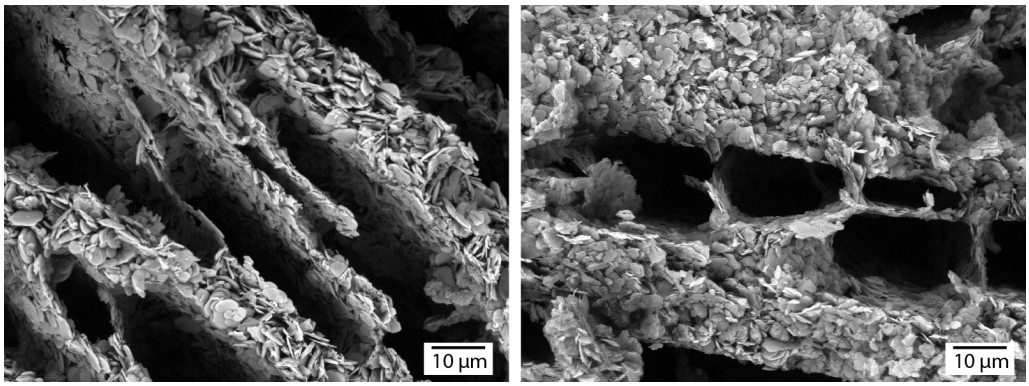

Figure 3.3: Cross section of an ice templated sample comprising 19 vol.% of 8 µm (left) and 1 µm (right) boron nitride platelets frozen at -1°C/min.

3.3 Self-assembly of facetted particles driven by ice growth

3.3.1 Introduction

The controlled alignment of facetted or anisotropic particles holds the promise of a new class of crystalline materials at all length scales, exhibiting appealing structural and functional properties [128]. Understanding and controlling how such particles organize is required for the optimization of functional properties. Superlattices, for instance, with translational and rotational order of the building blocks, are currently investigated for their optical and electrical properties or for plasmonic applications [129].

Most of the approaches developed so far are based on the evaporation of a solvent [82, 130] or the sedimentation of particles [22]; ordering in these phenomena is ultimately controlled by the pressure applied to a dense particles assembly, the particle interactions [21] and the rate at which the particle concentration increases. Reaching an optimal packing thus requires a fine control over the particle shape, polydispersity, self-assembly driving force, and particle interactions, which restrict the applicability of the approaches to specific systems.

For larger particles, the diffusion is limited and therefore so is their capacity to form dense structure upon concentration with conventional method. Sequential deposition methods [50, 131, 132] are able to order anisotropic particles, although such methods are limited to thin samples and work only with high aspect ratio particles because the alignment results from shear forces acting on the particles.

Anisotropic structural or functional properties could thus emerge from an assembly of anisotropic building blocks with an approximate alignment. Yet, very few approaches are able to provide such alignment in bulk materials and within reasonable time scale. The growth of ice crystals in a colloidal suspension can be used to drive the self-assembly of anisotropic building blocks [133, 134, 135].Several benefits are associated with ice growth in this case, such as the possibility to obtain bulk materials or a reduced processing time of the order or minutes -vs. hours or days for evaporation or sedimentation processes [22]. In addition, the process is in principle almost independent of the nature of the materials used [100].

Although alignment has been demonstrated experimentally, the underlying phenomena have not been deeply investigated so far. Several mechanisms have been hypothesized [133, 135], and numerous important questions must be addressed. What is the driving force for the self-assembly? How do particles organize? How should the freezing conditions be adjusted to optimize the structural organization of the

particles? How much do particle-particle interactions matter? The answers to these questions are essential for a proper control of the phenomenon and the resulting functional properties of the materials.

We demonstrate here how the ice growth induced self-assembly of facetted particles can be accurately described and understood by a combination of discrete element modeling and observation of the experimental spatial distribution using high resolution X-ray computed holotomography. These tools are used to explore the self-assembly behavior and predict the evolution of such colloidal system. The benefits of the resulting structures are illustrated with the thermal properties of Boron Nitride (BN)/silicon rubber composites. The methodology developed here is then extended to predict the self-assembly of cubic particles.

3.3.2 Experimental section

Materials processing

Suspensions were prepared by mixing distilled water, a cellulose ether (Tylose H4000P2, Shin Etsu, at a weight ratio Tylose on BN powder of 0.5%) an organic binder (Poly Ethylene Glycol 4M, Sigma Aldrich, 2 wt.% of dried powder mass) and the BN powder (TRES BN PUHP 3008, Saint-Gobain BN products) at different volume fractions. The powder used in the study present platelet morphology with a diameter around 8 μm and 1 μm in thickness. After a first mixing step with a propeller stirrer, ultra sonic mixing was conducted with a sonotrode (Digital Sonifier 250) with an applied energy around 150 Wh/kg.

Freezing of the slurries was done by pouring them into a silicone mold (diameter 20 mm, 21 mm height) placed on a cooled copper plate. The copper plate was cooled by silicone oil at a temperature regulated by a cryothermostat. The cooling rate were adjusted between 0.5°C/min and 2°C/min. Faster cooling rate were obtain by dipping a copper finger with the mold on top in liquid nitrogen. Measurement of ice front velocity was made by dipping a ruler at different times in the slurry and measuring the height of frozen sample. Once freezing was completed, the samples are freeze-dried for at least 48 hrs in a commercial freeze-dryer (Free Zone 2.5 Plus, Labconco, Kansas City, Missouri, USA), to ensure a complete removal of the ice crystals.

Holotomography

Holo-tomography experiments were carried out at European Synchrotron Facility at the beam line ID-22. More details on this technique can be found elsewhere [136]. To enhance phase contrast, porous sample were infiltrated by silicone rubber under

vacuum prior to observation. Segmentation and density measurements were made using the software Fiji [137].

Thermal diffusivities measurement

A flash lamp method was used to measure the thermal diffusivity of the BN/Silicone rubber composite. Disk samples of 20 mm diameter and 5 mm thick were put in a holder, a flash produced by a lamp heated a side of the sample and the temperature profile was recorded on the other side. The thermal diffusivity was obtained by a fit of this profile by the quadripole method [138]. At least five different measurements were made on each sample.

Percolation threshold measurement

The percolation threshold of platelet particles can be estimated from an empirical formula developed for permeability clay composite [139, 140]:

$$\Phi_p = \frac{2}{3S+1}\frac{W}{L}p_c \tag{3.1}$$

With W and L the thickness and length of the platelet respectively, $p_c = 0.718$ and S the order parameter of platelet orientation given by the following relationship:

$$S = \frac{3 < cos^2\theta > -1}{2} \tag{3.2}$$

Where $< cos\theta >$ is the mean of the platelet angles with respect to the preferred direction (equal to 54°for random orientation).

Discrete elements modeling

Discrete Elements Modeling: Discrete element modeling was carried out by a custom version of the LAMMPS Package. To reproduce the lamellar structure characteristic of ice crystal growth, a rectangular simulation box was created. The method used to produce platelet-like particles using spherical ones consist in the creation of a cylindrical region in the simulation box. The region was then filled with spheres with a diameter corresponding to the thickness of the particle, here 1 µm. During the simulation, the sphere were fixed together as a rigid body, the software just sums the interaction on all the spheres to calculated the resulting displacement and torque applied to the assembly. To introduce the polydispersity of particle size, a random number from a Gaussian statistical distribution was used to adjust the radius of

each cylindrical region. The distribution was centered on 4 µm with standard deviation of 1 µm. To avoid any overlap of the region that could lead to truncated particles, they were created successively at different x coordinate, while the z and y coordinates was randomly selected. The simulation box dimensions were first set to 300 x 200 x 200 μm^3, thus a dilute system was obtain. The box sizes were then shrunk to dimensions of 100 x 50 x 50 μm^3. The number of particles was calculated to obtain the desired volume fraction, knowing the density of BN (2.26 g/cm^3) and mean particles volume.

To replicate the growth of ice crystals, two opposite walls were moved at a given speed, the speed of the ice front velocity measured experimentally. The simulation box was constraint to remain small in the two directions z and y which allows us to neglect the curvature of ice crystals tips; they were therefore fixed at 50 µm. The y direction was thus extended to 100 µm to model enough particles to have statistical information. The other walls were maintained fix during the whole simulation, at a distance corresponding to particle radius, to allow the rotation of the particle placed in the box boundaries. Software limitations do not allow a periodic condition with rigid body assemblies. Considering the low surface charge of BN particles in water [110] and the large size of the particles, only the repulsive part of the Lenard-Jones potential was used to model particle interaction:

$$V(r) = \epsilon_0 \left(\frac{\sigma}{r}\right)^{12} \tag{3.3}$$

Where $\sigma = 1\mu m$ is the particle diameter, r the distance between two particles and ϵ_0 the Hamaker constant of the BN / water / BN interfaces. This potential, because it is only repulsive, creates an excluded volume to avoid unphysical particle overlaps, while simultaneously saving CPU time. The particle / ice front interaction is represented by a Van der Walls potential for a sphere and a plane near contact [141]:

$$W(h) = -\frac{AR}{6h} \tag{3.4}$$

Where $R = \sigma/2$ corresponds to the particle radius, A the Hamaker constant of particle / water / ice interaction and h the distance between the ice front and the particle. The non retarded lifshitz theory was used to calculate the different Hamaker constants with the refractive index and dielectric constant of each material (hexagonal BN, water and ice). The input values for simulation were $H = 4 \times 10^{-20} J$ and $A = -3 \times 10^{-21} J$. The negative value of the Hamaker constant for ice / particle interaction indicates repulsion, characteristic of many solidification front [142, 143, 144].

The simulations were carried out in an NVT ensemble with the temperature regulated by a Langevin thermostat. The Langevin thermostat allowed the addition of a viscous force characteristic of the solvent interaction, which is intimately linked to the repulsion / engulfment phenomenon. The repulsive interaction between the ice front and the particle lead to a disjoining pressure thus to the appearance of a thin liquid film at the interface. If the particle comes closer to the front, there is a chance of being encapsulated in the ice. No existing model grasps the complexity of the repulsion / engulfment equilibrium in concentrated colloids and a simplified one introduced by Barr et al. [145] has been used here. It is based on the balance between drag and repulsive forces. The repulsive forces come from the interactions with the ice front and the drag forces from solvent interaction. The maximum drag force attained at the encapsulation can be calculated via Stokes's law:

$$F^d_{max} = 6\pi\nu R v_c \tag{3.5}$$

Where ν is the viscosity of water (1.8 mPa.s at 0°c), R the particle radius and vc the critical velocity (determined experimentally at 35 µm/s for BN particle). The critical distance δ before encapsulation can thus be deduced by equaling $W(\delta) = F^d_{max}$. The construction of the anisotropic particles introduced here let us apply all the interaction and forces on each individual sphere without any assumption on the whole particle.

For visualization and image analysis purpose, the center, radius and normal vector of each particle was extracted and a plugin for Fiji was developed to visually reconstruct the particles from the knowledge of their geometry. The time-lapse density measurements were made by the use of a programmed plugin and the percolation region by the existing 'Find connected region' plugin with Fiji. The image and movie presented here have been made with the software Paraview.

3.3.3 Results and discussion

Ice growth induced self-assembly of anisotropic, facetted particles

The self-assembly of facetted particles during ice-templating occurs at length scale of tens of microns. The resulting spatial distribution is intimately linked to dynamical interactions between the particles and the growing crystals but also to viscous interaction with the unsolidified solvent. The imaging possibility offered now by synchrotron radiation facilities [146] allows the visualization of the growth of large crystals in real time [147] but the spatial resolution is still not sufficient to image in situ the dynamic arrangement of particles. After freezing and ice removal however, the resulting samples can be imaged at a resolution good enough to distinguish

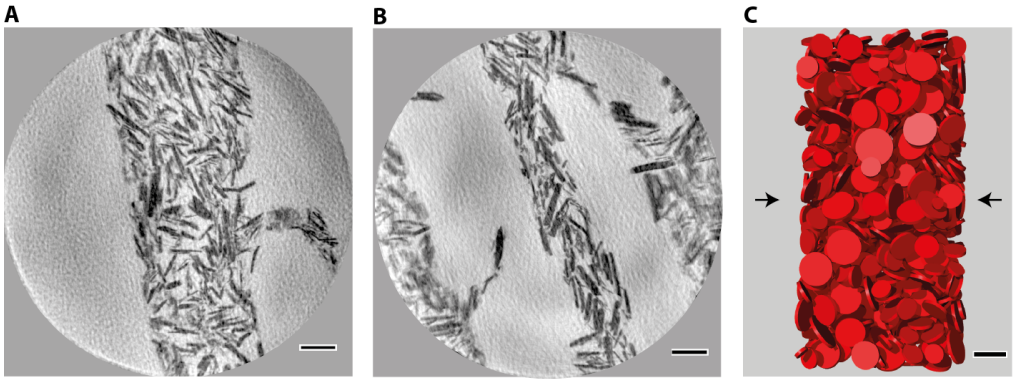

Figure 3.4: **Comparison between the modeling initial state with 700 platelets and the holotomography reconstruction of ice templated samples.** a) and b) Cross-sections perpendicular to the wall direction of holotomography reconstructions. Structures obtained with the slow freezing rate (15 μm/s) a) and the fast cooling rate (25 μm/s) b), resulting respectively in the thickest and the thinnest wall. The two types of structure are visible, with a better alignment of particles in the outer regions than in the core for a) and the homogenous orientation of the particles in b). c) Initial state of the modeled system, representing the random orientation and polydispersity of the particles size before compaction. The black arrows indicate the direction of the moving interface. Scale bars: 10 μm.

the particles. In the present paper, we have used high resolution KB focused X-Ray holotomography at the ID22NI beam line at the ESRF.

Microstructures of ice-templated BN platelets infiltrated by a silicon rubber are shown in figure 3.4. The 50 nm resolution of the holotomography is sufficient to discern the platelets arrangement in the wall. In figure 3.4A, the slow solidification interface velocity (close to 7 μm/s) leads to thick walls (30 μm) and the particles that are directly in contact with the growing ice are well aligned, parallel to it. Oppositely, in the inner region of the wall the particles are less ordered. This type of structure will be referred to as the sandwich structure. When the solidification interface is moving faster, a faster solidification interface velocity is applied (close to 25 μm/s), the wall obtained is significantly thinner (15 μm, figure 3.4b) and the packing and alignment of particles is improved. This type of structure will be referred to as the compact structure. The initial state of the modeled particles is depicted in figure 3.4c and shows the Gaussian size distribution of the particles, their random orientation, as well as the width of the model box (e.g. 50 μm). These dimensions

match the actual experimental conditions. This model uses comprises up to 800 particles (thus roundclose to 42 000 individual spheres) in a volume of 100 x 50 x 50 μm^3. The simulated volume is willingly limited to those dimensions, to reflect closely the actual experimental conditions (figure 3.4) and to neglect the curvature of the ice crystals in the freezing direction. Because crystal nucleation (and therefore branching) cannot be taken into account in this type of model, the lateral dimension has been extended just enough to have a representative number of particles in a reasonable simulation time.

The benefits of self-assembly of large particles in bulk materials are demonstrated here with the thermal properties of the BN/silicon rubber composite shown in Figure 1. Controlling the orientation of BN particles to take advantage of their anisotropic thermal conductivity could be highly beneficial in thermal management applications, where the heat needs to be taken away from the components in the most efficient manner. BN is a prime choice for ceramic materials that are used in thermal management systems. The crystalline anisotropy of BN can be used to obtain platelet-like particles which exhibit orthotropic thermal properties [148] that are 20 times lower in the c-axis (30 W/m/K) direction than in the perpendicular plane (600 W/m/K).

Here we took advantage of the ice growth induced self-assembly to obtain bulk, macroporous materials where the anisotropic particles are aligned along the freezing direction. The samples were then infiltrated with a silicon rubber before their thermal properties were assessed. For the sake of comparison, a homogeneous composite was obtained by simply mixing the same amount of particles in the silicon rubber. The corresponding microstructures are shown in figure 3.5, along with the results of the thermal diffusivities measurements (figure 3.5b). The material with the controlled architecture presents a thermal diffusivity almost three times greater than the homogeneous composite, illustrating the benefits of an aligned structure, even if the alignment is not completely perfect.

Alternative strategies based on the application of an electric [45] or magnetic [39] field have been proposed to align BN particles to improve the thermal properties. The relative improvement in thermal properties (figure 3.5c), estimated using the difference of the thermal properties in the random and aligned structures normalized by the thermal properties of the random structure, provides a comparison of the efficiency of these strategies. Ice templating is comparatively much more efficient. On top of that, it is also able to align particles in much more concentrated suspensions (almost 20 vol.%, compared to less than 5 vol.% for the other methods).

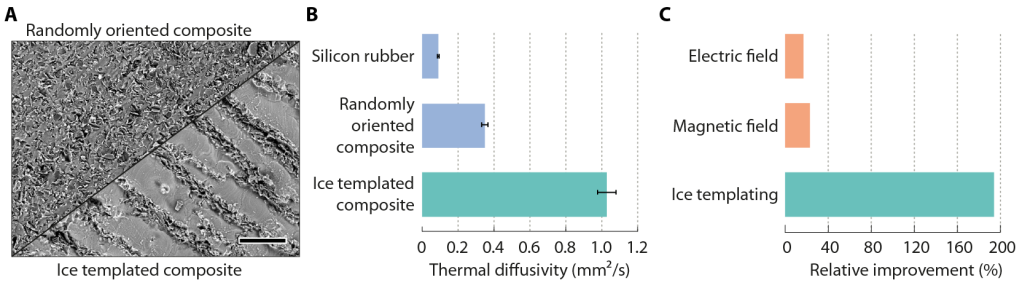

Figure 3.5: **Improvement in thermal properties resulting from the control of the orientation of anisotropic particles.** a) Microstructure obtained for both randomly oriented (upper left) and ice templated Boron Nitride/silicon rubber composite (lower right). Scale bar: 100 µm. b) Comparison of the thermal diffusivity of the two composites and the silicon rubber. c) Comparison of the relative improvements in thermal properties due to the alignment of BN particles induced by an electric field [45], a magnetic field [39], or ice templating (this study).

Predictions of particle packing

The driving force for ice growth induced self-assembly of large (> 1 µm) particles is not random thermal motion. The potential energy needed to lift the particles (of 8 µm diameter and 0.5 µm thick) from its own diameter in water can be estimated by the following relationship:

$$U_g = m \cdot g \cdot \Delta h = \pi R^2 e(\rho_{BN} - \rho_w) \cdot g \cdot 2r = 2.6 \times 10^{-18} J \tag{3.6}$$

where m is the weight of the particle, r its diameter, e its thickness, and ρ_{BN} and ρ_w the density of BN and water respectively. This energy is thus around three orders of magnitude superior to the energy brought by the thermal motion (of the order of $k_B T$, so $3.8 \times 10^{-21} J$ at 273K). This means that the behavior in water of particles of this size will not be controlled by thermal energy.

The common modeling approaches (e.g. Monte Carlo [149]) thus cannot accurately describe the behavior of the system. In particular, the particle encapsulation by the interface [142], a key feature of the phenomenon, cannot be taken into account. Discrete element modeling (DEM) is able to take into consideration several crucial aspects of the phenomena, such as the viscosity of the suspension, the interactions between particles (modeled here by a Van der Walls and Lenard-Jones pair potential for the ice and inter particles interactions respectively), and the continuous particle size distribution. The key feature implemented is the possible engulfment

of particles by the moving solidification interface. Many different analytical models have been developed to predict this complex phenomenon [150, 151, 152, 143, 153], but are only valid for single, isolated particles. By using DEM, a simple force equilibrium between repulsion and drag forces can be introduced and thus take the dynamical and collective aspects (e.g. shock between particles) of this phenomena into account. It also provides access to the dynamics (time-lapse position and orientation) of particle redistribution by the growing ice crystals, which is nearly impossible to obtain experimentally.

Particular attention must be paid to the particle shape and interactions. Different pair potentials can be used for anisotropic, facetted particles. These anisotropic potentials have been developed for clay suspension, such as the Gay-Berne [154, 155] potential, based on Lenard-Jones potential and a quadripole orientation. The RE-squared [156] potential, based on an assembly of small isotropic Lenard-Jones potential has also been used. Even if those potentials allow a lot of the complexity involved in anisotropic particles interaction to be taken into account, they are limited to model systems with monomodal particles and therefore, cannot accurately describe the interactions with planar interface such as the solidification front here. A different strategy has been developed here. Spheres (with an associated Lennard-Jones potential) are fixed together as cylindrical rigid bodies. The radius of those cylinders follows a Gaussian distribution to represent the polydispersity of platelet size. During the simulation, the software sums the interactions on all the spheres to calculate the resulting displacement and torque applied to the assembly. The simulated engulfment phenomenon can thus take place locally, at the scale of the constitutive spheres instead of the whole platelet and thus is closer to the reality. The comparison of the modeling and experimental results in terms of structures, particle density packing and distribution of orientations are shown in figure 3.6. The predicted compact structures (figure 3.6b) are comparable to the experimental one (figure 3.6a), with highly oriented particles in a thin wall. The same conclusion can be drawn for the sandwich structures (figure 3.6e and 3.6f), where the particles present a better alignment on the outer region of the wall than in the inner region. The use of reduced coordinates where the thickness of the wall is normalized by the periodicity λ of the structure (structural wavelength [89]) allows the proper comparison between the experimental and predicted results.

The experimental and predicted particles packing (figure 3.6c) are very similar: the density reaches a maximum value of 0.45 (0.41 for the experimental one) in the inner region of the wall. The high aspect ratio and the particle size distribution lower the packing density, compared to that of random close packing of monodispersed spheres (known to be about 0.64). For the sandwich structure, the evolution

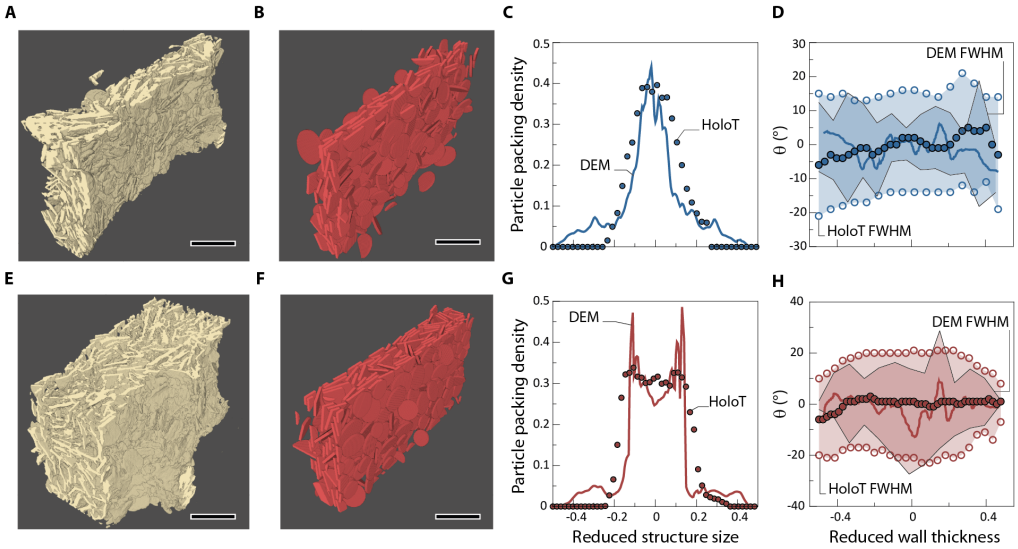

Figure 3.6: **Comparison and characteristics of particle packing of the two types of architectures in the tomography reconstruction and the model.** a-d) Compact structure and e-h) sandwich structure. a) and b), respectively e) and f) represent a 3D-view of the structures, as seen by holotomography (left) and DEM (right). c) and g) Packing density vs. reduced structure size. A continuous evolution of density is observed in the compact structure, while the density drops in the inner region in the sandwich structure. d) and h) Distribution of particles orientation for both structures vs. reduced wall thickness. The darker color indicates where the modeled and the experimental distributions overlap. Scale bar: 20 μm.

of the experimental and predicted density is again similar (figure 3.6g). The density appears higher in the border and reaches a value of 0.45, similar to the compact structure while the density in the inner region falls to 0.25 (0.35 and 0.29 respectively for the actual structure). Both structures present approximately the same overall density (0.32). The dispersion of particle orientations with respect to the wall direction is plotted in figure 3.6d and figure 3.6H, represented by their mean orientation and the full width at half maximum (FHWM) of their cumulative distribution. In the compact structure (figure 3.6d), the mean orientation corresponds to that of the wall (mean angle of 0°), for both the model and the experiment. The concentration of the particle during the freezing does not induce any tilt of the particles. The FWHM is constant in the wall, and the value is slightly smaller in the model (10°) than in the experiment (15°). The particles are slightly more aligned in the model than in the experiment and therefore the density and alignment are also slightly overestimated. In the sandwich structure (figure 3.6h), the FWHM varies from 10°in the outer region to 20°in the inner region, revealing the misalignment of the particles in the inner region.

We can now analyze through a parametric study the resulting structure as a function of the experimental conditions. The predicted phase diagram is shown in figure 3.7. This diagram is calculated using simulation, as a function of particle size and interface velocity, the two main experimental parameters that can be adjusted to control the resulting microstructure. The encapsulation situation corresponds to the situation where the fraction of encapsulated particles is above 30%. The selection of this threshold of particle fraction as a criterion for encapsulation was made by looking at the fraction of engulfed particles at the critical velocities determined experimentally. Those structures are obtained at the same ice front velocity (above 40 μm/s) for the entire set of initial particle fractions (which confirmed this value as an intrinsic property of the particles) except for the highest solid loading (0.22). At this point the concentration is close to the percolation threshold (estimated at 0.215, see Experimental section and references [139, 140] for more details). The transition between sandwich and compact structures occurs at a higher ice front velocity as the solid loading increases. The final densities are also represented in figure 3.7 as an isodensity contour map. As described previously, the architecture of the wall reflects the particle orientation and thus the packing density. Area of high density corresponds to the compact structure. This phase diagram can be used as a predictive tool to adjust the properties of the final material, by predicting the density and structure of the particle packing as a function of the experimental conditions.

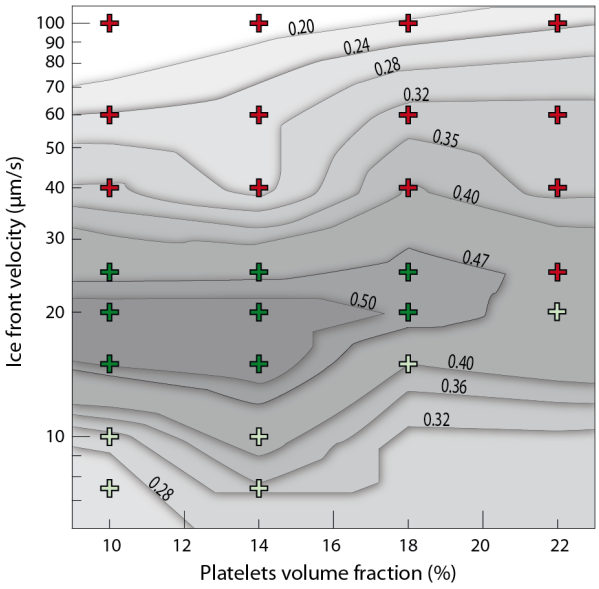

Figure 3.7: **Phase diagram of the possible anisotropic particle assemblies.** Light green cross symbol for sandwich structure, dark green cross symbol for compact structure, and red cross symbolfor engulfed structure (where more than 30% of particles are trapped in the ice). The background represents a map of the wall density predicted by DEM, each tone representing an isodensity region.

Dynamics: self-assembly principle

Because the structures obtained after freezing are the result of the redistribution and concentration of particles by a solidification front, the observed differences arise from different interactions that take place in this peculiar system. In a first approximation, the process can be considered as equivalent to a simple powder compaction by two moving fronts. Nevertheless, particles can be encapsulated by the moving front, depending of the conditions (viscosity, velocity, existence of premelted films). The dynamic behavior of the system can be investigated by DEM (Figure 3.8).

The time-lapse snapshots of the DEM results (figure 3.8ato 3.8e) and the corresponding density profiles (figure 3.8h) illustrate how the alignment is initiated in the outer region and then progressively propagates towards the inner region. Particles with the same color belong to the same percolating network. The evolution of the system follows three stages (figure 3.8g). Because the interface moves slowly, very few or no particle are engulfed during the first moments of growth (stage 1), they are just locally aligned and densely packed (figure 3.8aand figure 3.8b). Some are then engulfed (figure 3.8c) as the interface keeps moving. The layer of aligned particles is still pushed and the concentration of particles in the inner region of the system starts to increase (figure 3.8h). Percolating networks grow rapidly (stage 2). It starts to act against the displacement and rotation of particles. The pressure exerted by the moving interface is eventually not strong enough to overcome the counter pressure exerted by the percolating network of particles (stage 3); the system is ultimately jammed in a configuration where particles are aligned in the outer region and in the inner region (compact structure) or not (sandwich structure).

The evolution of the fraction of particles encapsulated in the ice is plotted in figure 3.8F, for two initial concentrations (10 vol.% and 18 vol.%) and three different ice front velocities (15, 25 and 40 μm/s). For the 18 vol.% system, the density evolutions present similar trajectories at three different velocities (15, 25 and 40 μm/s), even if the final densities differ. The evolution is similar in a more dilute system (10 vol.%). An increase of either the volume fraction of particles or the interface velocity results in more encapsulation of particles by the moving interface.

Percolation arguments are not enough to predict the type of structure obtained. In both types of structure, complete percolation is obtained at approximately the same position of the moving interfaces (figure 3.8g). Further local ordering of the particles is still possible after reaching complete percolation, as illustrated in figure 3.8a to 3.8e (white arrows).

For large particles like the ones used here, the critical factor controlling the evolution of the system and the type of packing obtained is thus the encapsulation of the particles by the moving interface. With the same initial volume fraction of parti-

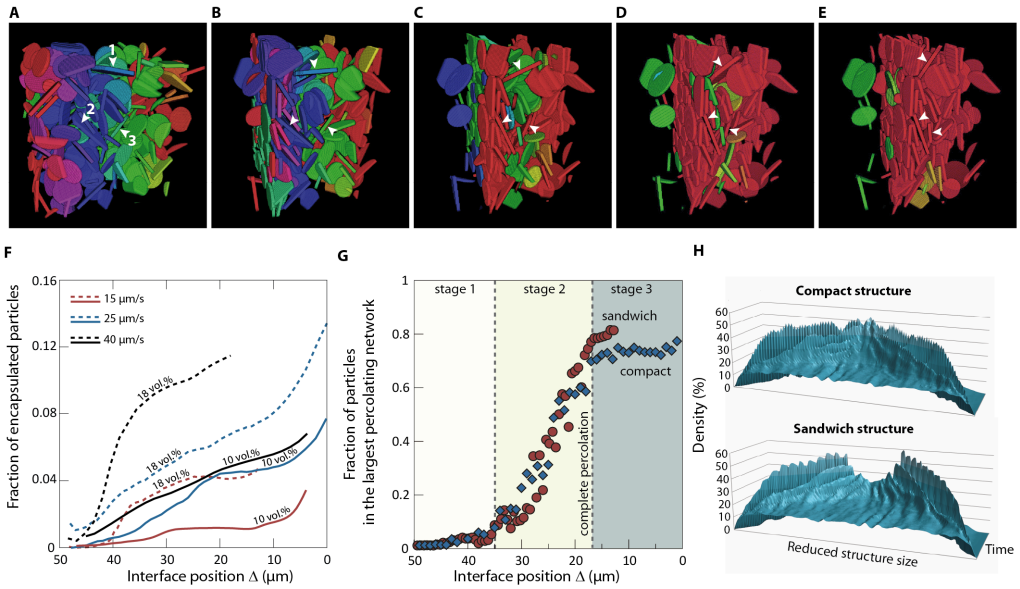

Figure 3.8: **Dynamic evolution of particle organization and packing density.** a-e) Snapshots of the time-lapse evolution that illustrate the progressive alignment of the particles as the interface progresses. The color code correspond to the percolation of particles: particles having the same colors belong to the same percolating network. f) Dynamical evolution of the fraction of encapsulated particles during the freezing for two different volume fraction: 10 and 18 vol.% and three different interface velocities. g) Evolution of the fraction of particles that belongs to the largest percolating network as a function of the interface position Δ, for the compact and sandwich structures. A complete percolation is obtained around 17 µm for both types of structure, although further local alignment of the particles occurs, as can be observed in a-e). The fraction is not reaching a value of 1 as some particles are engulfed in the early stages of interface movement. h) Time-lapse evolution of the density profile through the wall thickness, for both types of structure.

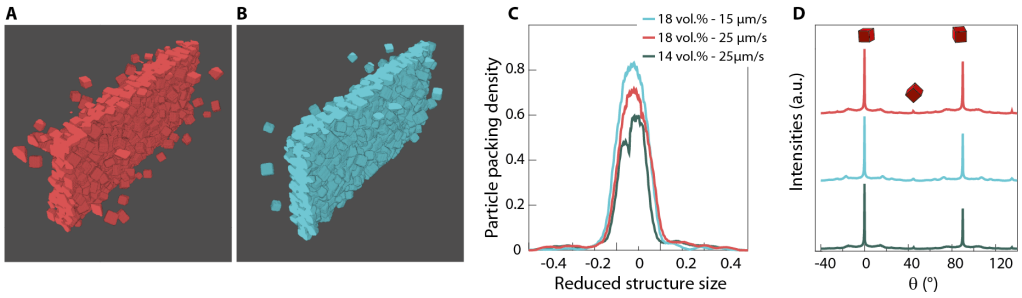

Figure 3.9: **Ice growth induced self-assembly of cubic particles.** a) and b) Final architectures predicted by DEM for 25 µm/s a) and 15 µm/s b) ice front velocity, at the same solid loading (18 vol.%). Denser packing's are obtained for the slowest front velocity. c) Particle packing density for different concentrations (14 and 18 vol.%) and interface velocities (15 and 25 µm/s). sd) Orientation of the resulting architecture (see text for details) showing the alignment of the cubes along the wall direction (0°and 90°).

cles, an increase in interface velocity results in an increase of particle encapsulation. As a result, the concentration of the solid phase between the moving interfaces is lower. Particles have more freedom to reorient before the interface eventually encapsulates everything, leading to the compact structure. If all of them are repelled by the moving interface, the concentration is too high when the particle networks start to percolate. Particles do not have enough time to rearrange before total encapsulation, leading to the sandwich structure.

Self-assembly of cubic particles

Being able to orient platelet-like particles in porous or bulk materials is highly valuable, in particular for structural materials but also piezoelectric or thermal management materials. However the self-assembly induced by ice-templating is not limited to this specific particle shape and might be extended to any type of facetted particle. To illustrate the fact that facetted particles can self-assemble even if they have an isotropic aspect ratio, the self-assembly of cubic particles has been explored with our simulation tool. Three different conditions (figure 3.9) have been simulated, to predict the effect of the ice front velocity and the initial volume fraction. The obtained morphologies at two different ice front velocities are presented in figure 3.9a and 3.9b. Only one type of organization is obtained with all the simulation conditions: after solidification, all the cubes are well aligned in the wall's direction. This

is confirmed by the density profile in figure 3.9c, where the maximum density is at the center of the wall. However, this value changes with the applied conditions. The higher the initial density and the slower the compaction rate, the higher the final density. The packing density can reach a value as high as 0.80, slightly higher than the theoretical random packing of cubes found in the literature (0.74 for reference [157], 0.78 for reference [158], both using different model type). The nearly perfect stacking in one direction (the direction of the wall thickness) can explain this slight discrepancy. The alignment of cubes is similar in all the conditions tested and the image analysis revealed nearly only the edges of the cube at 0°and 90°. The cubes are then nearly all perfectly stacked in the thickness of the wall. Those three conditions reveal the potential of this model to easily determine the best conditions to obtain dense packing of cubic particles or any others shaped particles of interest.

3.4 Conclusions

Using the growth of ice crystals as a driving force for the self-assembly of large, facetted particles is an appealing alternative to the current evaporation or sedimentation strategies.

A key conclusion of this work is that a high aspect ratio is not required for ice growth induced self-assembly, as shown here and in contrast to the sequential deposition methods. The steric interaction between the moving interface and the particle is highly localized; working with facetted particles is therefore the only requirement (in terms of morphology) to obtain alignment. The methodology developed here can easily be generalized to other systems, in particular by taking into account different models of interaction potentials for smaller particles where gravity is not the controlling parameter.

Although the particle alignment is not perfect, in comparison to superlattices obtained by sedimentation for instance, the benefits on the functional properties have been demonstrated here for thermal properties. The possibility to align particles in the bulk (centimeter sized samples) and in short times (minutes), holding the promise of novel crystalline materials with appealing functional properties, make it worth further research efforts.

Chapter 4

First level- Putting the alignment of particles to good use

4.1 Introduction

The growth of ice crystals effectively aligns platelet particles (or induces self-assembly). This chapter describes its application in two different ways. The first concerns the use of platelets alignment and organization to improve the functional (thermal) properties of polymer/ceramic composite materials. The second part details an unexpected benefit to the use of platelets, because they lead to structures that were up until now difficult to obtain: porous structure with large (some tens of μm), non-tilted pores and thin walls. This part has been submitted as an article.

4.2 Thermal properties of boron nitride composites

4.2.1 Introduction

This section investigates the effects of particles alignment by ice templating on the functional properties of materials (in the simplest configuration possible) and compares the results obtained with different alignment techniques. The study of thermal properties of boron nitride platelet composites is an example of the resulting improvements achieved by ice-templating compare to other techniques. The effect of different processes and / or composition modifications was also investigated.

To palliate the low thermal conductivity of polymers, ceramic particles are often added. Their thermal conductivities are an order of magnitude higher and they are electric insulators at room temperature. Boron nitride is a good candidate due to a

high thermal conductivity and a high energy band gap (around 5 eV). As mentioned previously (3.3.3), its crystalline structure is similar to graphite, highly anisotropic, and its properties reflect this anisotropy, with a conductivity twenty times higher in the direction perpendicular to the c-axis than parallel (respectively 600 W/m/K and 30 W/m/K)[148]. Tailoring boron nitride particles orientation could greatly improve the properties of the composites by aligning the platelets parallel to thermal gradient direction.

4.2.2 Thermal properties of composites by ice-templating

Different parameters of ice templating can be changed to influence the thermal properties of the composite. The cooling rate changes both the platelets organization and size of the structure wavelength[a]. However, the measurement of the thermal properties is not sensitive and accurate enough to measure the small changes introduced by the different architectures. The thermal diffusivities of several samples with the two types of architectures (see chapter 3.3.3) were measured and no significant deviations were observed compared to the experimental uncertainty (±10%). The values obtained with a randomly oriented and an ice templated composite, both with a BN content of 18 vol. %, are plotted in the figure 4.1. Details about the measurements can be found in section 3.3.2. The thermal diffusivity of the ice templated composites is around three times higher than the randomly oriented material.

Below a certain BN content (14 vol.% for 8 µm platelets), the composite's response changes. A thermogram of the typical response of a high and low BN content composite is plotted in figure 4.2a. The curve for a low content composite appears to be the sum of two contributions, probably the wall and the silicon rubber. Evolution of the diffusivity as a function of the volume fraction of boron nitride is presented in figure 4.2b. Below 14 vol% of boron nitride, the response of the composite is heterogeneous and above, a slight increase can be seen but it is too small to be considered significant.

The response of those materials can be modeled as a lamellar composite of pure silicon rubber and boron nitride / silicon rubber lamellae. They are close to the case considered for Voigt bound in the Voigt approach[159] and the diffusivity D_{comp} can be modeled as (if we neglect the coupling between the two components):

$$D_{\text{comp}} = \nu_{\text{matrix}} \cdot D_{\text{matrix}} + \nu_{\text{wall}} \cdot D_{\text{wall}} \tag{4.1}$$

Where ν_{matrix} and ν_{wall} are the volume fraction of each phase, D_{matrix} and D_{wall} the thermal diffusivities of the matrix and the walls respectively. The volume frac-

[a] the mean length of a pore plus a wall[89]

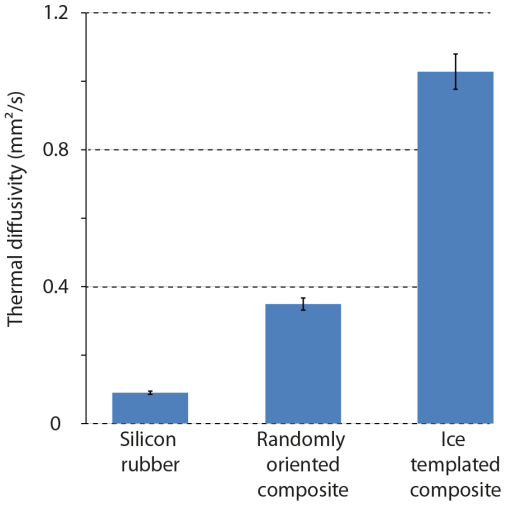

Figure 4.1: Thermal diffusivity of samples at 18 vol.% of boron nitride, prepared by simple mixing or by ice templating with a cooling rate of -0.5°C/min, and the value of the pure silicon rubber used as reference

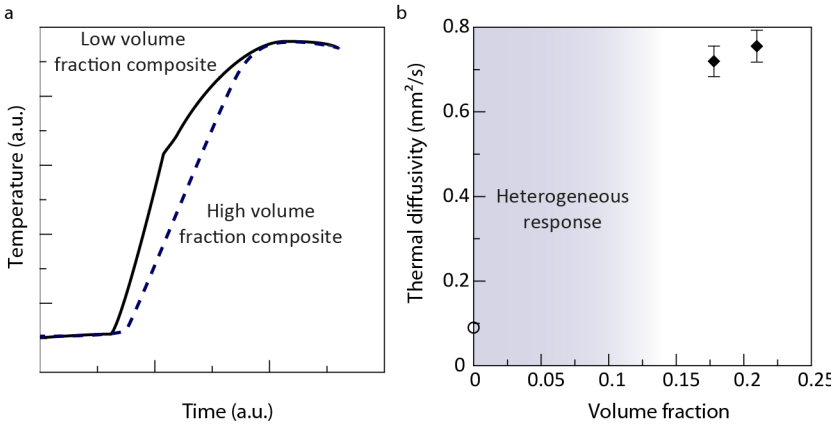

Figure 4.2: a) Typical temperature at the back of a sample as a function of time (after the flash of the lamp) of a low and high BN content composite. b) Thermal diffusivity as a function of volume fraction of platelets in composite frozen at -1°C/min. The grayed area corresponds to the volume fraction where the composite response is composed of two signals.

tion of the wall and the pure matrix can be estimated by image analysis of the microstructure, assuming that for a lamellar composite the area fraction is the same as volume fraction. For the value presented above (see figure 4.1) the value of the walls diffusivities obtained is $D_{\text{wall}} = 2.3\,\text{mm}^2/\text{s}$ with a volume fraction of walls of 0.43. Finally, a wall itself is a composite of aligned boron nitride platelets in a matrix of silicon rubber and can be modeled in the same way.

$$D_{\text{wall}} = \nu_{\text{matrix}} \cdot D_{\text{matrix}} + \nu_{\text{BN}} \cdot D_{\text{BN}} \tag{4.2}$$

With ν_{matrix} and ν_{BN} measured in a previous chapter (see section 3.3.3) by X-ray tomography. Diffusivity of boron nitride in this example is equal to $D_{\text{BN}} = 6mm^2/s$ and its conductivity to $\lambda_{\text{BN}} = D_{\text{BN}} \cdot \rho_{\text{BN}} \cdot C_{\text{BN}} = 6 \times 10^{-6} \cdot 2260 \cdot 800 = 11\,\text{W/m/K}$. This value for boron nitride (even if it is only a rough estimation) is actually lower than both theoretical ones ($\lambda_{||} = 30\,\text{W/m/K}$ and $\lambda_{\perp} = 600\,\text{W/m/K}$). This can be explained by the resistance of the multiple interfaces between the platelets and the silicon rubber. This also explains why the improvement that should result from the increase in BN content is negligible (cf. figure4.2b), because more interfaces are also created in the meantime. The main factor controlling the thermal properties of the composite is therefore the interfaces resistance, just like the properties of bulk boron nitride(see section 4.2.3).

4.2.3 The different ways to align boron nitride platelets

In the first chapter (chapter 1), we detailed different ways to control the orientation of platelet particles. Different techniques can be used, from the application of external fields to a mechanical alignment. Three publications can be found in the literature that discuss the properties gain of a BN/silicon rubber composite when BN platelets orientation is modified. In the first paper, an electric field is used to guide the platelets into templated mold[45] or simply to force an oriented segregation[44]. In the second paper, a high intensity magnetic field (10 T) is use to align the platelets (hexagonal boron nitride presents a small magnetic susceptibility) in the silicon rubber[39]. The study is similar in these articles, the conductivity or the diffusivity is measured for a composite where all the platelet are randomly aligned and the evolution of the thermal properties with the progressive alignment is investigated. Those techniques are limited to low particles content because the presence of too many platelets prevents their rotation even if high intensity fields are used[47]. Because they present a composition similar to that of the composite made by ice templating, their properties are discussed in a following section (see 4.2.2).

The other way to align platelets is tape casting (cf. 1.6.1). Samples made of aligned boron nitride platelets were produced by tape casting and sintered by Spark Plasma Sintering[160, 161]. They present a high relative density (> 90%) and the alignment of the grain orientation has been characterized by XRD. Depending on the conditions (addition of sintering additives and small particle size), the final samples present grains nearly all aligned along the casting direction (see figure 4.3) and the XRD patterns show only the <00l> crystallographic plane peaks in one direction and all the different peaks in the two others directions [b]. Despite the high density and the important texturation of these samples, the anisotropy of the thermal conductivities is relatively low, with a maximum ratio of 1.5 between the one parallel and the one perpendicular to the basal plan (23.7 W/m/K and 15.3 W/m/K respectively), far from the particles ratio of 20. This may be explained by the deleterious effect of the grain boundaries on the thermal transfer (and the remaining porosity) that probably dictates the material property (see section 4.2.2).

4.2.4 Comparison of the different alignment processes

The different parameters that can influence the thermal properties of BN/silicon rubber composites are described in the previous section. Those properties are more sensitive to interfaces than to platelets alignment. However, improvement induced by this process is significant (see figure 4.1), multiplying the thermal diffusivities by a factor of three. To compare the improvement induced by each technique detailed in the paragraph 4.2.2, a relative improvement (RI) can be calculated between the reference state (where particles are randomly oriented) and the state where the platelets present the best alignment, with the conductivity or diffusivity:

$$RI = \frac{(\lambda_{\text{aligned}}, D_{\text{aligned}} - \lambda_{\text{ref}}, D_{\text{ref}})}{\lambda_{\text{ref}}, D_{\text{ref}})} \tag{4.3}$$

The results obtained are plotted in figure 4.4. The relative improvement associated with the processes using external fields is around 20% but the one obtained with ice templating is of nearly 200%. Even if the alignment of the platelets in the two examples from literature is nearly perfect, the relative improvement is rather low compared to the one brought by ice-templating. The difference may come from the drastically increased local platelets concentration. The presence of the walls creates fast thermal path, therefore the material reacts as if it contains more BN. A similar difference exist between materials that present a lamellar and a matrix / inclusion architecture at the macroscale. Another asset of the ice templating is the high solid

[b] This orientation is called "fiber textured" and is typical from the tape casting process[162]

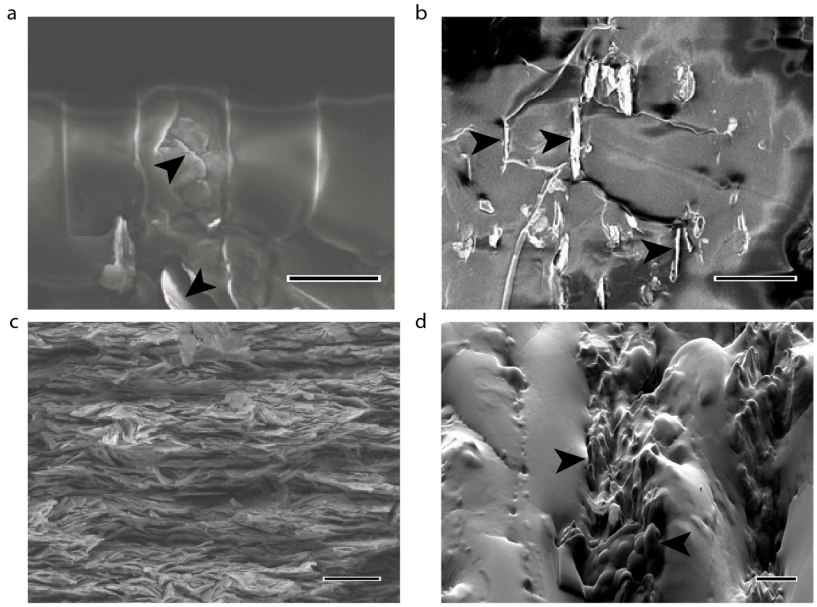

Figure 4.3: Different microstructures obtained with aligned boron nitride platelets. The black arrows indicate some platelets in each microstructure. a) Aligned platelets by an electric field in a templated mold[45] and b) aligned by high intensity magnetic field[39] in silicon rubber. Scale bars: 5 μm. c) Microstructure of a sample made by tape casting[160]. Scale bar: 10 μm. d) Microstructure of a composite boron nitride/silicon rubber at 18 vol.% made by ice-templating. Scale bar: 10 μm.

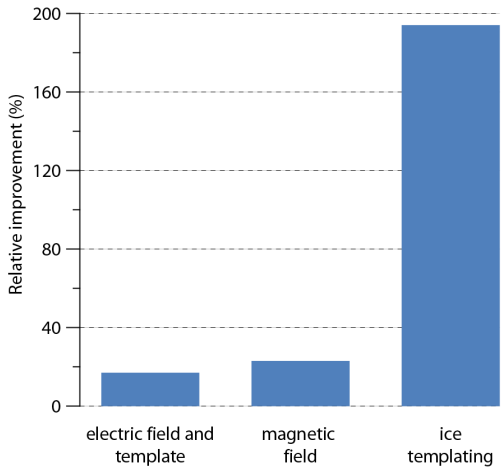

Figure 4.4: Relative improvement of thermal properties of BN/silicon rubber composites for different platelets alignment processes[39, 45].

loading that can be used, here around 20 vol.% compared to 0.5 vol.% for electric field[45] and 5 vol.% for magnetic field[39] respectively.

4.2.5 Conclusions

The thermal properties of BN/silicon rubber composites can be greatly improved by ice templating, because the process is not only able to align the particles but also to change their spatial arrangement. The influence of the different process parameters has been investigated, but as long as a given solid content is used, they do not seem to have important consequences on the final properties. This process lead to a relative improvement of nearly 200% of the thermal properties of BN/silicon rubber composites, a value more than four times higher than the ones obtained by different methods for the same system.

Although the platelets alignment by ice-templating could improve functional properties, building cellular ceramics with platelets may also have an impact on their structural properties. The aspect ratio of such particles open the way of structure difficult to obtain with spherical particles, such as thin walls and large pores. The following section details how the use of alumina particles gave rise to structure similar to that of balsa wood, a particularly efficient cellular material.

4.3 Lightweight and stiff cellular ceramic structures by ice templating

4.3.1 Introduction

The mechanical properties of porous cellular materials directly depend on their cell structure. Natural materials such as wood, because their role is to withstand stresses and to mediate water and nutriments transfer, provide guidelines to obtain cellular materials with remarkable stiffness and tailored porosity. The most common cellular structure encountered in load–bearing natural material is the honeycomb because this geometry provides a very high specific elastic modulus[163]. The pores need to be as parallel and straight as possible while the hexagonal shape maximizes the structural stiffness.

The options to obtain cellular ceramic materials with an oriented, anisotropic porosity are limited when the targeted cell size and cell wall thickness are similar to that of wood (typically 30 μm cell size and less than 5 μm in wall thickness for balsa[164]). Wood structures are defined by a delicate balance between the densities of pores (to have a large accessible area), large and straight pores to limit the pressure drop, and cell structure and wall thickness to provide structural resistance. Cellular ceramics presenting such characteristics can be useful as supports for liquid or gaseous chemical reaction and more generally as fluid carrier. Usual ceramic foams partly fulfill those requirements, such as a high porosity content and high strength, but their low cell connectivity and high tortuosity may restrain their use for those applications. The presence of straight and oriented pores can greatly increase the permeability of a porous support[165, 166].

Today the most common way to obtain cellular material is extrusion, although technical limitations make it extremely complicated to decrease the pore size below a hundred of micrometers or so. Alternatively, direct replication of the wood structure has already been successfully demonstrated[167, 168, 169]. The use of natural wood templates and multiple heat/impregnation treatments can lead to ceramic materials where cellulose is converted into a ceramic phase. Even if the template structure is preserved, which helps retain the mechanical properties, the large number of steps and specificity of the chemistry involved remain important drawbacks[170]. Here we present an alternative and simpler process, based on ice templating, to obtain porous ceramics emulating the structure of wood. Ice templated porous materials have already demonstrated appealing mechanical properties arising from the three dimensional architecture of the structure imprinted by the ice crystals[100]. The process is based on the phase separation that occurs when a colloidal suspension is

frozen, leading to the rejection of the particles by the growing crystals. Because of a strong anisotropy of crystal growth velocities, ice crystals adopt a lamellar morphology. The structure is lamellar and mechanical properties are thus maximized along this direction. The tortuosity of the porous phase in these structures remains low. This process has been successfully used to make unidirectional porous support, with cell size and wall thickness approaching that of natural balsa. Some are based on camphene suspension[171, 172] and the materials obtained present a dendritic and tortuous pore morphology. Others, based on jellified water-based suspensions, get close to the structure of the natural model but their strength and stiffness are usually rather low[173, 174].

A 30 μm pore diameter can be obtained with a slow cooling rate (around -1°C/min), resulting in a low growth velocity[1]. Such conditions nevertheless result in highly tilted pores. Large particles, around a few micrometers, can stabilize the interface and reduce the crystal tilt, resulting in straight and equiaxed crystals at the expense of a greater walls thickness. In order to obtain a honeycomb-like porous structure with thin ceramic walls, in the present paper we use a combination of an ice shaping compound and anisotropic, platelet shaped particles. The growing ice crystals trigger the self-assembly of the platelets[102]. Different mechanisms have been proposed for this alignment, such as shear forces at crystal tip[103] or anisotropic growth rates[133]. Walls constituted of aligned platelets can be significantly thinner than those composed of spheres because the percolation threshold is inversely proportional to the aspect ratio. Simultaneously, we take advantage of the ice shaping properties of zirconium acetate[175, 176] (ZRA) to obtain hexagonal ice crystals and thus a honeycomb-like porous architecture.

We show that this combination can lead to stiff and strong porous cellular ceramic materials with specific mechanical properties approaching that of wood.

4.3.2 Experimental procedure

Suspensions were prepared by mixing distilled water with a zirconium acetate (Saint-Gobain) leading to a concentration of zirconium around 20 g/L, an organic binder (Poly Ethylene Glycol 20M, 4 wt.% of dried powder mass, Sigma Aldrich), and the alumina powder (RonaFlair White Sapphire; produced by Antaria ltd, sold by Merck KGaA) at 13 vol.%. This concentration of zirconium acetate lead to a suspension pH of 4, a necessary condition to obtain hexagonal pores[175]. The particles used in the study were platelets with a diameter around 8 μm and a thickness of 500 nm. Isotropic alumina particles were also used for comparison (Ceralox SPA05, Ceralox Div., Condea Vista Co., Tucson, AZ). Slurries were ball-milled for 20 h with alumina

milling media. The glassy phase precursors consisted of a colloidal suspension of silica (Nexsil 20K, diameter 20 nm, provide by Nyacol) and calcium nitrate tetrahydrate (Sigma Aldrich). The ratio of each precursor was adjusted to obtain a composition of 75:25 molar ratio of Si:Ca ions and 5 or 10 vol% were added based on alumina content.

Freezing of the slurries was done by pouring them into a silicone mold (20 mm diameter, 21 mm height) placed on a cooled copper plate. The copper plate was cooled by silicone oil at a temperature regulated by a cryothermostat. A cooling rate of -1°C/min was used. Once freezing was completed, the samples were freeze-dried for at least 48 h in a commercial freeze-dryer (Free Zone 2.5 Plus, Labconco, Kansas City, Missouri, USA) to ensure a complete removal of the ice crystals. The heat treatment comprised a binder removal step, heating from room temperature to 550°C at 50°C/h followed by a steady stage of 2hrs. Directly after this organic burnout, the samples were sintered at 1550°C for 2hrs with 300°C/h heating and cooling rates.

Geometrical density measurements were made after the removal of one millimeter of material at the top and the bottom of each sample to avoid surface artifacts. The theoretical bulk density was calculated by a rule of mixture to take into account the addition of the glassy phase.

Pore diameters and volume were measured by mercury intrusion porosimetry (AutoPore IV 9500, Micromeritics) with applied pressures up to 200 MPa. The open porosity of the pore walls was deduced from the volume V_m of mercury introduced below a 10 µm equivalent pore diameter and the volume of the sample V_e by the following relation: walls open porosity equals $V_m/(V_m + V_e)$. Samples (dimensions around 18 mm in diameter and 18 mm height) surfaces were first ground to be parallel then the samples were compressed on a testing machine (Shimadzu AGSX), with a crosshead speed of 0.2 mm/min.

4.3.3 Results and discussion

The typical microstructure of a sample made by ice templating with alumina platelets and ZRA is shown in figure 4.5a. The macropores (figure 4.5c) are approximately hexagonal, with a relatively smooth surface resulting from the local alignment of the platelets. The structure also presents a unique pore connectivity and morphology. The pores are arranged in elongated cells (figure 4.6). This feature is possibly a consequence of the large size of particles, able to induce tip splitting of the ice crystal[177]. The morphology of these materials is thus unexpectedly similar to that of wood, which presents the same cell structure[164, 178]. A sample made

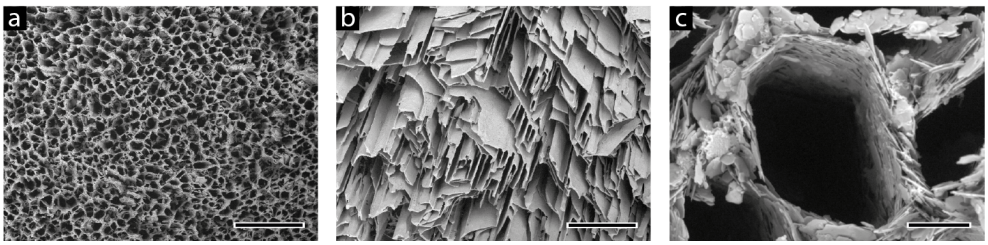

Figure 4.5: SEM micrographs of porous alumina structures obtained under the same conditions with a) large alumina platelets and b) small isotropic particles. Scale bars: 500 μm. Cross-section perpendicular to the temperature gradient. c) Closer view of a macropore. Scale bar: 20 μm.

of isotropic 0.5 μm alumina particles obtained under the same freezing conditions is shown in figure 4.5b. The material containing isotropic particles presents highly tilted pores (approximately at 45 °of the direction of the temperature gradient) characteristic of the structures obtained at low growth velocities (figure 4.5b). The mechanical properties of cellular materials strongly depend on the pore volume and properties of the solid phase. Here the particle rich phase is porous because the ice crystals repel the particles until a critical particle concentration is reached[179]. This concentration is typically around the random close packing for monodispersed spherical particles but lower for less isotropic particles. This porosity drastically impacts the mechanical properties[103] and thus needs to be reduced. For submicromic ceramic particles, the remaining porosity is reduced by a sintering step. In this study, the particles exhibited a 8 μm diameter and a nm thickness, yielding a ceramic phase with lower green and sintered densities. Indeed, the volume of such particles and the low number of particle contacts (due to the high aspect ratio) prevent their rearrangement and coarsening. The Laplace pressure is not sufficient for densification in this case. To improve the mechanical properties, the porosity of the walls must therefore be reduced.

The solution chosen here was to densify by liquid phase sintering. If the glassy phase composition and volume are suitable, its presence can facilitate particle rearrangement. The glassy phase must exhibit a good wettability with particles so that the capillary forces induced by the liquid film between adjacent particles are strong enough to bring them closer while the liquid partially fills the gap. A glassy phase composed of silica and calcia in molar ratio 75:25 was chosen. Previous studies[56, 180] reported a good wettability of this compound with alumina, in conjunction with formation of a calcium aluminosilicate phase at the grain boundary.

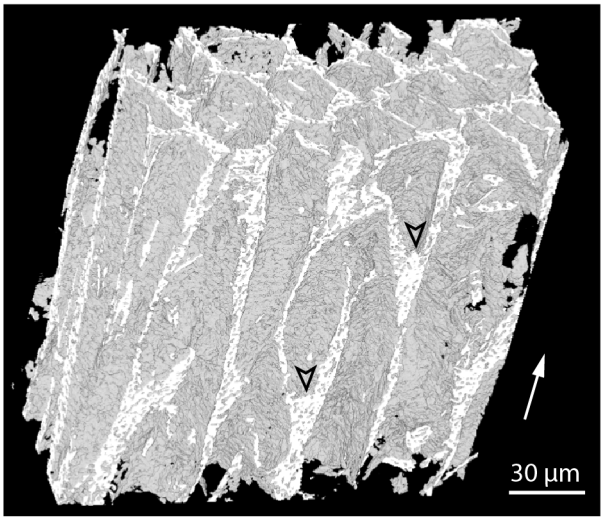

Figure 4.6: 3D structure of the structure obtained by tomography containing alumina platelets and 10 vol.% of glassy phase. The arrows indicate the beginning of a new cell. The white arrow indicates the solidification direction.

An intergranular phase can further enhance the contact strength between adjacent particles. The use of such a glassy phase allows us to decrease the wall porosity in the sample and thus improve the mechanical properties.

The addition of a glassy phase allows densification of the sample during sintering which does not occur in samples without sintering additives (figure 4.7a). However, the macropore size is relatively independent of the amount of glassy phase (figure 4.7c). The shrinkage is therefore due to densification of the ceramic walls. The pore network, assessed by mercury intrusion, is characterized by two different peaks: one corresponding to the intergranular porosity (figure 4.7b) and another for macroporosity (figure 4.7c). The intergranular porosity is significantly decreased by the addition of glassy phase (figure 4.7b). By comparing the amount of the two porosity types with the material volume, the average wall porosity can be calculated as a function of glassy phase content.

The walls composed only of platelets present a high pore content (60%). The only change in the structure after sintering consists of necks created by diffusion at the few contact points between adjacent platelets. The porosity is thus the same as in the freeze-dried green body. The wall density is lower than the one obtained with spherical particles[181] due to the smaller packing ability of high aspect ratio

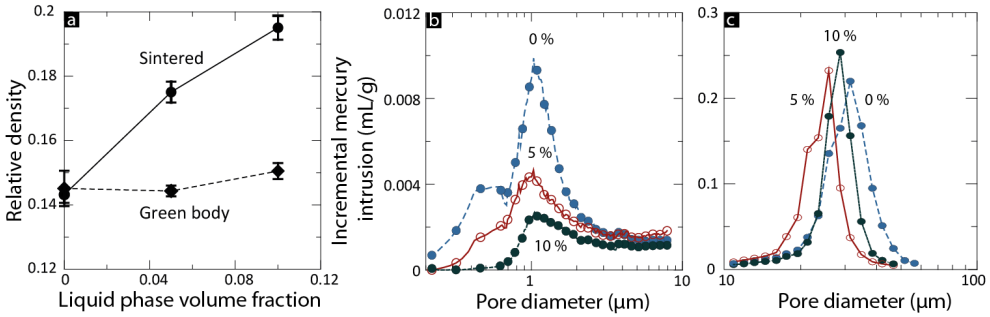

Figure 4.7: Evolution of a) the relative density, b) the intergranular and c) the macroporosity of the cellular material with alumina platelets vs. the amount of glassy phase.

particles. Because of this high porosity, the compressive strength is relatively low. The addition of 5 and 10 vol.% of glassy phase reduces the wall open porosity from 60% to 18% and 4% (figure 4.8a), respectively, which in turn increases the compressive strengths by a factor of 4 and 7, respectively (figure 4.8b). The Young's modulus increase by a factor of 4 (10 vol.% of glassy phase, figure 4.8c). The tilted pore structure obtained with spherical particles results in low compressive strength (2.1 MPa) and Young's modulus (75 MPa), despite a density slightly higher than the samples with glassy phase (0.78 g/cm^3 and 0.73 g/cm^3 respectively). The presence of a glassy phase and rearrangement are illustrated in figure 4.8d and figure 4.8e. Clearly, the addition of glassy phase in the structure greatly improves the mechanical properties by allowing a particle rearrangement, which results in a reduction of the porosity in the walls after sintering.

The mechanical response of the material is drastically modified by the addition of the glassy phase. Not only does the glassy phase fraction increase the compressive strength and Young's modulus, but it also affects the fracture behavior. Typical stress-strain curves for the three different types of materials are shown in figure 4.9. The behavior of the sample containing 5 vol.% of glassy phase is non-linear after a stress of 8 MPa. Observations of the fractured samples revealed localized damage of the sample in contact with the dies. The two other compositions are characterized by brittle facture behavior, arising from unresolved tensile stresses due to the friction on the dies. Along with the increase of mechanical properties, the amount of glassy phase modifies the fracture behavior of the samples. By decreasing the porosity in the walls, a compromise is reached when the porosity is low enough to obtain interesting macroscopic properties and at the same time high enough to promote

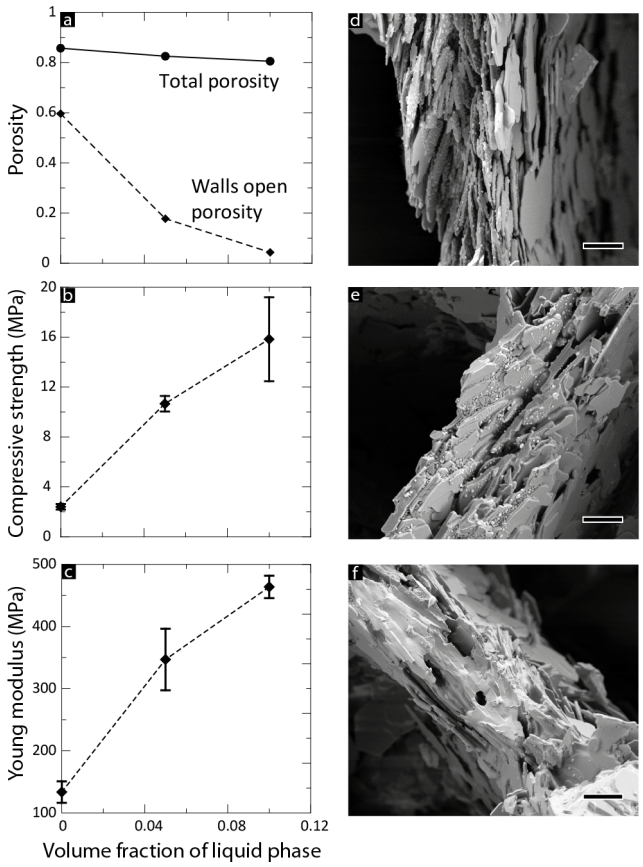

Figure 4.8: Influence of glassy phase content on the structural and mechanical properties of the cellular material containing alumina platelets. SEM pictures of structure with d) 0 vol.%, e) 5 vol.%, and f) 10 vol.% of glassy phase. Scale bars: 5 μm.

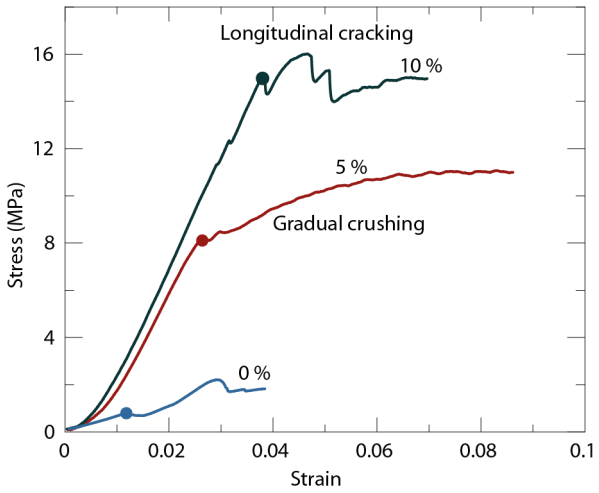

Figure 4.9: Typical stress-strain curves obtained under compression as a function of the glassy phase content. Dots represent the first recorded crack propagation.

gradual crushing instead of a catastrophic failure (here at 5 vol.% of glassy phase). The failure of the sample under load is progressive, a behavior similar to that observed in ceramic foams. When the porosity in the wall becomes too low (10 vol.% of glassy phase), the usual failure mechanisms are observed with longitudinal crack propagation throughout the sample.

The strengths of the porous structures obtained here are plotted in figure 4.10, along with similar structures and macroporous foams made of alumina. The strengths of our materials are closed to the maximum of the one obtained with foams with the same level of porosity. The two materials close to that are a camphene-based material[172] the alumina wood replica[169], which are made by complex and multi steps processes. The specific Young's moduli of our materials and the ones with similar microstructure are presented in table 4.1. The structures reported by Hunger et al.[103] present approximately the same pore sizes and wall thicknesses but are comprise polymer (gelatin and chitosan) and alumina platelets. The presence of a polymeric phase and a lamellar pore structure decreases the stiffness and resistance of the unit cell. Rambo et al.[169] use an Al-vapor deposition process to transform natural wood into α-Al_2O_3 while retaining the wood microstructure. However, the specific stiffness is clearly below natural wood (0.11 GPa/(g/cm^3)) compared to 10 GPa/(g/cm^3)) due to the presence of defects in the wall that, according to the authors, arise from the deposition. The specimen showed in this study presented

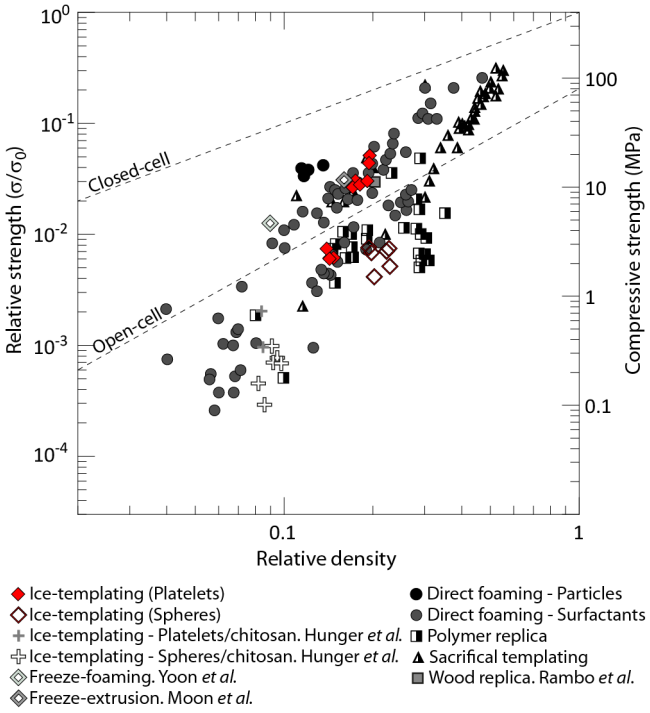

Figure 4.10: Compressive strength of our ice templated alumina structures compared to macroporous alumina obtained by various techniques: direct foaming, polymer replica, sacrificial templating[182], wood replica[169], ice templating of composites[103, 135], freezing/foaming[183] and freezing/extrusion[172] . Reproduced from Gonzenbach et al.[182].

Material and reference	Specific Young's modulus (GPa/(g/cm^3))
Alumina platelets (this study)	0.64
Alumina spheres (this study)	0.10
Alumina platelets/chitosan[103]	0.13
Alumina spheres/chitosan[135]	0.03
Alumina wood replica[169]	0.11
Zirconia ice-templated with camphene[184]	0.53
Carbon wood replica[167]	4.08
Balsa wood[164] (transverse / longitudinal)	1 / 10

Table 4.1: Comparison of specific Young's modulus for different materials with similar architecture

higher characteristics because of a stiffer and defect-free unit cell material. However, the properties of these materials are still not quite at the level of natural balsa in terms of specific stiffness (0.64 GPa/(g/cm^3)), see table 4.1). Another wood replica was obtained by pyrolysis[167], leading to a carbon-based structure with specific properties close to that of the template (4 GPa/(g/cm^3)). The walls probably retained the structure of wood at a smaller scale, such as the crystallographic alignment of cellulose fibers, which leads to an increased stiffness.

The materials obtained share certain structural features with wood, such as hexagonal cells of similar dimensions (around 30 µm) and relatively thin cell walls. These bioinspired materials exhibit interesting mechanical properties compared to other similar structures reported in the literature but also compared to other alumina foam made by various techniques. However, they are still short of the value of wood or its carbon replica by an order of magnitude in stiffness. The ice templated materials obtained here do not mimic all of the complex wood architecture, and in particular the internal structure of the cell's wall. The benefit of the trade-off is the relative simplicity and versatility of the processing approach presented here, compared to the wood replica techniques.

4.3.4 Conclusions

Cellular ceramics have been synthesized with structural guidelines derived from wood. To reproduce wood-like features, the ice templating process has been used to obtain large and straight pores with self-assembled platelets during freezing. Because the honeycomb cell structure is known to maximize the specific Young's mod-

ulus, zirconium acetate addition was used to promote such a structure. The harmful effect of platelets on densification of the walls formed after ice templating has been countered by the addition of a glassy phase. The resulting specific properties are relatively close to that of wood in terms of compressive strength but still an order of magnitude short in stiffness. Indeed, the macrostructure of wood have been successfully mirrored here, but only at the length scale of macropores. Further work to control the microstructure at a finer scale is required.

Chapter 5

Second level- Control of walls alignment

5.1 Introduction

Now that the benefits of platelets alignment have been illustrated for two different properties, a second level of organization is introduced in this chapter, the control of the pores long range order. A sample obtained by ice-templating exhibit orthotropic properties, the lateral orientation of the pores being random over large dimensions. Bringing order to the pore orientation gives the possibility to create layered composites where both phases are lamellar and interconnected. The other asset is a better stacking of the walls when the material is compressed (see chapter 6 for more details). But the aligmment of the ice crystals over large dimensions required to influence their growth, which has proven to be difficult so far. A new technique have been developed, named 'freezing under flow', and is detailed hereafter.

Piezoelectric ceramics have been chosen to illustrate the profit of this two-level architecture: crystals are aligned over several centimeters and platelets are locally aligned by the solidification front. To palliate the poor densification behavior of large platelets, a different strategy has been employed, the templated grain growth.

This chapter have been submitted as an article (see page viii).

5.2 Templated grain growth in macroporous material

5.2.1 Introduction

Many functional properties depend on the crystallographic orientation of a material, and single crystals are used in many applications to take advantage of crystallographic and property anisotropy. Single crystals are, however, frequently difficult to grow with adequate cost, size, shape, and compositional homogeneity for some applications. For this reason, a group of processing strategies has been developed to produce polycrystalline ceramics with aligned grains, called textured ceramics. One particularly promising approach that has been widely applied is Templated Grain Growth [185], or TGG. For TGG, a small population of large templates (5-50 μm) is dispersed in a fine particle matrix. The templates are aligned during green forming, usually by tape-casting, and controlled epitaxial grain growth from the templates results in microstructures constituted of large and aligned grains.

To date, TGG and texturing methods have been successful at producing monolithic ceramics and microstructure composites with improved properties relative to random ceramics. But, the processing strategies used are not usually conducive to producing some types of composite architectures that combine controlled macroscopic porosity with textured ceramic layers. To facilely produce porous composite TGG structures, we propose a modified ice templating approach.

Ice templating is a well establish technique to make porous ceramics and composites [1, 96]. It uses the growth of ice crystals in a suspension and their subsequent removal to template and control the porosity of diverse materials. This technique is also a promising approach for self-assembly [100] because particle consolidation between the ice crystals takes place on the micron scale while, at the same time, the material obtained is on the mm to cm size scale. This hierarchical aspect makes it an ideal tool to realize composites with various interconnections and at the same time control the microstructure of the constitutive parts. For instance, ice-templating has already been used to make 3-1 piezoelectric composites [186] demonstrating materials that have the same electromechanical coupling coefficient as bulk material but an adaptive acoustic impedance, as well as relative permittivity and greater hydrostatic piezoelectric properties. This process has also recently proven effective to align anisotropic building blocks, such as graphene [102] or alumina platelets [103]. To control the composite microstructure and obtain real 2-2 and 3-2 composites, a lamellar structure is needed. Some modification of the process have been developed to obtain lamellar pores over large dimension [90] but

have been hard to replicate so far.

In this study we present a method to combine ice templating and TGG. We first demonstrate how to make textured porous alumina as a model system and then apply the process to sodium potassium niobate, KNN, a promising lead free piezoelectric composition. We also show that the various ceramic walls produced during ice templating can be aligned based on the application of a second thermal gradient during the freezing, to produce 2-2 type composites with ordered lamellar macropores between textured KNN layers. The complex interconnections and morphologies of the textured and ice template materials make them difficult to adequately characterize with standard tools like XRD rocking curve analysis or Lotgering factor. Therefore, we propose a different strategy coupling XRD and morphological descriptors with a modification of the March-Dollase equation.

5.2.2 Experimental procedure

For the alumina samples, commercially available alumina platelets (RonaFlair White Sapphire; produced by Antaria ltd, sold by Merck KGaA) with 8 μm diameter and 500 nm thickness were used as template particles and isotropic alumina (TM-DAR, Taimicron) of 100 nm as matrix particles. Nanoparticles of silica (Nexsil 20K, diameter 20 nm, provide by Nyacol) and calcium carbonate (Sigma Aldrich) were added as liquid phase precursors in 75:25 molar ratio of $SiO_2 : CaO$. The matrix powder, liquid phase precursors and a binder (PEG20M, 4 wt.% of the powder mass, Sigma Aldrich) were mixed with distilled water and ball-milled for 20h and the template particles were added only three hours before the end of the milling step to avoid any excessive breakage of the particles.

For conventional ice-templating, the slurry was poured into a cylindrical Teflon mold and placed in contact with a copper cold plate. Temperature was controlled by circulating refrigerated silicone oil through the copper plate, and the freezing rate was -1°C/min. Once the sample was completely frozen, it was removed from the mold and freeze dried for at least 48 h in a commercial freeze-dryer (Free Zone 2.5 Plus, Labconco, Kansas City, Missouri, USA) to ensure a complete removal of the ice crystals.

In order to align the ceramic walls during ice-templating, freezing took place while the slurry flowed over the freezing surface. A rectangular mold made of silicon rubber was placed on an inclined copper plate. The slurry was then introduced at the top end of the mold and allowed to flow down the inclined plane of the copper plate as it froze. Slurry that reached the bottom of the mold was recirculated using a peristaltic pump. A cooling rate of -1 ° C/min was used for all the samples. Once a

first layer (of around 5 mm in high) of aligned crystals was frozen, the slurry recirculation was turned off, the copper plate was leveled, and the mold was filled with the remaining slurry. Once freezing was completed, the samples were freeze-dried under conditions identical to those used for alumina.

The sintering cycle of alumina sample frozen at -1°C/min was chosen in accordance with the study by Pavlacka et al. [180] with a sintering step at 1550°C for 90 minutes. For SEM observations, the samples were fractured and thermally etched at 1450°C for 20 minutes to better reveal the grain boundaries.

For KNN samples, anisotropic sodium niobate (NNT) platelets 15 μm in diameter and 1 μm thick and sodium potassium niobate (KNN) particles of 0.5 μm in diameter as template and matrix particles were synthetized. The NNT particles were prepared by Topochemical Microcrystal Conversion [187, 188] of bismuth niobate seeds according to the procedure detailed by Chang et al. [189]. The KNN particles were made by a conventional mixed oxide synthesis the mixed oxide synthesis described in [189]. 1 mol% of copper oxide (Sigma Aldrich) was added as liquid phase precursor.

The slurry preparation conditions and freezing conditions for KNN were identical to that of alumina.

The sintering cycle of the KNN sample was chosen in accordance with the study of Chang et al. [189], with a sintering step at 1115°C for 4h and an annealing step at 1125°C for 3h.

SEM picture were taken by a Supra 55 microscope (Zeiss) on gold coated samples. Samples were scanned on a XX with a 3.4 μm^3 voxel size on a disk sample of 3 mm diameter and 3 mm in high. The directionality measurement was made with the plug-in named 'directionality' of the free software Fiji. XRD measurements were performed on a D5000 setup (Bruker).

5.2.3 Results and discussions

Ice templating and templated grain growth

There are several examples where ice crystal growth effectively organizes anisotropic particles [102, 103], but none have demonstrated the ability to align a small fraction of platelet particles in a fine particle matrix as required for TGG. Therefore, it was not clear whether platelets in a powder/platelet mixture would align sufficiently for TGG, or whether the small particles would screen the most important alignment forces.

Figure 5.1a shows that the platelets in the green body are generally aligned in the same direction as the ceramic wall, but there is some misorientation. Most

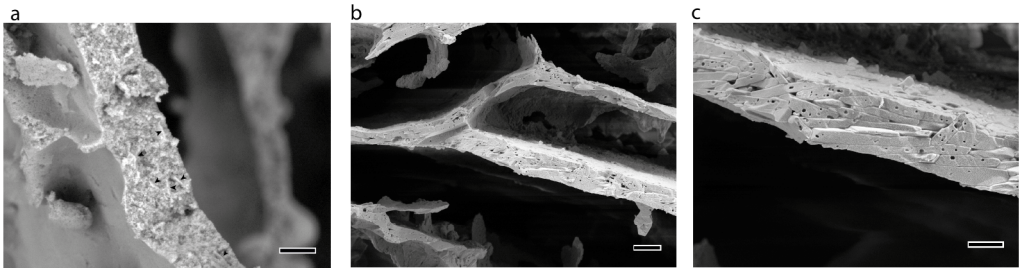

Figure 5.1: a) SEM observations of the platelets (black arrows) alignment in the green body. Scale bar 10 μm. b) Close view of wall's organization after sintering, showing the correlation between wall and grain orientation. Scale bar 10 μm. c) SEM picture showing the grain high alignment. Scale bar 5 μm.

reports on textured ceramics by TGG use the shear forces generated by the doctor blade to align the template particles. In this case, the size and aspect ratio of the platelets are critical to achieving good alignment. The mechanisms involved in platelet alignment during ice templating are unclear, but, intuitively, alignment of the particles seems to be largely a result of compaction between the laterally growing ice crystals, similar to the alignment of platelets during unidirectional pressing. The most important differences between the two situations being the magnitude of the compaction force and the fact that ice templating takes place in a colloidal suspension where interparticle forces, preferential surface interactions between the platelets/ice crystals interactions, and purely steric impingement minimization by platelet rotation are key parameters.

The fact that platelets are aligned in the center of the walls supports the hypothesis that the orientation of the platelet comes from steric impingement - in this specific case, the ice does not directly interact with the platelet. Instead, the ice crystal compacts the ceramic particles which in turn push on and align them during the concentration. Even if the collective efforts of the particles are sufficient to orient the platelet in one direction, the lateral orientation is not as well controlled. The platelets are nevertheless well aligned in the direction of crystal growth, and thus are compatible with the realization of textured composites.

The resulting microstructure is shown in figure 5.1b and c. These samples have a lamellar structure where 10-20 μm thick pores are separated by 5-10 μm thick ceramic layers. In figure 5.1b, large tabular grains are easily observed within the ceramic walls, and the orientation of those grains is generally parallel to the border of the walls, even the wall itself is divided or wavy. Figure 5.1c shows a closer image

Figure 5.2: Typical porous structure obtained by ice-templating showing the different domains of orientation. Scale bar 0.5 mm.

of the ceramic walls, and it is clear that the major part of the grains in the wall is aligned within 15°the wall orientation.

While the images in figure 5.1 show that TGG is possible within individual walls by ice templating, we must align the walls within the sample in order to benefit from the texture in each individual wall. Figure 5.2 shows a wide view of a microstructure that is typical of ice templated ceramics. The sample is divided into individual domains where the walls are well aligned, but the orientation distribution of the walls taken over the entire sample is random.

Control of the lateral wall orientation by freezing under flow

Controlling the lateral orientation of the ceramic walls is an important challenge in ice templating, and it is critical to realizing the improved properties we seek from the textured ceramic walls. Previously, walls were aligned during ice templating by patterning the ice nucleation surface in conjunction with small vibrations [90, 190]. Because this process is inherently linked to the specific freezing setup and has proven difficult to replicate, we developed a different and robust alignment technique.

The ice crystal orientation is intimately related to the direction and magnitude of the applied temperature gradient, so adding a second gradient could orient the crystal growth in a direction imposed by the combination of the two gradients. The problem of this method comes from the complexities of controlling the superposition and relative intensities of such gradients. If the second gradient is too strong, ice

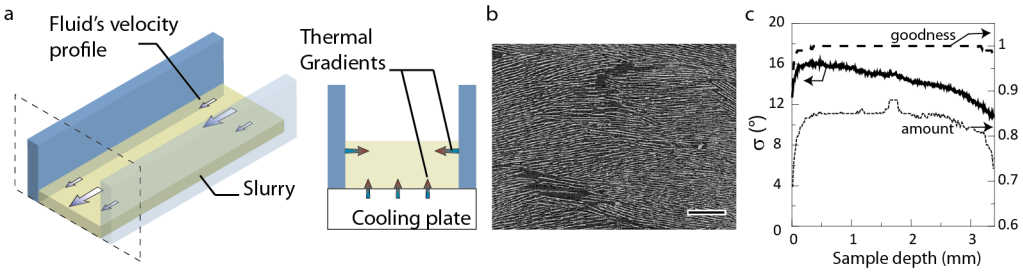

Figure 5.3: **Freezing under flow: process and structures** a) schematic representation of the freezing under flow setup, depicting the fluid velocity profile and a cross section perpendicular to the flow showing the two different orthogonal gradients. b) Cross section of an X-ray tomography of the sample, showing the long range order in the wall alignment. Scale bar 0.5 mm. c) Results of the morphological characterization from the tomography 3D picture.

crystals will start to grow from the side of the mold and if it is too weak, there will be no influence at all. Instead of simply adding another refrigerated part on the experimental setup, we flowed the slurry along the cooling plate. Because the suspension is viscous, a typical u-shaped velocity gradient is introduced in the fluid (see figure 5.3a). The slurry that flows along the sides of the mold becomes cool faster than the slurry in the center. This velocity gradient is thus translated into a second temperature gradient. The intensity of this gradient is enough to align ice crystals over large dimensions, typically a few centimeters (see figure 5.3b). Another benefit of this technique is that the lateral gradient introduced is self-regulated. Because the ice crystal growth starts from one side, the size of the liquid part decrease and the velocity gradient increases, which correspondingly increases the temperature gradient. The increase can help balance the effect of the lower thermal conductivity of the frozen layer. The microstructure is thus similar from one side to the other in the material. Domains can still be found in the microstructure (see figure 5.3b) but the orientation mismatch between them is small (less than 10°) compared to samples frozen under the typical static conditions.

In order to characterize the wall orientation distribution, we imaged the samples using X-ray tomography. The directionality of the structure was characterized by measuring the brightness gradient and its orientations for all the slices of the tomogram. For each slice, a histogram of the sum of gradients at each orientation is made and a Gaussian fit is applied. The output of this measurement is the

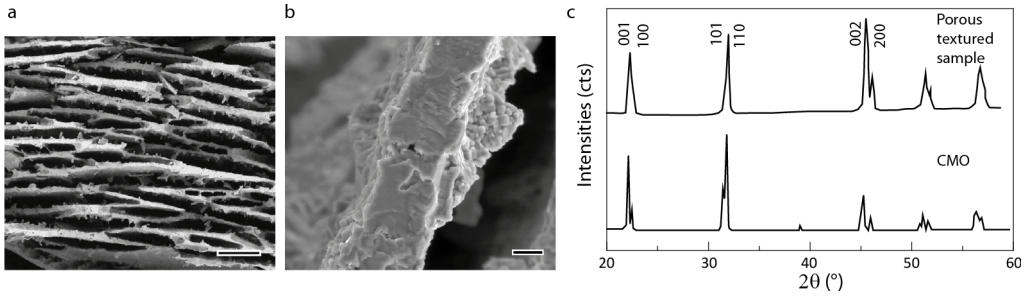

Figure 5.4: a) Microstructure of sample frozen under flow, showing the alignment of ceramic wall. Scale bar 100 µm. b) SEM picture of a wall showing the large cubic grains. Scale bar 10 µm. c) Comparison of XRD pattern obtained with textured composite and non-textured sample (CMO stand for Conventional Mixed Oxide, reproduced from [189]).

evolution of the direction of preferred orientation in the volume (the mean of the Gaussian fit) and the associated dispersion (the standard deviation of the Gaussian fit). The results of this measurement are shown in figure 5.3c. The orientation in the structure follows a Gaussian distribution, as the quality of the fit approaches 1 over the entire sample. The dispersion evolves from 16°to 10°, revealing an evolution of the microstructure. This type of difference could come from the sample preparation or microstructure evolution during the freezing. The number of pixels in the image with the preferred orientation is more than 80% over the entire sample (see figure 5.3c) meaning that the vast majority of the microstructure is textured. Freezing under flow is thus able of controlling the orientation of ice crystals over a large sample with a small dispersion.

Textured piezoelectric composite

Given the results presented above, it is clear that ice-templating can texture grains in ceramic walls of a porous body and align those walls in two directions in a single processing step with alumina, a model material. In order to test the ability to do this in a functional material, the same process has been applied to a KNN powder. We chose a piezoelectric material to demonstrate that textured composites, like those required in some sensor and transducer applications, can be made in a single processing step. The microstructure of the porous sample is presented in figure 5.4a and 5.4b. The microstructure obtained (see figure 5.4a) is similar to the alumina

sample because the ice templating process is not strongly influenced by the material composition, but rather the physical characteristics of the particles, platelets, and the suspension The large grains present in the wall (see figure 5.4b) are cube shaped, due to the weakly orthorhombic crystallographic structure of KNN. As was the case in alumina, the ice crystal growth effectively aligned the NNT and dense and textured walls are obtained after sintering.

The presence of preferred grain orientation has been investigated by XRD measurement. Two XRD patterns are shown in figure 5.4c: one that represents a non-textured sample obtained by a simple mix of KNN precursors and the other the response of the porous textured composite. A clear texture of the <00l> plane is present in the sample made by ice-templating. However the texture is not as good as in samples made by tape-casting [189] and the Lotgering factor of the sample is only 21%. Because of the relatively low depth of penetration of the X-rays, only a few walls contribute to the XRD pattern. This response is affected by the small dispersion existing in the wall orientation (see figure 5.3). In order to better quantify and optimize the structure, and thus the final properties, the orientation of the grain in the wall and orientation of the wall themselves has to be included in the measurement.

Texture measurement in composite, layered materials

The final texture of the composite are a result of the superimposition of two distinct alignments present at two length-scales: the particle alignment in the wall and the wall alignment in the composite. The piezoelectric response, or any other functional properties of a material, is directly linked to the dispersion of crystallographic orientation of the whole sample, not just the texture measured in the first few layers. Whatever the type of distribution that the grain orientation follows, the Full Width at Half Maximum (FWHM) of this distribution is characteristic of the existence of a preferred grain orientation and of its quality in the material. The orientation of grains in bulk textured material can be measured by several XRD methods, like pole figure or rocking curve [162]. More specifically, the orientation distribution in materials made by templated grain growth is known to follow a March-Dollase (MD) distribution [180, 162] (5.1). In a first approximation we consider that the templated grain growth that occurs in the wall of our samples follows the same type of distribution as the one in tape cast samples.

$$MD(f,r,\omega) = f(r^2 cos^2\omega + \frac{sin^2\omega}{r})^{-3/2} + (1-f) \tag{5.1}$$

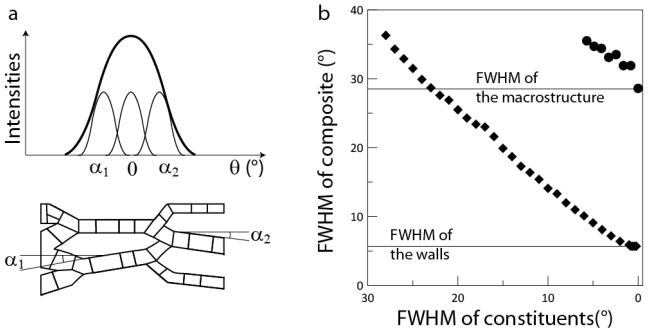

Figure 5.5: **Model of the composite texture** a) Representation of the cubic grain textured wall slightly misaligned and the contribution of those walls in the material global orientation distribution. b) Evolution of the FWHM of the composite with respect to the FWHM of the constituent. Dots represent the evolution of the composite response with the reduction of the grain orientation distribution. Losanges represent the evolution of the composite response with the reduction of the wall orientation distribution.

The porous material made here can be considered as a combination of layers, each one of those slightly disoriented with respect to the surface (5.2), as depicted in figure 5.5a.

$$W = f(r^2 cos^2(\omega - \alpha_n) + \frac{sin^2(\omega - \alpha_n)}{r})^{-3/2} + (1 - f) \tag{5.2}$$

Where α_n is the angle between wall direction and the reference plan. The overall texture of the composite can thus be modeled as the sum of the same MD functions, each of them shifted from an angle α. Because α represents the shift between the reference plane and the wall orientation, it follows the same Gaussian distribution as the one previously measured by tomography. By adding a large number of MD functions shifted by a random angle following a Gaussian distribution, one can model the behavior of a textured composite (5.3), represented by the FWHM of this distribution.

$$W_{\text{Composite}} = \sum_{1}^{N_{wall}} f(r^2 cos^2(\omega - \alpha_n) + \frac{sin^2(\omega - \alpha_n)}{r})^{-3/2} + (1 - f) \tag{5.3}$$

with $\alpha_n \sim N(\theta, \sigma)$, where N is a Gaussian distribution of mean θ and standard deviation σ. Because templated grain growth in alumina has already been studied, the parameters of the MD functions, f and r, are known for different compositions

[180] made by tape casting. As we know the MD funtions and the Gaussian distribution of the wall, we can calculate the FWHM of composite distribution but also model its evolution with the Gaussian and MD parameters. The FWHM of the composite as produced in this study is 36°, which is relatively high compared to the measurements made on tape cast materials. This value is greater than both FWHM of Gaussian distribution and MD function, 28°and 5.7°respectively. In figure 5.5b, the evolution of the composite FWHM versus the two parameters, the Gaussian standard deviation and the MD parameter r is shown. Reducing the FWHM of both distributions tends to decrease the FWHM of the composite. From this data, it is clear that better aligning the individual ceramic walls during ice templating, rather than improving the texture within the walls, is more important for obtaining high texture quality composites in the future. This deviation of the walls could be reduced by optimizing the freezing under flow process, for example, by increasing the magnitude of the lateral temperature gradient (thus an increase in the flow velocity). Indeed, the texture quality within the walls could be improved by improving template alignment within the walls, but it would be a relatively small increase given the level of misorientation between the walls themselves (the smallest FWHM reported to date with alumina is 4.6°[180]).

5.3 Conclusions

We demonstrated here in alumina and KNN systems that ice-templating combined with template grain growth is an effective method to produce textured, macroporous materials. The growth of ice crystals is used to align platelets that are used afterward as seeds for templated grain growth. To retain the benefits arising from this local texture, a "freezing under flow method" has been developed to control the long range order of the lamellar ice crystals, and thus ensure both short and long range order of the grains orientation. This novel method is robust and independent of the material used. The original dispersion of orientation of the ice crystals compromises the optimization of the functional properties and needs to be reduced, as suggested by the model developed here. This could be achieved by modifying the freezing conditions, which requires a more comprehensive study of the process parameters. The principles demonstrated here could be the basis for hierarchical, multifunctional composite materials, including structural and piezoelectric ceramics.

Chapter 6

Third level- Control of the interfaces properties

6.1 Introduction

This final chapter detailed how we assembled the two previous architectures with a new one, the control of the interfaces, towards the fabrication of material inspired by the structure of nacre. The mechanical properties of nacre are remarkable: its toughness is nearly two orders of magnitude above each of its constituents, due to its hierarchical architecture (c.f. section 1.7.1). Because those reinforcement mechanisms are extrinsic, the reproduction of such organization can be used to improve the toughness of ceramics, while retaining their intrinsic assets, such as their high strengths, high stiffnesses and their ability to operate at high temperature. This chapter have been submitted as an article (see page viii).

6.2 Strong and tough bioinspired ceramics from brittle constituents

6.2.1 Introduction

Ceramics exhibit among the highest stiffness and strength of all known material classes [191]. Because of the strong and directional bonding between constitutive atoms, they present a high fusion temperature and thus a high thermal stability. Being composed of mostly light elements, they are also lightweight compared to most metals. This property combination predestined them to be the best material

choice for high stress and high temperature operative conditions. However, the iono-covalent bonds limit most common plasticity mechanisms and therefore prevent any ductile behavior. This lack of plasticity is often the main limitation for the use of ceramic materials, resulting frequently in catastrophic and unpredictable failure [62] which greatly limits their range of applications. Damage-resistant ceramics are thus in great demand. However, countless damage-resistant biological materials comprise ceramics and are used for structural purposes [67, 68] in nature. The most famous example is the nacreous part of seashells where the brick and mortar structure comprising 95 vol.% of platelets of polycrystalline aragonite ($CaCO_3$) and 5 vol.% of a protein is extremely effective at restricting crack propagation [70] and presents a toughness orders of magnitude greater than either of its constituents [71, 192]. Nacre toughness is achieved through numerous extrinsic mechanisms that include viscoelastic deformation of the protein layer [193], mineral bridges rupture, and inelastic shearing and frictional sliding during platelets pull out [70].

Tough ceramic materials could be obtained by translating the specific microstructural and interfacial structures present in natural systems to engineering materials [99]. This could be achieved by building 'brick and mortar' organized structures using anisotropic particles as building blocks combined with a ductile phase. The alignment of anisotropic particles can be achieved by sequential deposition methods [49] for thin films but not for bulk materials.

The most successful attempts at replicating nacre so far have been obtained with ice templating, a well-established materials processing route [99]. Ice templating consists of the formation of a porous structure templated by the growth of ice [100]. A complex strategy based on numerous sintering, pressing, chemical and thermal treatments, and infiltration steps lead to an 80%/20% ceramic/PMMA composite with controlled organic/inorganic interface chemistry [194]. The resulting toughening properties are impressive due to the presence of microstructural features similar to nacre, such as a few ceramic bridges and a strong ceramic/polymer interface.

Such approaches nevertheless suffer from severe limitations. Because the design is based on the presence of a ductile phase, the materials exhibiting the highest toughness all comprise at least 20 vol.% of a polymeric phase, restricting de facto their useful temperature range to mild temperatures (200°C or less). In addition, the approach relies on freezing to form the elementary bricks of the structure, thereby imposing a lower limit (10 μm) of the layer thickness that can be achieved. Refining the ceramic layers thickness to the submicrometer range is critical to increase the number of interfaces and thus improve the strengthening and toughening mechanisms but has not been achieved so far. Finally, the processing route still includes

too many steps to make it viable beyond the lab scale. Here we demonstrate the use of a simple two-step processing route to obtain fully ceramic, layered bulk materials with submicrometer layer spacing that exhibit not only an unprecedented toughness for a ceramic material, but also, because it comprises only brittle constituents, a very high strength and stiffness.

6.2.2 Methods

Suspensions preparation

All the constituents where added in distilled water and then ball-milled for 24 hours, except the alumina platelets that have been added 3 hours before the end of the cycle to avoid any excessive breakage by the milling media. A rheology modifier (Carbopol ETD 2691) was added to form a soft gel (yield stress suspension) in order to avoid any settling of the large particles during the freezing and thus ensuring the homogeneity of the sample throughout the specimen.

Freezing under flow

To obtain dense structures by pressing the porous sample obtained after ice templating, further control of the crystal growth is needed to obtain parallel crystals over large dimension. Indeed, the crystals are vertically aligned in the direction of the temperature gradient, but because nucleation occurs at different spots, different domains of lateral orientation are present [195]. To induce long range order of the crystals, different strategies have been developed [196]. Here we use a method in which we let the slurry flow on the cooling plate where freezing occurs, leading to a second perpendicular temperature gradient during the freezing. The crystals thus guided in two directions are all parallel, and we repeatedly obtain sample of relatively large dimensions (a few centimeters) with aligned crystals. A 1°C/min cooling rate is used for all suspensions.

Field Assisted Sintering (FAST)

The equipment used for sintering is a HPD25 device from FCT System GmbH. The sample is compressed between two graphite punches inside a cylindrical graphite die (20 mm diameter). The heating of the sample is obtained by injecting electrical current through the punches. This leads to a very high heating rate and the presence of the electrical current accelerates the sintering. The FAST device is known to

allow sintering ceramics and metals at lower temperature than conventional sintering resulting in finer microstructures due to the applied pressure. As described, a system composed of alumina platelets (7 μm diameter, 500 nm thickness), alumina nanoparticles (diameter around 100 nm), and a silica-calcia liquid phase (diameter around 20 nm) have been used. The molar composition of 75:25 ($SiO_2 : CaO$) have been chosen because of its high wettability of alumina surface and a relatively high melting point [180, 197, 56] between 1300°C and 1500°C. The densification behavior of different compositions is described in figure 1B. The linear shrinkage rates were obtained from the movement of the die during the sintering. All the relative density of the sample prepared here are above 98% after sintering at 1500°C with 100°C/min heating rate.

Microstructural characterization

SEM pictures were taken on uncoated samples by a Supra 55 microscope (Zeiss) and a ZEISS NVision40. The pictures were taken at low acceleration voltage (typically 1 kV) to avoid any charging effects.

Preparation of SENB and bending samples

Disk shaped samples with 20 mm diameter were obtained after sintering. Beam shaped specimens with dimensions around 14x2x2 mm^3 where then cut from the sintered disks. The beams for bend testing where mirror polished and beveled to avoid any crack departure from the sides. SENB test specimen were first notched with a diamond saw of 200 μm thickness and then the bottom of each notch was sharpened by repeatedly passing a razor blade with diamond paste (1 μm). Using this method, the final notch radiuses were always below 40 μm. At least 5 specimens were tested for each composition and setup.

Determination of crack length

The indirect method usually used to determine crack length is based on complaisance evolution during cyclic loading. However in our case this method has proven to be unusable here because the repeated cycles applied induce small crack propagation, even at low stress. We instead used a simple equivalence between complaisance and crack length on an SENB test. The complaisance were calculated thanks to the relation $C = u/f$, where u and f are the displacement and force at each point after departure of a crack, respectively. Then the crack length was recursively calculated

with (6.1).

$$a_n = a_{n-1} + \frac{W - a_{n-1}}{2} \frac{C_n - C_{n-1}}{C_n} \tag{6.1}$$

where W is the thickness of the specimen, a and C respectively the crack length and complaisance calculated at the n and $n-1$ step.

Details on J-integral calculation

To assess the different mechanisms that occurred during the stable crack propagation (crack length< 200 µm), a J-integral versus crack extension has been calculated as the sum of elastic and plastic contribution, a method already used to measure the properties of bone [67, 198] and similar structures [194, 64]. The elastic contribution J_{el} is based on linear-elastic fracture mechanics ($J_{el} = K_{IC}/E'$), The plastic component J_{pl} is calculated with the relation (6.2):

$$J_{pl} = \frac{1.9 A_{pl}}{Bd} \tag{6.2}$$

where A_{pl} represents the plastic area under the load-displacement curve, B the specimen lateral dimension and b the uncracked ligament. A geometric mean of the local stress intensity factor leads to an equivalent stress intensity factor (6.3).

$$K_{JC} = \sqrt{(J_{el} + J_{pl})E} \tag{6.3}$$

with K_{JC} the back calculated stress intensity factor, J_{el} and J_{pl} elastic and plastic contribution of the J-integral and E the young modulus of alumina.

6.2.3 Processing strategy

Inspired by structural guidelines derived from the study of nacre, we demonstrate dense ceramic materials defined by five structural features, spanning several length scales (figure 6.1a): (i) long range structural order, (ii) closely packed ceramic platelets of dimensions identical to that of nacre, (iii) ceramic bonds (bridges) linking the platelets, (iv) nano-asperities at the surface of platelets, and (v) a secondary phase with lower stiffness ensuring load redistribution, crack deflection, and delamination.

The process we used here is based on ice-templating. However, we do not rely on ice crystals to form the elementary bricks, but instead take advantage of their growth as a driving force for the local self-organization of anisotropic particles (platelets).

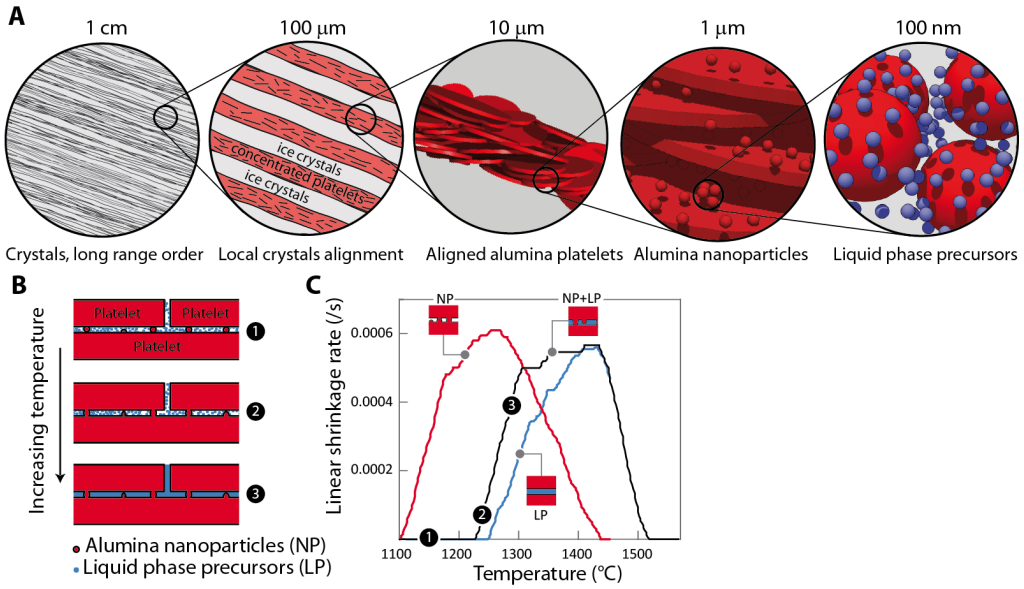

Figure 6.1: **Design strategy describing the control at multiple scale of structural self-organization and the densification strategy**. a) Self-organization of all the structural features occurs during the freezing stage. The growth of ordered-ice crystals triggers the local alignment of platelets. Alumina nanoparticles and liquid phase precursors are entrapped between the platelets. b) Schematic representation of the densification scenario. c) The linear shrinkage rate illustrates that the densification of the composition comprising either one of the building blocks (3 vol.% nanoparticles or 5 vol.% liquid phase) occurs at different temperatures. In the composition comprising all the building blocks, the densification starts earlier, showing an interaction between nanoparticles and liquid phase precursors.

Those particles are the same dimensions as nacre platelets (500 nm thickness, 8 μm diameter) and constitute the elementary building blocks of the structure. When a suspension is directionally frozen, the metastable growth of the ice crystals [195] repels and concentrates the particles present in the suspension. The concentration of the particles occurs at a length-scale where self-organization of platelets can occur [135] (figure 6.1a). Alumina nanoparticles (100 nm) incorporated in the initial suspension serve as a source of both inorganic bridges between the platelets and nanoasperities at the surface of platelets, similar to that observed in nacre. Finally, smaller nanoparticles (20 nm) of liquid phase precursors (silica and calcia) are added to aid filling the remaining gaps during the sintering stage. The material is thus composed of 98.5 vol.% alumina, 1.3 vol.% of silica, and 0.2 vol.% of calcia. This simple strategy, where all the constituents are incorporated in the initial suspension and self-organized in one step, allows precise and facile tailoring of the final material composition. Long range order of the ice crystals is obtained through a freezing under flow method (see Methods 6.2.2). Once the porous samples are obtained, they are simply pressed (to remove the macroporosity) and sintered by field assisted sintering (FAST), a common densification technique. Due to their size and high aspect ratio, the platelets themselves are unlikely to densify by sintering. Instead, the liquid phase formation densifies the structure by rearranging the particles through capillary forces, facilitating platelet packing under the applied load by lubricating the contact points, and by filling the pore space between them (figure 6.1b). At the same time, the nanometric alumina particles form strong bridges by sintering to the platelets because their higher surface area and surface curvature allows them to sinter at lower temperatures than the platelets [199] (figure 6.1c). One important consideration is ensuring that the alumina nanoparticles are not completely dissolved in the liquid phase by either limiting the total amount of liquid phase, or by using short processing times like those employed here (enabled by the rapid, pressure assisted densification method).
The entire process thus consists of just three simple steps:

1. Preparation of an aqueous colloidal suspension containing all the required building blocks and processing additives

2. Ice templating this suspension

3. Pressure assisted sintering at 1500°C.

The materials obtained are referred to as nacre-like alumina.

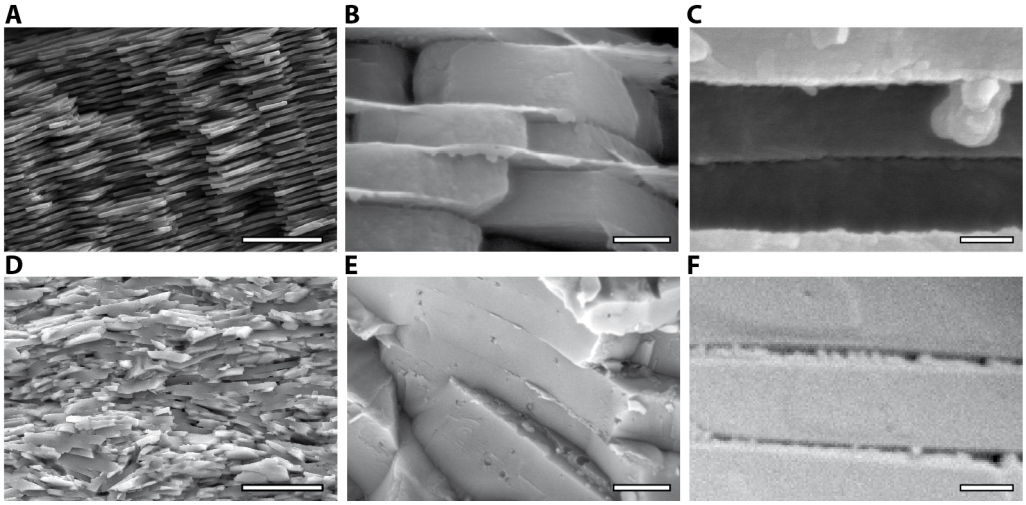

Figure 6.2: **Comparison of the microstructure of nacre a-c) and nacre-like ceramic d-f).** a) and d) SEM micrograph showing the short and long range order of platelets. The nacre-like alumina shows relatively high organization of the platelets. b) and e), Local stacking of platelets. A liquid phase film is present even when the platelets are close, mimicking the protein layer in the nacre structure. c) and f) Closer views of platelets interface unveiling the presence of the inorganic bridges and nano-asperities along with the glassy f) or organic c) phase filling the space between adjacent platelets. Some residual pores are also visible. Scale bars: a), d): 10 μm, b), e): 500 nm, c), f): 250 nm.

6.2.4 Nacre vs. nacre-like alumina microstructure

The final microstructure of the nacre-like alumina (figure 6.2) is characterized by a dense packing of platelets presenting long range order. The use of a fast sintering method limits grain growth so that the initial dimensions of the platelets are retained. A bulk material with submicronic layer spacing is thus obtained, a feature of nacre that had proved impossible to replicate so far in bulk materials. Compared to the microstructure of nacre (figure 6.2, a and b), the packing of platelets presents short range order (figure 6.2e), but the long range order is not as perfect. The waviness of the stacking (figure 6.2d) in our nacre-like ceramic, estimated at pm 15°around the main orientation, comes from the organization of the ice crystals. The long range order is nevertheless sufficient to obtain nearly fully dense samples (e.g., >98% of relative density).

Observations of the interfaces between platelets (figure 6.2, e and f) reveals the presence of a secondary phase mimicking the organic layer in nacre (figure 6.2b), some alumina bridges between adjacent platelets, and nanoasperities analogous to those in nacre (figure 6.2c). Based on the experimental conditions and the ceramic phases in presence, this secondary phase is most likely a glass. A small fraction of the alumina platelets and nanoparticles is dissolved into this glass phase at the interface, so that the actual final fraction of this phase (estimated around 2 to 3 vol.%) is slightly higher than initially incorporated into the suspension (1.5 vol.%). Based on the ternary alumina-silica-calcia phase diagram [200], we can estimate the composition of the glass phase at 10 wt.% SiO2, 65 wt.% CaO, and 25 wt.% Al2O3, although it is hard to tell whether equilibrium is achieved during the rapid densification.

The microstructure of the synthetic material is thus strikingly similar to that of natural nacre at several length scales, validating the possibility to fabricate bulk, centimeter-sized samples with only a few simple processing steps.

6.2.5 Ductile ceramics?

Replicating natural structures like nacre has long been an outstanding challenge. The benefits of such structures on toughness have long been hypothesized [201] although not yet practically demonstrated in bulk materials. All the approaches demonstrated so far are based on the incorporation of a ductile phase (metallic or polymeric). Here we demonstrate a radically different approach to improve toughness, based on brittle constituents. The behavior of the materials tested was compared with a reference polycrystalline alumina sample.

Single-edge notched beam (SENB) tests were carried out to measure the toughness. The resulting stress-strain curves are plotted in figure 6.3a for three model compositions to illustrate the synergistic effects between the structural features introduced: platelets with nano-asperities, platelets with a liquid phase, and platelets with both (the nacre-like alumina structure). As expected, the samples containing the liquid phase only at the platelet interface exhibit a purely linear elastic response until a catastrophic failure occurs, with unstable crack propagation characteristic of brittle materials. The corresponding fracture surface, showing no crack deflection at all, is shown in figure 6.3d.

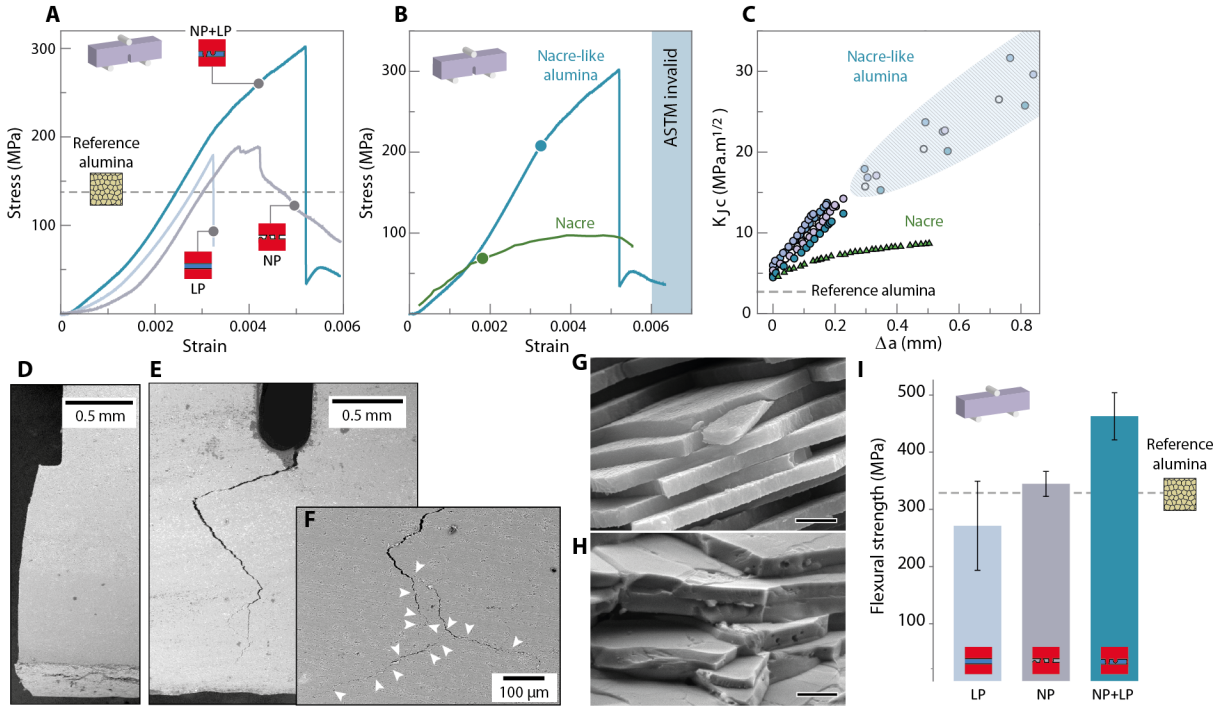

Figure 6.3: **Mechanical properties and toughness measurement of nacre-like ceramic and nacre.** a) Stress strain curve of the same three compositions on SENB samples. The 5 vol.% liquid phase presents brittle behavior, the 3 vol.% nanoparticles presents toughening and the combination leads to a very important toughening. b) Stress strain curve for SENB samples of the nacre-like ceramic and natural nacre. The dots on the curve indicate the onset of non-linearity. c) Fracture toughness K_J calculated from J-integral and crack extension Δa and the equivalent for the nacre-like ceramic and nacre. The hatched area represents the second crack event. d) Smooth fracture surface of brittle composition (platelets and liquid phase). e) Fracture surface of a nacre-like sample that shows the long range crack deflection. f) Multiple cracking and crack bridging towards the end of the crack path. Arrows indicate the onset of crack branching and bridging (g and h) Detail of the fracture surface in nacre g) and nacre-like alumina h) showing the crack deflection and delamination at the platelets interface. Scale bar: 1 µm. i) Flexural strength of three different compositions, liquid phase (5 vol.%) an platelets, nanoparticles (3 vol.%) and platelets, and nacre like alumina (respectively 1.5 vol.% and 3 vol.% of liquid phase and nanoparticles). The dot line corresponds to an equiaxed fine grain alumina on the a) and i) plots. Error bars indicate standard deviation.

The fracture toughness K_{IC} is nevertheless already significantly higher than a reference alumina, with respective values of 4.9 MPa$\sqrt{\text{m}}$ and 3.8 MPa$\sqrt{\text{m}}$, since platelets are significantly harder to separate than isotropic particles due to their orientations [202]. Platelets with nano-asperities exhibit a behavior characteristic of unstable crack growth with a significant crack deflection, although only a limited toughening is measured.

When both reinforcements are combined, leading to the nacre-like alumina structure, we obtain stable crack growth combined with toughening, similar to that of nacre (reported for comparison in figure 6.3b). The nacre-like alumina, free of any ductile component, is clearly stiffer. The mechanical response, where 40% of the strain to failure is inelastic, is strikingly reminiscent of that observed in ductile metallic or organic materials, a remarkable and unexpected behavior for what is a wholly ceramic material (98.5 vol.% alumina and 1.5 vol.% silica and calcia). The reinforcement mechanisms (discussed in the next section) are extrinsic, which means that of course no true ductility (plastic deformation without crack propagation) can be achieved.

The crack is deflected by the composite low stiffness interface [75] (figure 6.3e) and slowed down by various extrinsic toughening mechanisms which result in stable crack growth, similar to natural nacre [70]. Unstable propagation occurs when the crack length exceeds 200 µm. The crack is eventually arrested again by different toughening mechanisms like multiple cracking, crack bridging (figure 6.3f), delamination, and frictional sliding of the platelets.

The fracture toughness K_{IC} describes only the resistance to a crack initiation. It is nevertheless unable to describe the multiple extrinsic toughening mechanisms that take place during crack propagation and greatly contributes to the dissipation of energy. This toughening leads to an increase of the fracture resistance as the crack propagates. This behavior, known as an R-curve effect, is characteristic of many natural materials such as nacre [70], bone [67, 68], and tooth [203]. In order to measure the R-curve, the indirect crack length is measured by a compliance method (see 6.2.2). By taking into account the local deflection as well as the other dissipation mechanisms with J-integral and using the equivalence in stress intensity factor, the maximum increase of toughness (referred to as short crack toughness) is already extremely high, around 15 MPa$\sqrt{\text{m}}$. This corresponds to a 300% increase compared to the K_{IC} toughness (400% increase with respect to the reference alumina). This value is probably the highest reported for a purely ceramic material which does not present intrinsic toughening [a].

[a] Transformation toughening in zirconia [204] is the only intrinsic toughening mechanism in ceramic materials.

The second stage of crack growth is unstable. Nevertheless, different toughening mechanisms are present, such as multiple crack deflection and crack branching (figure 6.3, e and f), eventually leading to the arrest of cracks before catastrophic failure can occur. Samples are not fully broken after being exposed to their maximum stresses, an attestation to the efficiency of the toughening mechanisms in these materials. Estimating this contribution to the overall toughness should be done carefully, as validity of the assumptions can be questioned. According to the ASTM criterion [205], the maximum crack extension is given by $\Delta a_{max} = 0.25b$ (b being the uncracked ligament width), which corresponds in our results to $\Delta a = 0.4mm$.

However, toughness measurements can be considered valid until the data becomes geometry dependent due to large scale bridging [190], which here corresponds to $\Delta a = 0.8mm$. We adopt a more conservative approach and consider a limit more representative of our material, corresponding to the crack extension where the first instability occurs, around 200 µm. We consider that the toughness values above this threshold, referred to as the long crack toughness, are only indicative, and used here only to reflect the multiple toughening mechanisms that take place during the second stage of crack propagation. The calculated values are plotted in figure 6.3c. Analogous approaches have been used previously in similar structures [62, 67, 194] where multiple extrinsic toughening mechanisms needed to be described. Reaching a value of more than 30 MPa$\sqrt{\text{m}}$, the toughness of our nacre-like alumina far exceeds that of nacre, and is equivalent to the best brick and mortar polymer/ceramic composites developed previously [194], an unprecedented value for a purely ceramic material or even for a ceramic composite.

6.2.6 Toughening mechanisms

The measured toughness is much greater than one could expect from a rule of mixture of the individual constituents. We combine here a number of toughening mechanisms, operating at different length scales. By restricting our choice of constituents to ceramic materials to ensure their potential use at high temperature and maximize the stiffness, we are also eliminating most of the usual toughening mechanisms seen in ductile materials such as dislocation plasticity, shear bands, or ductility. The extrinsic toughening mechanisms developed here are derived from the hierarchical, multilayered architecture of the material and the load redistribution resulting from the brick and mortar architecture. Multiple cracking, crack bridging (figure 6.3f), and delamination (figure 6.3h) operate at the crack tip, effectively relieving the locally high stresses. The alumina nanoparticles provide both bridges between the platelets and nano-asperities, with lead to a very efficient energy dissipation by fric-

tional sliding during platelets pull-out and breaking of the bridges. Pores located between adjacent platelets, as seen in figure 6.2c, may also contribute by acting as local crack arresters by a Cook-Gordon mechanism [206].

The possibility to achieve toughness through a proper combination of brittle constituents has been recently hypothesized [207]. With the proper topological arrangement and stiffness ratio between two brittle phases, the stress concentration around the crack tip can be reduced thanks to a more efficient load redistribution. The deformation is delocalized and strain redistributes throughout the entire structure. These mechanisms are likely to contribute to the level of toughness achieved in these structures. Further work will be necessary to quantify the relative contributions of all the toughening mechanisms identified here.

6.2.7 Breaking free from the strength-toughness compromise

The flexural strengths of our materials are reported in figure 6.3i. Platelets combined with either the liquid phase or the nano-asperities alone have, as expected, a flexural strength equivalent to or lower than the reference alumina. The nacre-like alumina, comprising both the liquid phase and the nano-asperities, exhibits a 470 MPa flexural strength, a value that largely exceeds that of the reference alumina. The synergistic combination of both the liquid phase and the nano-asperities is thus strikingly demonstrated by these measurements.

Strength and toughness are generally considered to be mutually exclusive [62]. Because intrinsic toughening mechanisms are linked to plasticity and thus strength, a compromise is always reached in structural materials where either one of the properties is sacrificed. All the previous attempts to increase the toughness of ceramics are based on the introduction of a ductile phase, which can be a polymer, a metal phase, or carbon reinforcements such as graphene or carbon nanotubes. In similar work [194] for instance, the introduction of 20 vol.% of a polymeric phase to increase the toughness resulted in a notable decrease of the flexural strength. Further toughness increases can be achieved through the addition of up to 60 vol.% Al-Si alloy [64], but no appreciable gains in strength are obtained. The introduction of a polymer or a metallic phase is thus always done at the expense of strength, stiffness and useful temperature range. The toughness of the nacre-like alumina is far greater than other reported values for alumina [219], textured alumina [180], or even for alumina composites [220], composed of either an organic phase [194], a metallic phase [208, 209, 210, 211, 212], or carbon reinforcements such as carbon nanotubes [214, 215, 216] or graphene [213] (figure 6.4a). As in nacre, the organization of the microstructure induces the emergence of improved properties without

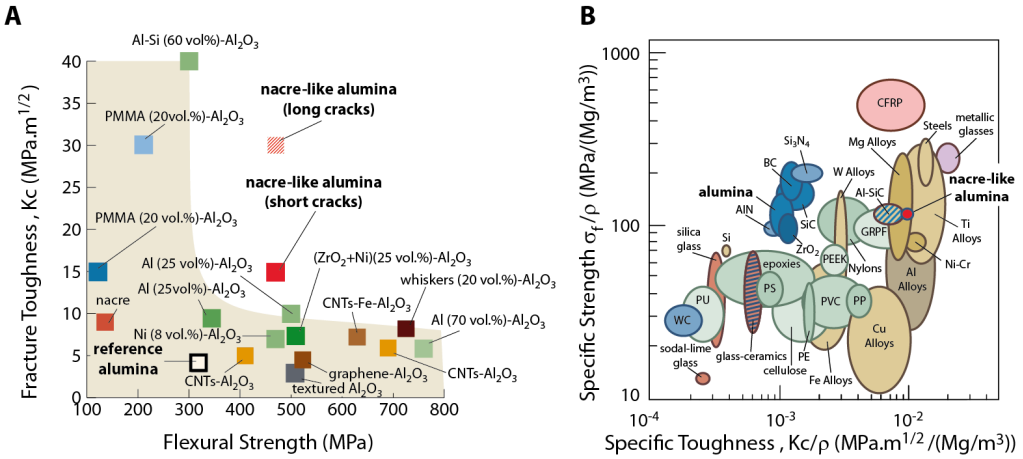

Figure 6.4: **Comparison of the relative materials performance.** a) The conflict between strength and toughness: fracture toughness vs. flexural strength, for alumina based materials. Improvements in toughness are obtained by the introduction of a ductile phase, such as a metallic phase [64, 208, 209, 210, 211, 212], a polymer [194], or carbon reinforcements such as graphene [213], carbon nanotubes [214, 215, 216], or whiskers [217]. Improvements in strength are achieved through a texturation of the grains [180] or the addition of strong reinforcements. b) Ashby diagram of specific strength versus specific toughness for a range of engineering and natural materials [218]. The nacre-like alumina's have specific strength/toughness properties similar to that of titanium or magnesium metallic alloys.

compromise.

When it comes to materials choice, in particular for structural applications, the density is a major consideration. Metallic glasses are some of the toughest engineered materials produce, but their high density, twice that of titanium, limits their use. Thickness is also a major problem because the cooling rates necessary cannot always be achieved on bulk samples. The unique combination of specific strength (σ_f/ρ) and specific toughness (K_c/ρ) of our bioinspired ceramic material actually matches that of engineering aluminum and magnesium alloys (figure 6.4b) while exhibiting a higher hardness, stiffness, and operating temperature. Because only ceramic constituents are used, the stiffness and the strength of our material are at the usual level of engineering, technical ceramics, highlighting their remarkable potential in structural and energy-related applications.

6.3 Concluding remarks

The possibility to achieve toughness based on the proper topological arrangement of brittle constituents proves the remarkable potential of the approach shown here in the development of strong and tough materials. The bioinspired design presented here is material-independent, and can therefore guide future endeavors to the development of strong, tough, and stiff materials, in great need for structural, transportations, and energy-related applications where catastrophic failure is not an option. The flexibility in the choice of materials permits an independent assessment of the role of each structural feature on the mechanical properties, which is not possible in natural materials. Beyond structural materials, we expect to see many other benefits of using ice crystals as a driving force for the bulk self-organization of elementary building blocks. We are now focused on assessing the high temperature mechanical properties of these materials and extending the concepts demonstrated here to other materials combinations.

Conclusions and outlooks

Conclusions

This work was carried out at the LSFC/Saint-Gobain CREE and the MATEIS laboratory under the supervision of Sylvain Deville and Eric Maire.

The primary objective of this research was to study the alignment of micrometric platelet particles by ice-templating. This technique, which can be considered as a self-assembly process, allows the processing of macroporous samples with a directional porosity. The underlying phenomenon is the segregation of a suspension's constituents by the growth of solvent crystals. This concentration occurs at the micronic scale and is the driving force of the self-assembly. We have studied the organization of boron nitride and alumina platelets in various compositions. A discrete element model was built to unravel the mechanisms defining the characteristics of the final structures. The rest of the manuscript exposed the control over the material's architecture, each chapter corresponding to an increase in complexity:

1. control of the local orientation of platelets in macroporous solids
2. control of the long range order of crystals (and walls)
3. control of the interfaces between the building blocks

Ice-templating and self-assembly

In the first chapter, the different self-assembly processes are described, along with their drawbacks and assets. Multiple strategies exist to organize building blocks, depending on their sizes and/or functions, but the resulting samples are mainly two dimensional, large three dimensional systems being extremely hard to control. The main asset of using ice-templating is the capacity to act on small scale, the concentration between two ice crystals occurring at micronic scale, while the final sample may reach the size a few cubic centimeters. The process seems compatible

with a variety of elementary blocks (molecules, colloids...) used so far, but the underlying mechanisms were not explained yet.

Ice-templating was previously known for its capacity, among other uses, to process bioinspired materials. However, plenty of room was available to improve the concept, such as the use of smaller building blocks to multiply interfaces, the use of mineral materials only or the simplification of the process.

How platelets get aligned

The development of a discrete element model provides us with a direct insight into the dynamic organization of the platelets during the process. The presence of different architectures, first observed in SEM pictures, was confirmed by both holotomography experiments and the model results. The compaction that occurs between two adjacent crystals align the particles and is a delicate balance between pushing and engulfment at the interface. Above a certain number (dependent on the material), the particles in direct contact with the solidification front are aligned and pushed. As the concentration increases, particles in the core are not free to move anymore and are jammed in a disordered state. Avoiding this state requires either to reduce the number of particles or to increase the interface velocity, which dynamically dilutes the system.

A phase diagram that separate the domain where the platelets were partially aligned, fully aligned or jammed was established using the model. The benefit of particle alignment was illustrated through the investigation of the thermal properties of boron nitride/silicon rubber composites. The thermal diffusivities on ice templated sample were improved by 200% compared to a sample presenting the same amount of randomly oriented platelets.

Putting the alignment of platelets to good use

Ice-templating can concentrate and align platelets to obtain orthotrope composites. This microstructure is highly efficient for thermal transfer compare to material produced by other methods, such as electric or high intensity magnetic field. Even though, the behavior remains dictated by the resistance of the interfaces, as the modeling of the response suggests.

The use of platelets is not only interesting for functional properties, but also for mechanical properties. When aligned by ice-templating, such particles provide a scaffold that combines thin walls (around 5 μm) and large pores (> 30 μm). This combination is nearly impossible to achieve with isotropic particles because of tilted ice growth at low cooling rates. Once consolidated by liquid phase sintering, the

resulting cellular materials exhibit not only an architecture similar to that of wood but their specific mechanical properties are also close.

Through these two examples, we have proven that the alignment of particles is indeed beneficial for functional and structural properties. The control over the alignment of both particles and walls can nevertheless be enhanced, to further improve the mechanical or functional properties.

Long range order control of ice crystals orientation

A novel technique, named freezing under flow, was developed in order to align the ice crystals over large dimensions. The addition of a second thermal gradient during the freezing allows to control the growth in two directions simultaneously. This additional gradient is created by letting the suspension flow continuously on the cooling stage. The sample obtained by this method with a long range order over several centimeters. The orientation distribution of the walls was measured by image analysis on X-ray computed tomography data and the associated full width at half maximum was 34°.

The orientation distribution of the particles aligned by ice-templating is in the same order of magnitude (FWHM of 30°) which may be too broad for certain functional properties. We used Templated grain growth (TGG) to decrease this misalignment. This method is based on the growth of large particles at the expense of smaller ones to obtain dense and textured polycrystalline ceramics. By combining TGG with ice-templating, we obtained porous alumina samples with large and aligned grains.

We combined the TGG and freezing under flow methods to produce porous sodium potassium niobate (KNN) piezoceramics. The final material consisted in a layered ceramic presenting large cubic grains oriented perpendicular to the pore direction. Even if a preferred orientation was measured by XRD, it was low compared to typical texture in dense ceramics made by TGG. A model was developed to simulate the variation of the composite orientation distribution. The wall misalignment is the main broadening factor in the composite response.

Nacre-like alumina: controlling the interface is the key

The final goal of this work was to create a dense ceramic that presents aligned platelets and controlled interfaces. The particles were pre-aligned by ice templating and the porous material was then compacted. To obtain a dense material, the walls needed to be as parallel as possible to minimize the presence of stacking defects of the particles after the compaction. We added another level of hierarchy by modifying the interfaces between the platelets with different additives, to mimic the structure

of nacre. The organic layer and the bridges between adjacent platelets in nacre were reproduced by a glassy phase formed at high temperature and by alumina nanoparticles.

The combination of the three levels of hierarchy in the architecture led to a microstructure similar to nacre. The mechanical properties were highly dependent of the composition of the interface between the platelets. The behavior during crack propagation tests ranged from catastrophic failure to a slow crack growth with toughening when the amount of glassy phase and nanoparticles was reduced (down to 1.5 and 3 vol% respectively). The improvement of the resistance to crack propagation [b] increased from 6 MPa$\sqrt{\text{m}}$ to 15 MPa$\sqrt{\text{m}}$ for short crack length (<200 µm). This value even reached 30 MPa$\sqrt{\text{m}}$ for longer cracks which makes this material probably the toughest ceramics (alumina?) ever synthesized. The main mechanisms responsible for the reinforcement are crack deflections and crack bridging at the interfaces for short crack length, in addition to crack branching and micro-cracking for long crack length.

The flexural strength was also dependent on the composition, the most brittle one possessed a strength of 280 MPa but the toughest one broke at a stress of 480 MPa. Again, because we choose only mineral constituents, the material strength is high, and the tougher it is the stronger it gets.

Perspectives

During these past three years, we have tried to cover as many aspects of the platelets self-assembly by ice templating as we could, from basic understanding to the creation of hierarchical materials. But (fortunately) many others aspects of this work can be (and will be) pursued.

As detailed in the first chapter, ice-templating is a promising tool to induce self-assembly of elementary blocks. This research has used only platelet-shaped particles to reach the final goal of mimicking nacre structure. But several other materials could be used. For instance colloidal crystals of large dimensions can theoretically be built, with gradually changing optical properties depending on the freezing conditions.

For this type of problematic, the discrete element model may prove useful to determine under which conditions self-assembly may occur. The model developed here does not take into account the solidification of water and thus ignore the impact of the impurities (particles, soluble species. . .) on the crystals morphology. But despite

[b] Traduced here in terms of stress intensity factor K_{JC}

this intrinsic limitation, it may be applied to a variety of compositions, to predict their arrangement as a function of the freezing conditions. This may be an important tool to develop functional materials where the organization of the particles need to be carefully controlled.

The porous materials containing aligned platelets have proven readily efficient for some applications, such as thermal management materials, and can be extended to electrical conductivity for instance. Regarding the mechanical properties, the possibility to adjust the wall porosity to change the fracture behavior of the entire material have merely been introduced. If this type of behavior can be observed with a higher solid loading, then the strength of the sample could be improved while keeping it crushable, thus avoiding critical failure. Furthermore, the fracture behavior of porous bodies is not fully understood yet, and this type of structures could facilitate the comprehension of the effect of porosity.

Developing functional 2-2 composites has been and it still a challenge. Because the growth of crystals has to be controlled, complexity in the process and randomness in the results are expected. An effective solution has been developed, the 'freezing under flow', and it is robust enough to repeatedly produce homogeneous samples with a long range structural order. However, the main limitation of this approach is the broad distribution in orientation, as testified by the final texture of the piezoceramic developed. Narrowing this distribution might be done by changing process conditions, but it remains hazardous to predict the extent of the improvement. To get a robust grasp on the final ice crystals arrangement, a control of the nucleation must probably be introduced.

Finally, the nacre-like alumina possess remarkable mechanical properties. Now that we have at our disposal a robust process and design guidelines, the concept can be improved and extended to other classes of materials. Keeping fully ceramic design and changing the composition could further improve the properties, especially the thermal stability. But changing the nature of the second phase may reveal the true potential of these materials. Adding for instance carbon (similarly to existing ceramic composites) could add some ductility at the interfaces while retaining the thermal resistance. Nearly every part of this material can be tuned independently so the toughening mechanisms can be adapted and improved.

Personally, I cannot wait to see the materials that will be developed using all these tools.

Bibliography

[1] S. Deville, E. Saiz, R. K. Nalla, and A. P. Tomsia, "Freezing as a path to build complex composites.," *Science*, vol. 311, pp. 515–8, Jan. 2006.

[2] G. M. Whitesides and B. Grzybowski, "Self-assembly at all scales.," *Science*, vol. 295, pp. 2418–21, Mar. 2002.

[3] G. Desiraju, *Crystal Engineering: The Design of Organic Solids*. Elsevier Science, 1989.

[4] S. Jakubith, H. Rotermund, W. Engel, A. von Oertzen, and G. Ertl, "Spatiotemporal concentration patterns in a surface reaction: Propagating and standing waves, rotating spirals, and turbulence," *Physical Review Letters*, vol. 65, pp. 3013–3016, Dec. 1990.

[5] W. L. Noorduin, A. Grinthal, L. Mahadevan, and J. Aizenberg, "Rationally Designed Complex, Hierarchical Microarchitectures," *Science*, vol. 340, pp. 832–837, May 2013.

[6] M. J. Garay, R. Davies, C. Averill, and J. a. Westphal, "Actinoform Clouds: Overlooked Examples of Cloud Self-Organization at the Mesoscale," *Bulletin of the American Meteorological Society*, vol. 85, pp. 1585–1594, Oct. 2004.

[7] G. J. D. a. a. Soler-Illia, C. Sanchez, B. Lebeau, and J. Patarin, "Chemical strategies to design textured materials: from microporous and mesoporous oxides to nanonetworks and hierarchical structures.," *Chemical reviews*, vol. 102, pp. 4093–138, Nov. 2002.

[8] S. Förster and M. Antonietti, "Amphiphilic Block Copolymers in Structure-Controlled Nanomaterial Hybrids," *Advanced Materials*, vol. 10, pp. 195–217, Feb. 1998.

[9] J. N. Israelachvili, D. J. Mitchell, and B. W. Ninham, "Theory of self-assembly of hydrocarbon amphiphiles into micelles and bilayers," *Journal of the Chemical Society, Faraday Transactions 2*, vol. 72, p. 1525, 1976.

[10] G. Riess, "Micellization of block copolymers," *Progress in Polymer Science*, vol. 28, pp. 1107–1170, July 2003.

[11] J. J. Hwang, S. N. Iyer, L.-S. Li, R. Claussen, D. a. Harrington, and S. I. Stupp, "Self-assembling biomaterials: liquid crystal phases of cholesteryl oligo(L-lactic acid) and their interactions with cells.," *Proceedings of the National Academy of Sciences of the United States of America*, vol. 99, pp. 9662–7, July 2002.

[12] T. Aida, E. W. Meijer, and S. I. Stupp, "Functional supramolecular polymers.," *Science*, vol. 335, pp. 813–7, Feb. 2012.

[13] O. Ikkala and G. ten Brinke, "Functional materials based on self-assembly of polymeric supramolecules.," *Science*, vol. 295, pp. 2407–9, Mar. 2002.

[14] C. G. Hardy and C. Tang, "Advances in square arrays through self-assembly and directed self-assembly of block copolymers," *Journal of Polymer Science Part B: Polymer Physics*, vol. 51, pp. 2–15, Jan. 2013.

[15] A. Taguchi and F. Schüth, *Ordered mesoporous materials in catalysis*, vol. 77. Jan. 2005.

[16] Y. Ren, L. J. Hardwick, and P. G. Bruce, "Lithium intercalation into mesoporous anatase with an ordered 3D pore structure.," *Angewandte Chemie*, vol. 49, pp. 2570–4, Mar. 2010.

[17] W. C. K. Poon, "Colloids as big atoms.," *Science*, vol. 304, pp. 830–1, May 2004.

[18] C. P. Royall, W. C. K. Poon, and E. R. Weeks, "In search of colloidal hard spheres," *Soft Matter*, vol. 9, no. 1, p. 17, 2013.

[19] W. C. K. Poon, "The physics of a model colloid-polymer mixture," *Journal of Physics: Condensed Matter*, vol. 14, 2002.

[20] W. C. K. Poon, "Phase separation, aggregation and gelation in colloid-polymer mixtures and related systems," *Current Opinion in Colloid & Interface Science*, vol. 3, pp. 593–599, Dec. 1998.

[21] Y. Xia, B. Gates, Y. Yin, and Y. Lu, "Monodispersed Colloidal Spheres: Old Materials with New Applications," *Advanced Materials*, vol. 12, pp. 693–713, May 2000.

[22] J. Henzie, M. Grünwald, A. Widmer-Cooper, P. L. Geissler, and P. Yang, "Self-assembly of uniform polyhedral silver nanocrystals into densest packings and exotic superlattices.," *Nature materials*, vol. 11, pp. 131–7, Feb. 2012.

[23] K. Miszta, J. de Graaf, G. Bertoni, D. Dorfs, R. Brescia, S. Marras, L. Ceseracciu, R. Cingolani, R. van Roij, M. Dijkstra, and L. Manna, "Hierarchical self-assembly of suspended branched colloidal nanocrystals into superlattice structures.," *Nature materials*, vol. 10, pp. 872–6, Nov. 2011.

[24] A. Yethiraj and A. van Blaaderen, "A colloidal model system with an interaction tunable from hard sphere to soft and dipolar.," *Nature*, vol. 421, pp. 513–7, Jan. 2003.

[25] T. Palberg, "Crystallization kinetics of repulsive colloidal spheres," *Journal of Physics: Condensed Matter*, vol. 11, pp. R323–R360, July 1999.

[26] E. Sirota, H. Ou-Yang, S. Sinha, P. Chaikin, J. Axe, and Y. Fujii, "Complete phase diagram of a charged colloidal system: A synchrotron x-ray scattering study," *Physical Review Letters*, vol. 62, pp. 1524–1527, Mar. 1989.

[27] M. E. Leunissen, C. G. Christova, A.-P. Hynninen, C. P. Royall, A. I. Campbell, A. Imhof, M. Dijkstra, R. van Roij, and A. van Blaaderen, "Ionic colloidal crystals of oppositely charged particles.," *Nature*, vol. 437, pp. 235–40, Sept. 2005.

[28] Y. Wang, Y. Wang, D. R. Breed, V. N. Manoharan, L. Feng, A. D. Hollingsworth, M. Weck, and D. J. Pine, "Colloids with valence and specific directional bonding," *Nature*, vol. 490, no. 7422, pp. 51–55, 2012.

[29] A. Stein and R. Schroden, "Colloidal crystal templating of three-dimensionally ordered macroporous solids: materials for photonics and beyond," *Current Opinion in Solid State and Materials . . .* , vol. 5, no. 2001, pp. 553–564, 2001.

[30] A. Stein and R. C. Schroden, "Colloidal crystal templating of three-dimensionally ordered macroporous solids: materials for photonics and beyond," *Current Opinion in Solid State and Materials Science*, vol. 5, pp. 553–564, Dec. 2001.

[31] A. van Blaaderen, R. Ruel, and P. Wiltzius, "Template-directed colloidal crystallization," *Nature*, vol. 385, pp. 321–324, Jan. 1997.

[32] E. Kumacheva, R. Golding, M. Allard, and E. Sargent, "Colloid Crystal Growth on Mesoscopically Patterned Surfaces: Effect of Confinement," *Advanced Materials*, vol. 14, pp. 221–224, Feb. 2002.

[33] P. Schall, I. Cohen, D. a. Weitz, and F. Spaepen, "Visualization of dislocation dynamics in colloidal crystals.," *Science*, vol. 305, pp. 1944–8, Sept. 2004.

[34] O. Paris, G. Fritz-Popovski, D. Van Opdenbosch, and C. Zollfrank, "Recent Progress in the Replication of Hierarchical Biological Tissues," *Advanced Functional Materials*, pp. n/a–n/a, June 2013.

[35] A. Stein, F. Li, and N. R. Denny, "Morphological Control in Colloidal Crystal Templating of Inverse Opals, Hierarchical Structures, and Shaped Particles," *Chemistry of Materials*, vol. 20, pp. 649–666, Feb. 2008.

[36] J.-P. Dacquin, J. Dhainaut, D. Duprez, S. Royer, A. F. Lee, and K. Wilson, "An efficient route to highly organized, tunable macroporous-mesoporous alumina.," *Journal of the American Chemical Society*, vol. 131, pp. 12896–7, Sept. 2009.

[37] K. H. Nagamanasa, S. Gokhale, R. Ganapathy, and a. K. Sood, "Confined glassy dynamics at grain boundaries in colloidal crystals.," *Proceedings of the National Academy of Sciences of the United States of America*, vol. 108, pp. 11323–6, July 2011.

[38] Y. Sakka, T. S. Suzuki, and T. Uchikoshi, "Fabrication and some properties of textured alumina-related compounds by colloidal processing in high-magnetic field and sintering," *Journal of the European Ceramic Society*, vol. 28, pp. 935–942, Jan. 2008.

[39] H.-B. Cho, Y. Tokoi, S. Tanaka, T. Suzuki, W. Jiang, H. Suematsu, K. Niihara, and T. Nakayama, "Facile orientation of unmodified BN nanosheets in polysiloxane/BN composite films using a high magnetic field," *Journal of Materials Science*, vol. 46, pp. 2318–2323, Nov. 2010.

[40] Y. Sahoo, M. Cheon, S. Wang, H. Luo, E. P. Furlani, and P. N. Prasad, "Field-Directed Self-Assembly of Magnetic Nanoparticles," *The Journal of Physical Chemistry B*, vol. 108, pp. 3380–3383, Mar. 2004.

[41] J. Legrand, A. T. Ngo, C. Petit, and M.-P. Pileni, "Domain Shapes and Superlattices Made of Cobalt Nanocrystals," *Advanced Materials*, vol. 13, pp. 58–62, Jan. 2001.

[42] S. Samouhos and G. McKinley, "Carbon Nanotube–Magnetite Composites, With Applications to Developing Unique Magnetorheological Fluids," *Journal of Fluids Engineering*, vol. 129, no. 4, p. 429, 2007.

[43] A. a. Shah, H. Kang, K. L. Kohlstedt, K. H. Ahn, S. C. Glotzer, C. W. Monroe, and M. J. Solomon, "Liquid Crystal Order in Colloidal Suspensions of Spheroidal Particles by Direct Current Electric Field Assembly.," *Small*, pp. 1–12, Mar. 2012.

[44] H.-B. Cho, T. Nakayama, T. Suzuki, S. Tanaka, W. Jiang, H. Suematsu, and K. Niihara, "Linear Assembles of BN Nanosheets, Fabricated in Polymer/BN Nanosheet Composite Film," *Journal of Nanomaterials*, vol. 2011, pp. 1–7, 2011.

[45] T. Fujihara, H.-B. Cho, T. Nakayama, T. Suzuki, W. Jiang, H. Suematsu, H. D. Kim, and K. Niihara, "Field-Induced Orientation of Hexagonal Boron Nitride Nanosheets Using Microscopic Mold for Thermal Interface Materials," *Journal of the American Ceramic Society*, vol. 5, pp. 1–5, Nov. 2011.

[46] A. Ahniyaz, Y. Sakamoto, and L. Bergström, "Magnetic field-induced assembly of oriented superlattices from maghemite nanocubes.," *Proceedings of the National Academy of Sciences of the United States of America*, vol. 104, pp. 17570–4, Nov. 2007.

[47] R. M. Erb, R. Libanori, N. Rothfuchs, and A. R. Studart, "Composites Reinforced in Three Dimensions by Using Low Magnetic Fields," *Science*, vol. 335, pp. 199–204, Jan. 2012.

[48] J. Chatterjee, Y. Haik, and C.-J. Chen, "Size dependent magnetic properties of iron oxide nanoparticles," *Journal of Magnetism and Magnetic Materials*, vol. 257, pp. 113–118, Feb. 2003.

[49] L. J. Bonderer, A. R. Studart, and L. J. Gauckler, "Bioinspired design and assembly of platelet reinforced polymer films.," *Science*, vol. 319, pp. 1069–73, Feb. 2008.

[50] Z. Tang, N. a. Kotov, S. Magonov, and B. Ozturk, "Nanostructured artificial nacre.," *Nature materials*, vol. 2, pp. 413–8, June 2003.

[51] P. Das, S. Schipmann, J.-M. Malho, B. Zhu, U. Klemradt, and A. Walther, "Facile access to large-scale, self-assembled, nacre-inspired high-performance materials with tunable nanoscale periodicities.," *ACS applied materials & interfaces*, Mar. 2013.

[52] P. Podsiadlo, A. K. Kaushik, E. M. Arruda, A. M. Waas, B. S. Shim, J. Xu, H. Nandivada, B. G. Pumplin, J. Lahann, A. Ramamoorthy, and N. A. Kotov, "Ultrastrong and Stiff Layered Polymer Nanocomposites," *Science*, vol. 318, pp. 80–83, Oct. 2007.

[53] T. Kimura, "Preparation of crystallographically textured Bi0.5Na0.5TiO3BaTiO3 ceramics by reactive-templated grain growth method," *Ceramics International*, vol. 30, no. 7, pp. 1161–1167, 2004.

[54] H. Watanabe, T. Kimura, and T. Yamaguchi, "Particle Orientation During Tape Casting in the Fabrication of Grain-Oriented Bismuth Titanate," *Journal of the American Ceramic Society*, vol. 72, pp. 289–293, Feb. 1989.

[55] A. Karnis, H. Goldsmith, and S. Mason, "The kinetics of flowing dispersions," *Journal of Colloid and Interface Science*, vol. 22, pp. 531–553, Dec. 1966.

[56] M. M. Seabaugh, I. H. Kerscht, and G. L. Messing, "Texture Development by Templated Grain Growth in Liquid Phase Sintered alpha-Alumina," *Journal of American Ceramic Society*, vol. 80, no. 5, pp. 1181–1188, 1997.

[57] J. A. Horn, S. C. Zhang, U. Selvaraj, G. L. Messing, and S. Trolier-McKinstry, "Templated Grain Growth of Textured Bismuth Titanate," *Journal of the American Ceramic Society*, vol. 82, pp. 921–926, Apr. 1999.

[58] K. M. Nam, Y. J. Lee, W. T. Kwon, S. R. Kim, H. M. Lim, H. Kim, Y. Kim, and O. Pmma, "Preparation of Al2O3 Platelet / PMMA Composite and Its Mechanical / Thermal Characterization," *Journal of the Korean Ceramic Society*, vol. 49, no. 5, pp. 438–441, 2012.

[59] R. Libanori, R. M. Erb, A. Reiser, H. Le Ferrand, M. J. Süess, R. Spolenak, and A. R. Studart, "Stretchable heterogeneous composites with extreme mechanical gradients.," *Nature communications*, vol. 3, p. 1265, Jan. 2012.

[60] H. D. Espinosa, J. E. Rim, F. Barthelat, and M. J. Buehler, "Merger of structure and material in nacre and bone – Perspectives on de novo biomimetic materials," *Progress in Materials Science*, vol. 54, pp. 1059–1100, Nov. 2009.

[61] C. Sanchez, H. Arribart, and M. M. G. Guille, "Biomimetism and bioinspiration as tools for the design of innovative materials and systems.," *Nature materials*, vol. 4, pp. 277–88, Apr. 2005.

[62] R. O. Ritchie, "The conflicts between strength and toughness.," *Nature materials*, vol. 10, pp. 817–22, Nov. 2011.

[63] K. Liu and L. Jiang, "Bio-inspired design of multiscale structures for function integration," *Nano Today*, vol. 6, pp. 155–175, Apr. 2011.

[64] M. E. Launey, M. J. Buehler, and R. O. Ritchie, "On the Mechanistic Origins of Toughness in Bone," *Annual Review of Materials Research*, vol. 40, pp. 25–53, June 2010.

[65] R. Rabiei, S. Bekah, and F. Barthelat, "Failure mode transition in nacre and bone-like materials.," *Acta biomaterialia*, vol. 6, pp. 4081–9, Oct. 2010.

[66] F. Heinemann, M. Launspach, K. Gries, and M. Fritz, "Gastropod nacre: structure, properties and growth–biological, chemical and physical basics.," *Biophysical chemistry*, vol. 153, pp. 126–53, Jan. 2011.

[67] K. J. Koester, J. W. Ager, and R. O. Ritchie, "The true toughness of human cortical bone measured with realistically short cracks.," *Nature materials*, vol. 7, pp. 672–7, Aug. 2008.

[68] H. Peterlik, P. Roschger, K. Klaushofer, and P. Fratzl, "From brittle to ductile fracture of bone.," *Nature materials*, vol. 5, pp. 52–55, Jan. 2006.

[69] R. D. Rao, S. Tang, C. Lim, and N. Yoganandan, "Developmental morphology and ossification patterns of the c1 vertebra.," *The Journal of bone and joint surgery. American volume*, vol. 95, pp. e1241–7, Sept. 2013.

[70] F. Barthelat and R. Rabiei, "Toughness amplification in natural composites," *Journal of the Mechanics and Physics of Solids*, vol. 59, pp. 829–840, Apr. 2011.

[71] F. Barthelat, H. Tang, P. Zavattieri, C. Li, and H. Espinosa, "On the mechanics of mother-of-pearl: A key feature in the material hierarchical structure," *Journal of the Mechanics and Physics of Solids*, vol. 55, pp. 306–337, Feb. 2007.

[72] F. Song, X. H. Zhang, and Y. L. Bai, "Microstructure in a biointerface," *Journal of Materials Science Letters*, vol. 21, pp. 639–641, 2002.

[73] F. Song, A. Soh, and Y. Bai, "Structural and mechanical properties of the organic matrix layers of nacre," *Biomaterials*, vol. 24, pp. 3623–3631, Sept. 2003.

[74] J. Aizenberg, J. C. Weaver, M. S. Thanawala, V. C. Sundar, D. E. Morse, and P. Fratzl, "Skeleton of Euplectella sp.: structural hierarchy from the nanoscale to the macroscale.," *Science*, vol. 309, pp. 275–8, July 2005.

[75] O. Kolednik, J. Predan, F. D. Fischer, and P. Fratzl, "Bioinspired Design Criteria for Damage-Resistant Materials with Periodically Varying Microstructure," *Advanced Functional Materials*, vol. 21, pp. 3634–3641, Oct. 2011.

[76] L. Addadi and S. Weiner, "Biomineralization: a pavement of pearl," *Nature*, vol. 389, pp. 912–915, June 1997.

[77] A. Lin and M. A. Meyers, "Growth and structure in abalone shell," *Materials Science and Engineering: A*, vol. 390, pp. 27–41, Jan. 2005.

[78] H. Cölfen, "Biomineralization: A crystal-clear view.," *Nature materials*, vol. 9, pp. 960–1, Dec. 2010.

[79] F. Nudelman, K. Pieterse, A. George, P. H. H. Bomans, H. Friedrich, L. J. Brylka, P. A. J. Hilbers, G. de With, and N. A. J. M. Sommerdijk, "The role of collagen in bone apatite formation in the presence of hydroxyapatite nucleation inhibitors.," *Nature materials*, vol. 9, pp. 1004–9, Dec. 2010.

[80] A. Dey, P. H. H. Bomans, F. A. Müller, J. Will, P. M. Frederik, G. de With, and N. A. J. M. Sommerdijk, "The role of prenucleation clusters in surface-induced calcium phosphate crystallization.," *Nature materials*, vol. 9, pp. 1010–4, Dec. 2010.

[81] J. Aizenberg, A. Black, and G. Whitesides, "Control of crystal nucleation by patterned self-assembled monolayers," *Nature*, vol. 1720, no. 1971, pp. 1997–2000, 1999.

[82] B. Pokroy, V. F. Chernow, and J. Aizenberg, "Crystallization of malonic and succinic acids on SAMs: toward the general mechanism of oriented nucleation on organic monolayers.," *Langmuir*, vol. 25, pp. 14002–6, Dec. 2009.

[83] M. Lopez, P. Chen, J. McKittrick, and M. Meyers, "Growth of nacre in abalone: Seasonal and feeding effects," *Materials Science and Engineering: C*, vol. 31, pp. 238–245, Mar. 2011.

[84] S. Deville, "Freeze-Casting of Porous Ceramics: A Review of Current Achievements and Issues," *Advanced Engineering Materials*, vol. 10, pp. 155–169, Mar. 2008.

[85] M. C. Gutiérrez, M. L. Ferrer, and F. del Monte, "Ice-Templated Materials: Sophisticated Structures Exhibiting Enhanced Functionalities Obtained after Unidirectional Freezing and Ice-Segregation-Induced Self-Assembly," *Chemistry of Materials*, vol. 20, pp. 634–648, Feb. 2008.

[86] U. G. K. Wegst, M. Schecter, A. E. Donius, and P. M. Hunger, "Biomaterials by freeze casting.," *Philosophical transactions. Series A, Mathematical, physical, and engineering sciences*, vol. 368, pp. 2099–121, Apr. 2010.

[87] S. S. L. Peppin, J. a. W. Elliott, and M. G. Worster, "Solidification of colloidal suspensions," *Journal of Fluid Mechanics*, vol. 554, p. 147, Apr. 2006.

[88] T. Fukasawa, M. Ando, T. Ohji, and S. Kanzaki, "Synthesis of Porous Ceramics with Complex Pore Structure by Freeze-Dry Processing," *Journal of the American Ceramic Society*, vol. 84, pp. 230–232, Jan. 2001.

[89] S. Deville, E. Saiz, and A. P. Tomsia, "Ice-templated porous alumina structures," *Acta Materialia*, vol. 55, pp. 1965–1974, Apr. 2007.

[90] E. Munch, E. Saiz, A. P. Tomsia, and S. Deville, "Architectural Control of Freeze-Cast Ceramics Through Additives and Templating," *Journal of the American Ceramic Society*, vol. 92, pp. 1534–1539, July 2009.

[91] L. Hu, C.-A. Wang, Y. Huang, C. Sun, S. Lu, and Z. Hu, "Control of pore channel size during freeze casting of porous YSZ ceramics with unidirectionally aligned channels using different freezing temperatures," *Journal of the European Ceramic Society*, vol. 30, pp. 3389–3396, Dec. 2010.

[92] L. Hu, C.-A. Wang, and Y. Huang, "Porous YSZ ceramics with unidirectionally aligned pore channel structure: Lowering thermal conductivity by silica aerogels impregnation," *Journal of the European Ceramic Society*, vol. 31, pp. 2915–2922, Dec. 2011.

[93] Y. Tang, K. Zhao, J. Wei, and Y. Qin, "Fabrication of aligned lamellar porous alumina using directional solidification of aqueous slurries with an applied electrostatic field," *Journal of the European Ceramic Society*, vol. 30, pp. 1963–1965, July 2010.

[94] S. Deville, C. Viazzi, J. Leloup, A. Lasalle, C. Guizard, E. Maire, J. Adrien, and L. Gremillard, "Ice shaping properties, similar to that of antifreeze proteins, of a zirconium acetate complex.," *PloS one*, vol. 6, p. e26474, Jan. 2011.

[95] S. Deville, E. Saiz, and A. P. Tomsia, "Freeze casting of hydroxyapatite scaffolds for bone tissue engineering.," *Biomaterials*, vol. 27, pp. 5480–9, Nov. 2006.

[96] E. Munch, M. E. Launey, D. H. Alsem, E. Saiz, a. P. Tomsia, and R. O. Ritchie, "Tough, bio-inspired hybrid materials.," *Science*, vol. 322, pp. 1516–20, Dec. 2008.

[97] A. Ojuva, F. Akhtar, A. P. Tomsia, and L. Bergström, "Laminated adsorbents with very rapid CO2 uptake by freeze-casting of zeolites.," *ACS applied materials & interfaces*, vol. 5, pp. 2669–76, Apr. 2013.

[98] M. E. Launey, E. Munch, D. H. Alsem, E. Saiz, A. P. Tomsia, and R. O. Ritchie, "A novel biomimetic approach to the design of high-performance ceramic-metal composites.," *Journal of the Royal Society, Interface / the Royal Society*, vol. 7, pp. 741–53, May 2010.

[99] M. a. Meyers, J. McKittrick, and P.-Y. Chen, "Structural Biological Materials: Critical Mechanics-Materials Connections," *Science*, vol. 339, pp. 773–779, Feb. 2013.

[100] S. Deville, "Ice templating, freeze casting: Beyond materials processing," *Journal of Materials Research*, vol. 28, pp. 1–18, May 2013.

[101] H. J. Hwang, D. Y. Kim, and J. W. Moon, "Fabrication of Porous Clay Materials with Aligned Pore Structures by Freeze-Drying," *Materials Science Forum*, vol. 510-511, pp. 906–909, 2006.

[102] L. Qiu, J. Z. Liu, S. L. Chang, Y. Wu, and D. Li, "Biomimetic superelastic graphene-based cellular monoliths," *Nature Communications*, vol. 3, p. 1241, Dec. 2012.

[103] P. M. Hunger, A. E. Donius, and U. G. K. Wegst, "Platelets self-assemble into porous nacre during freeze casting.," *Journal of the mechanical behavior of biomedical materials*, vol. 19, pp. 87–93, Mar. 2013.

[104] J.-W. Kim, K. Tazumi, R. Okaji, and M. Ohshima, "Honeycomb Monolith-Structured Silica with Highly Ordered, Three-Dimensionally Interconnected Macroporous Walls," *Chemistry of Materials*, vol. 21, pp. 3476–3478, Aug. 2009.

[105] N. Ooi, A. Rairkar, L. Lindsley, and J. B. Adams, "Electronic structure and bonding in hexagonal boron nitride," *Journal of Physics Condensed Matter*, vol. 18, no. 1, pp. 97–115, 2006.

[106] A. Lipp, K. A. Schwetz, and K. Hunold, "Hexagonal boron nitride: Fabrication, properties and applications," *Journal of the European Ceramic Society*, vol. 5, no. 1, pp. 3–9, 1989.

[107] J. Eichler and C. Lesniak, "Boron nitride (BN) and BN composites for high-temperature applications," *Journal of the European Ceramic Society*, vol. 28, pp. 1105–1109, Jan. 2008.

[108] B. Ertug, T. Boyraz, and O. Addemir, "Microstructural aspects of the hot-pressed hexagonal boron nitride ceramics with limited content of boron oxide," *Materials Science Forum*, vol. 554, pp. 197–200, 2007.

[109] S.-K. Lee, K. Nakamura, S. Kume, and K. Watari, "Thermal conductivity of hot-pressed BN ceramics," *Materials Science Forum*, vol. 510-511, pp. 398–401, 2006.

[110] M. J. Crimp, D. A. Oppermann, and K. Krehbiel, "Suspension properties of hexagonal BN powders : effect of pH and oxygen content," *Journal of Materials Science*, vol. 4, pp. 2621–2625, 1999.

[111] B. J. Briscoe, A. U. Khan, and P. F. Luckham, "Optimising the dispersion on an alumina suspension using commercial polyvalent electrolyte dispersants," *Journal of the European Ceramic Society*, vol. 18, pp. 2141–2147, Dec. 1998.

[112] J. Cesarano, I. A. Aksay, and A. Bleier, "Stability of Aqueous alpha-Al2O3 Suspensions with Poly(methacrylic acid) Polyelectrolyte," *Journal of the American Ceramic Society*, vol. 71, pp. 250–255, Apr. 1988.

[113] G. H. Kirby, D. J. Harris, Q. Li, and J. A. Lewis, "Poly(acrylic acid)-Poly(ethylene oxide) Comb Polymer Effects on BaTiO 3 Nanoparticle Suspension Stability," *Journal of the American Ceramic Society*, vol. 87, pp. 181–186, Feb. 2004.

[114] J. a. Lewis, "Colloidal processing of ceramics," *Journal of the American Ceramic Society*, vol. 83, no. 10, pp. 2341–2359, 2000.

[115] J. Wang and P. Somasundaran, "Mechanisms of ethyl(hydroxyethyl) cellulose-solid interaction: influence of hydrophobic modification.," *Journal of colloid and interface science*, vol. 293, pp. 322–32, Jan. 2006.

[116] H. Barnes, J. Hutton, and K. Walters, *An introduction to rheology*. 1989.

[117] L. Bergstrom, "Shear thinning and shear thickening of concentrated ceramic suspensions," *Colloids and Surfaces A: Physicochemical and Engineering Aspects*, vol. 133, p. 1998, 1998.

[118] M. Mora, F. Gimeno, H. Amaveda, L. Angurel, and R. Moreno, "Dispersant-free colloidal fabrication of Bi2Sr2CaCu2O8 superconducting thick films," *Journal of the European Ceramic Society*, vol. 30, pp. 917–926, Mar. 2010.

[119] E. Loth, "Drag of non-spherical solid particles of regular and irregular shape," *Powder Technology*, vol. 182, pp. 342–353, Mar. 2008.

[120] K.-S. Khoo, E.-J. Teh, Y.-K. Leong, and B. C. Ong, "Hydrogen Bonding and Interparticle Forces in Platelet alpha-Al(2)O(3) Dispersions: Yield Stress and Zeta Potential.," *Langmuir : the ACS journal of surfaces and colloids*, pp. 3418–3424, Feb. 2009.

[121] S. Gautier, E. Champion, D. Bernache-Assollant, and T. Chartier, "Rheological characteristics of alumina platelet-Hydroxyapatite composite suspensions," *Journal of the European Ceramic Society*, vol. 19, pp. 469–477, Apr. 1999.

[122] Y. K. Leong, P. J. Scales, T. W. Healy, D. V. Boger, and R. Buscall, "Rheological evidence of adsorbate-mediated short-range steric forces in concentrated dispersions," *Journal of the Chemical Society, Faraday Transactions*, vol. 89, no. 14, p. 2473, 1993.

[123] S. Biggs, P. J. Scales, Y.-K. Leong, and T. W. Healy, "Effects of citrate adsorption on the interactions between zirconia surfaces," *Journal of the Chemical Society, Faraday Transactions*, vol. 91, no. 17, p. 2921, 1995.

[124] P. Moulin and H. Roques, "Zeta potential measurement of calcium carbonate," *Journal of Colloid and Interface Science*, vol. 261, pp. 115–126, May 2003.

[125] A. Lasalle, C. Guizard, E. Maire, J. Adrien, and S. Deville, "Particle redistribution and structural defect development during ice templating," *Acta Materialia*, Mar. 2012.

[126] T. Divoux, D. Tamarii, C. Barentin, S. Teitel, and S. Manneville, "Yielding dynamics of a Herschel-Bulkley fluid: a critical-like fluidization behaviour," *Soft Matter*, vol. 8, no. 15, p. 4151, 2012.

[127] G. P. Roberts and H. A. Barnes, "New measurements of the fow-curves for Carbopol dispersions without slip artefacts," *Rheologica Acta*, vol. 40, pp. 499–503, 2001.

[128] C. B. Murray, C. R. Kagan, and M. G. Bawendi, "Synthesis and characterization of monodisperse nanocrystals and close-packed nanocrystals assemblies," *Annual Review of Materials Science*, vol. 30, pp. 545–610, Aug. 2000.

[129] A. R. Tao, D. P. Ceperley, P. Sinsermsuksakul, A. R. Neureuther, and P. Yang, "Self-organized silver nanoparticles for three-dimensional plasmonic crystals.," *Nano letters*, vol. 8, pp. 4033–8, Nov. 2008.

[130] B. D. Hatton, L. Mishchenko, S. Davis, K. H. Sandhage, and J. Aizenberg, "Assembly of large-area, highly ordered, crack-free inverse opal films.," *Proceedings of the National Academy of Sciences*, vol. 107, pp. 10354–9, June 2010.

[131] P. Podsiadlo, A. K. Kaushik, E. M. Arruda, A. M. Waas, B. S. Shim, J. Xu, H. Nandivada, B. G. Pumplin, J. Lahann, A. Ramamoorthy, and N. A. Kotov, "Ultrastrong and stiff layered polymer nanocomposites.," *Science*, vol. 318, pp. 80–3, Oct. 2007.

[132] A. Walther, I. Bjurhager, J.-M. Malho, J. Pere, J. Ruokolainen, L. a. Berglund, and O. Ikkala, "Large-area, lightweight and thick biomimetic composites with superior material properties via fast, economic, and green pathways.," *Nano letters*, vol. 10, pp. 2742–8, Aug. 2010.

[133] J. Lee and Y. Deng, "The morphology and mechanical properties of layer structured cellulose microfibril foams from ice-templating method," *Biomacromolecules*, vol. 7, no. 13, p. 6034, 2011.

[134] H. E. Romeo, C. E. Hoppe, M. A. López-Quintela, R. J. J. Williams, Y. Minaberry, and M. Jobbagy, "Directional freezing of liquid crystalline systems: from silver nanowire/PVA aqueous dispersions to highly ordered and electrically conductive macroporous scaffolds," *Journal of Materials Chemistry*, vol. 22, no. 18, p. 9195, 2012.

[135] P. M. Hunger, A. E. Donius, and U. G. K. Wegst, "Structure-property-processing correlations in freeze-cast composite scaffolds.," *Acta biomaterialia*, vol. 9, pp. 6338–48, May 2013.

[136] P. Cloetens, W. Ludwig, J. Baruchel, D. Van Dyck, J. Van Landuyt, J. P. Guigay, and M. Schlenker, "Holotomography: Quantitative phase tomography with micrometer resolution using hard synchrotron radiation x rays," *Applied Physics Letters*, vol. 75, no. 19, p. 2912, 1999.

[137] J. Schindelin, I. Arganda-Carreras, E. Frise, V. Kaynig, M. Longair, T. Pietzsch, S. Preibisch, C. Rueden, S. Saalfeld, B. Schmid, J.-Y. Tinevez, D. J. White, V. Hartenstein, K. Eliceiri, P. Tomancak, and A. Cardona, "Fiji: an open-source platform for biological-image analysis.," *Nature methods*, vol. 9, pp. 676–82, July 2012.

[138] D. Maillet, S. André, J.-C. Batsale, A. Degiovanni, and C. Moyne, *Thermal Quadrupoles: Solving the heat Equation through Integral Transforms*. Chichester: Wiley, 2000.

[139] C. Lu and Y.-W. Mai, "Influence of Aspect Ratio on Barrier Properties of Polymer-Clay Nanocomposites," *Physical Review Letters*, vol. 95, p. 088303, Aug. 2005.

[140] H. Stanley, "Scaling, universality, and renormalization: Three pillars of modern critical phenomena," *Reviews of Modern Physics*, vol. 71, pp. S358–S366, Mar. 1999.

[141] A. V. Parsegian, *Van der Walls forces*. Cambridge Univ Press, 2006.

[142] R. Asthana and S. N. Tewari, "The engulfment of foreign particles by a freezing interface," *Journal of Materials Science*, vol. 28, no. 20, pp. 5414–5425, 1993.

[143] J. Garvin, Y. Yang, and H. Udaykumar, "Multiscale modeling of particle-solidification front dynamics. Part II: Pushing-engulfment transition," *International Journal of Heat and Mass Transfer*, vol. 50, pp. 2969–2980, July 2007.

[144] G. Lipp, "On the engulfment of spherical particles by a moving ice-liquid interface," *Journal of Crystal Growth*, vol. 130, pp. 475–489, June 1993.

[145] S. a. Barr and E. Luijten, "Structural properties of materials created through freeze casting," *Acta Materialia*, vol. 58, pp. 709–715, Jan. 2010.

[146] M. Di Michiel, J. M. Merino, D. Fernandez-Carreiras, T. Buslaps, V. Honkimaki, P. Falus, T. Martins, and O. Svensson, "Fast microtomography using high energy synchrotron radiation," *Review of Scientific Instruments*, vol. 76, no. 4, p. 043702, 2005.

[147] S. Deville, J. Adrien, E. Maire, M. Scheel, and M. Di Michiel, "Time-lapse, three-dimensional in situ imaging of ice crystal growth in a colloidal silica suspension," *Acta Materialia*, vol. 61, pp. 2077–2086, Apr. 2013.

[148] M. E. Levinshtein, S. L. Rumyantsev, and M. S. Shur, *Properties of Advanced Semiconductor Materials: GaN, A1N, InN, BN, SiC, SiGe*. Wiley-Interscience, 2001.

[149] K. Binder, *The Monte Carlo Method in Condensed Matter Physics*. Springer, New York, 1992.

[150] A. W. Rempel and M. G. Worster, "The interaction between a particle and an advancing solidification front," *Journal of Crystal Growth*, vol. 205, no. 3, pp. 427–440, 1999.

[151] P. Casses and M. Azouni-Aidi, "A general theoritical approach to the behaviour of a foreign particles at advancing solid-liquid interfaces," *Advances in colloid and interface science*, vol. 50, pp. 103–120, 1994.

[152] M. S. Park, A. A. Golovin, and S. H. Davis, "The encapsulation of particles and bubbles by an advancing solidification front," *Journal of Fluid Mechanics*, vol. 560, p. 415, July 2006.

[153] J. C. T. Kao and A. a. Golovin, "Particle capture in binary solidification," *Journal of Fluid Mechanics*, vol. 625, p. 299, Apr. 2009.

[154] R. Berardi, C. Fava, and C. Zannoni, "A Gay-Berne potential for dissimilar biaxial particles," *Chemical Physics Letters*, vol. 297, pp. 8–14, Nov. 1998.

[155] R. Berardi, C. Fava, and C. Zannoni, "A generalized Gay-Berne intermolecular potential for biaxial particles," *Chemical Physics Letters*, vol. 236, pp. 462–468, Apr. 1995.

[156] M. Babadi, M. Ejtehadi, and R. Everaers, "Analytical first derivatives of the RE-squared interaction potential," *Journal of Computational Physics*, vol. 219, pp. 770–779, Dec. 2006.

[157] F. Y. Fraige, P. a. Langston, and G. Z. Chen, "Distinct element modelling of cubic particle packing and flow," *Powder Technology*, vol. 186, pp. 224–240, Sept. 2008.

[158] S. Li, J. Zhao, P. Lu, and Y. Xie, "Maximum packing densities of basic 3D objects," *Chinese Science Bulletin*, vol. 55, pp. 114–119, Jan. 2010.

[159] S. N. Nasser and M. Hori, *Micromechanics: Overall Properties of Heterogeneous Materials*. Applied Mathematics and Mechanics Series, North-Holland Publ., 1993.

[160] D.-W. Ni, G.-J. Zhang, Y.-M. Kan, and Y. Sakka, "Textured h-BN Ceramics Prepared by Slip Casting," *Journal of the American Ceramic Society*, vol. 94, pp. 1397–1404, May 2011.

[161] X. Duan, D. Jia, Z. Wu, Z. Tian, Z. Yang, S. Wang, and Y. Zhou, "Effect of sintering pressure on the texture of hot-press sintered hexagonal boron nitride composite ceramics," *Scripta Materialia*, vol. 68, pp. 104–107, Jan. 2013.

[162] K. H. Brosnan, G. L. Messing, R. J. Meyer, and M. D. Vaudin, "Texture Measurements in <001> Fiber-Oriented PMN-PT," *Journal of the American Ceramic Society*, vol. 89, pp. 1965–1971, June 2006.

[163] L. Gibson and M. Ashby, *Cellular Solids: Structure and Properties*. Cambridge Univ Press, 1999.

[164] A. Da Silva and S. Kyriakides, "Compressive response and failure of balsa wood," *International Journal of Solids and Structures*, vol. 44, pp. 8685–8717, Dec. 2007.

[165] M. Scheffler and P. Colombo, *Cellular Ceramics: Structure, Manufacturing, Properties and Applications*. Wiley-VCH (Weinheim), 2005.

[166] T. Isobe, Y. Kameshima, A. Nakajima, K. Okada, and Y. Hotta, "Gas permeability and mechanical properties of porous alumina ceramics with unidirectionally aligned pores," *Journal of the European Ceramic Society*, vol. 27, pp. 53–59, Jan. 2007.

[167] P. Greil, T. Lifka, and A. Kaindl, "Biomorphic Cellular Silicon Carbide Ceramics from Wood: II. Mechanical Properties," *Journal of the European Ceramic Society*, vol. 18, pp. 1975–1983, Dec. 1998.

[168] E. Vogli, H. Sieber, and P. Greil, "Biomorphic SiC-ceramic prepared by Si-vapor phase infiltration of wood," *Journal of the European Ceramic Society*, vol. 22, pp. 2663–2668, 2002.

[169] C. R. Rambo, T. Andrade, T. Fey, H. Sieber, A. E. Martinelli, and P. Greil, "Microcellular Al 2 O 3 Ceramics from Wood for Filter Applications," *Journal of the American Ceramic Society*, vol. 91, pp. 852–859, Mar. 2008.

[170] A. R. Studart, U. T. Gonzenbach, E. Tervoort, and L. J. Gauckler, "Processing Routes to Macroporous Ceramics: A Review," *Journal of the American Ceramic Society*, vol. 89, pp. 1771–1789, June 2006.

[171] C. Hong, X. Zhang, J. Han, J. Du, and W. Han, "Ultra-high-porosity zirconia ceramics fabricated by novel room-temperature freeze-casting," *Scripta Materialia*, vol. 60, pp. 563–566, Apr. 2009.

[172] Y.-W. Moon, K.-H. Shin, Y.-H. Koh, W.-Y. Choi, and H.-E. Kim, "Porous alumina ceramics with highly aligned pores by heat-treating extruded alumina/camphene body at temperature near its solidification point," *Journal of the European Ceramic Society*, vol. 32, pp. 1029–1034, May 2012.

[173] M. Fukushima, M. Nakata, and Y.-i. Yoshizawa, "Fabrication and properties of ultra highly porous cordierite with oriented micrometer-sized cylindrical pores by gelation and freezing method," *Journal of the Ceramic Society of Japan*, vol. 116, pp. 1322–1325, 2008.

[174] M. Fukushima, M. Nakata, Y. Zhou, T. Ohji, and Y.-i. Yoshizawa, "Fabrication and properties of ultra highly porous silicon carbide by the gelation–freezing method," *Journal of the European Ceramic Society*, vol. 30, pp. 2889–2896, Oct. 2010.

[175] S. Deville and G. Bernard-Granger, "Influence of surface tension, osmotic pressure and pores morphology on the densification of ice-templated ceramics," *Journal of the European Ceramic Society*, Jan. 2011.

[176] S. Deville, J. Adrien, E. Maire, M. Scheel, and M. D. Michiel, "Time-lapse, three-dimensional in situ imaging of ice crystal growth in a colloidal silica suspension," *submitted*, 2012.

[177] J. Sekhar and R. Trivedi, "Solidification microstructure evolution in the presence of inert particles," *Materials Science and Engineering A*, vol. 147, pp. 9–21, 1991.

[178] M. Vural and G. Ravichandran, "Microstructural aspects and modeling of failure in naturally occurring porous composites," *Mechanics of Materials*, vol. 35, no. 3-6, pp. 523–536, 2003.

[179] N. O. Shanti, K. Araki, and J. W. Halloran, "Particle Redistribution During Dendritic Solidification of Particle Suspensions," *Journal of the American Ceramic Society*, vol. 89, pp. 2444–2447, Aug. 2006.

[180] R. J. Pavlacka and G. L. Messing, "Processing and mechanical response of highly textured Al2O3," *Journal of the European Ceramic Society*, vol. 30, pp. 2917–2925, Oct. 2010.

[181] S. S. Peppin, J. A. W. Elliott, and M. G. Worster, "Solidification of colloidal suspensions," *Journal of Fluid Mechanics*, vol. 554, p. 147, Apr. 2006.

[182] U. T. Gonzenbach, A. R. Studart, E. Tervoort, and L. J. Gauckler, "Macroporous Ceramics from Particle-Stabilized Wet Foams," *Journal of the American Ceramic Society*, vol. 90, pp. 16–22, Jan. 2007.

[183] H.-J. Yoon, U.-C. Kim, J.-H. Kim, Y.-H. Koh, W.-Y. Choi, and H.-E. Kim, "Macroporous Alumina Ceramics with Aligned Microporous Walls by Unidirectionally Freezing Foamed Aqueous Ceramic Suspensions," *Journal of the American Ceramic Society*, vol. 1582, pp. 2009–2011, Feb. 2010.

[184] J. Han, C. Hong, X. Zhang, J. Du, and W. Zhang, "Highly porous ZrO2 ceramics fabricated by a camphene-based freeze-casting route: Microstructure and properties," *Journal of the European Ceramic Society*, vol. 30, pp. 53–60, Jan. 2010.

[185] G. L. Messing, S. Trolier-McKinstry, E. M. Sabolsky, C. Duran, S. Kwon, B. Brahmaroutu, P. Park, H. Yilmaz, P. W. Rehrig, K. B. Eitel, E. Suvaci, M. Seabaugh, and K. S. Oh, *Templated Grain Growth of Textured Piezoelectric Ceramics*, vol. 29. Apr. 2004.

[186] S.-H. Lee, S.-H. Jun, H.-E. Kim, and Y.-H. Koh, "Piezoelectric Properties of PZT-Based Ceramic with Highly Aligned Pores," *Journal of the American Ceramic Society*, vol. 91, pp. 1912–1915, June 2008.

[187] S. F. Poterala, Y. Chang, T. Clark, R. J. Meyer, and G. L. Messing, "Mechanistic Interpretation of the Aurivillius to Perovskite Topochemical Microcrystal Conversion Process," *Chemistry of Materials*, vol. 22, pp. 2061–2068, Mar. 2010.

[188] Y. Saito, H. Takao, T. Tani, T. Nonoyama, K. Takatori, T. Homma, T. Nagaya, and M. Nakamura, "Lead-free piezoceramics.," *Nature*, vol. 432, pp. 84–7, Nov. 2004.

[189] Y. Chang, S. F. Poterala, Z. Yang, S. Trolier-McKinstry, and G. L. Messing, "Microstructure development and piezoelectric properties of highly textured CuO-doped KNN by templated grain growth," *Journal of Materials Research*, vol. 25, pp. 687–694, Jan. 2011.

[190] M. Launey, E. Munch, D. Alsem, H. Barth, E. Saiz, a.P. Tomsia, and R. Ritchie, "Designing highly toughened hybrid composites through nature-inspired hierarchical complexity," *Acta Materialia*, vol. 57, pp. 2919–2932, June 2009.

[191] M. Ashby, *Materials Selection in Mechanical Design*. 2010.

[192] K. Okumura and P. G. De Gennes, "Why is nacre strong ? Elastic theory and fracture mechanics for biocomposites with stratified structures," *The European Physical Journal E*, vol. 4, no. 1, pp. 121–127, 2001.

[193] F. Song and Y. L. Bai, "Effects of nanostructures on the fracture strength of the interfaces in nacre," *Journal of Materials Research*, vol. 18, no. 8, pp. 1741–1744, 2003.

[194] E. Munch, M. E. Launey, D. H. Alsem, E. Saiz, A. P. Tomsia, and R. O. Ritchie, "Tough, bio-inspired hybrid materials.," *Science (New York, N.Y.)*, vol. 322, pp. 1516–20, Dec. 2008.

[195] S. Deville, E. Maire, G. Bernard-Granger, A. Lasalle, A. Bogner, C. Gauthier, J. Leloup, and C. Guizard, "Metastable and unstable cellular solidification of colloidal suspensions.," *Nature materials*, vol. 8, pp. 966–72, Dec. 2009.

[196] E. Munch, E. Saiz, A. P. Tomsia, and S. Deville, "Architectural Control of Freeze-Cast Ceramics Through Additives and Templating," *Journal of the American Ceramic Society*, vol. 92, pp. 1534–1539, July 2009.

[197] S. I. Bae and S. Baik, "Determination of Critical Concentrations of Silica and/or Calcia for Abnormal Grain Growth in Alumina," *Journal of the American Ceramic Society*, vol. 76, no. 4, pp. 1065–67, 1993.

[198] R. K. Nalla, J. S. Stölken, J. H. Kinney, and R. O. Ritchie, "Fracture in human cortical bone: local fracture criteria and toughening mechanisms.," *Journal of biomechanics*, vol. 38, pp. 1517–25, July 2005.

[199] C. Herring, "Effect of Change of Scale on Sintering Phenomena," *Journal of Applied Physics*, vol. 21, no. 4, p. 301, 1950.

[200] A. Zaitsev, A. Litvina, B. Mogutnov, and A. Tsaplin, "Thermodynamic properties and phase equilibria in the system CaO-SiO2-Al2O3," *High Temperature and Material Science*, vol. 34, pp. 223–231, 1995.

[201] W. J. Clegg, K. Kendall, N. M. Alford, T. W. Button, and J. D. Birchall, "A simple way to make tough ceramics," *Nature*, vol. 347, pp. 455–457, Oct. 1990.

[202] K. Faber and A. Evans, "Crack deflection processes-I. Theory," *Acta Metallurgica*, vol. 31, no. 4, pp. 564–576, 1983.

[203] K. J. Koester, J. W. Ager, and R. O. Ritchie, "The effect of aging on crack-growth resistance and toughening mechanisms in human dentin.," *Biomaterials*, vol. 29, pp. 1318–28, Apr. 2008.

[204] R. C. Garvie, R. H. Hannink, and R. T. Pascoe, "Ceramic steel?," *Nature*, vol. 258, pp. 703–704, Dec. 1975.

[205] *ASTM E1820-06. Annual book of ASTM standards, vol. 03.01: Metals—Mechanical testing; Elevated and low-temperature tests; Metallography*. pa: astm i ed., 2006.

[206] J. Cook, J. E. Gordon, C. C. Evans, and D. M. Marsh, "A Mechanism for the Control of Crack Propagation in All-Brittle Systems," *Proceedings of the Royal Society A: Mathematical, Physical and Engineering Sciences*, vol. 282, pp. 508–520, Dec. 1964.

[207] L. S. Dimas and M. J. Buehler, "Tough and stiff composites with simple building blocks," *Journal of Materials Research*, pp. 1–9, May 2013.

[208] W. H. Tuan, H. H. Wu, and T. J. Yang, "The preparation of AI2O3/Ni composites by a powder coating technique," *Journal of Materials Science*, vol. 30, pp. 855–859, Feb. 1995.

[209] N. Travitzky, E. Gutmanas, and N. Claussen, "Mechanical properties of composites fabricated by pressureless infiltration technique," *Materials Letters*, vol. 33, pp. 47–50, Nov. 1997.

[210] H. Prielipp, M. Knechtel, N. Claussen, S. Streiffer, H. Müllejans, M. Rühle, and J. Rödel, "Strength and fracture toughness of aluminum/alumina composites with interpenetrating networks," *Materials Science and Engineering: A*, vol. 197, pp. 19–30, June 1995.

[211] M. K. Aghajanian, N. H. MacMillan, C. R. Kennedy, S. J. Luszcz, and R. Roy, "Properties and microstructures of Lanxide Al2O3-Al ceramic composite materials," *Journal of Materials Science*, vol. 24, pp. 658–670, Feb. 1989.

[212] G. Chen, T. Ushida, and T. Tateishi, "Hybrid Biomaterials for Tissue Engineering: A Preparative Method for PLA or PLGA-Collagen Hybrid Sponges," *Advanced Materials*, vol. 12, pp. 455–457, Mar. 2000.

[213] J. Liu, H. Yan, and K. Jiang, "Mechanical properties of graphene platelet-reinforced alumina ceramic composites," *Ceramics International*, vol. 39, pp. 6215–6221, Aug. 2013.

[214] T. Wei, Z. Fan, G. Luo, F. Wei, D. Zhao, and J. Fan, "The effect of carbon nanotubes microstructures on reinforcing properties of SWNTs/alumina composite," *Materials Research Bulletin*, vol. 43, pp. 2806–2809, Oct. 2008.

[215] a. Peigney, C. Laurent, E. Flahaut, and a. Rousset, "Carbon nanotubes in novel ceramic matrix nanocomposites," *Ceramics International*, vol. 26, pp. 677–683, July 2000.

[216] G. Yamamoto, M. Omori, T. Hashida, and H. Kimura, "A novel structure for carbon nanotube reinforced alumina composites with improved mechanical properties.," *Nanotechnology*, vol. 19, p. 315708, Aug. 2008.

[217] P. F. Becher, "Microstructural Design of Toughened Ceramics," *Journal of the American Ceramic Society*, vol. 74, pp. 255–269, Oct. 1991.

[218] U. G. K. Wegst and M. F. Ashby, "The mechanical efficiency of natural materials," *Philosophical Magazine*, vol. 84, pp. 2167–2186, July 2004.

[219] R. G. Munro, "Evaluated Material Properties for a Sintered alpha-Alumina," *Journal of the American Ceramic Society*, vol. 28, pp. 1919–1928, 1997.

[220] G.-D. Zhan, J. D. Kuntz, J. Wan, and A. K. Mukherjee, "Single-wall carbon nanotubes as attractive toughening agents in alumina-based nanocomposites.," *Nature materials*, vol. 2, pp. 38–42, Jan. 2003.

List of Figures